100% automatic metrology with UAV photogrammetry and embedded GPS and its application in dike monitoring

Yilin Zhou

Université Paris-Est

École Doctorale MSTIC
Mathématiques & Sciences et Technologies
de l'Information et de la Communication

Spécialité: Sciences et Technologies de l'Information Géographique

THÈSE DE DOCTORAT

En vue de l'obtention du grade de :

Docteur de l'Université Paris-Est

présentée et soutenue le 6 Décembre 2019 par :

Yilin Zhou

Métrologie 100% automatique par photogrammétrie aéroportée légère et GPS de précision permanent et embarqué, application au suivi de digues

Composition du jury :

Directeur de thèse: Marc Pierrot-Deseilligny	IGN-ENSG
Rapporteur: Pierre Grussenmeyer	INSA Strasbourg
Rapporteur: Peter Sturm	INRIA Grenoble Rhône-Alpes
Examinateur: Francesco Nex	University of Twente
Examinatrice: Marie-Odile Berger	INRIA Nancy Grand Est
Président du jury: Pascal Monasse	ENPC
Encadrante: Ewelina Rupnik	IGN-ENSG
Membre invité: Paul-Henri Faure	CNR

Paris-Est University

MSTIC Doctoral School

Mathematics & Sciences and Technologies
of Information and Communication

Domain: Sciences and Technologies of Geographical Information

Ph.D Thesis

To obtain the grade of :

Doctorate of Paris-Est University

presented and defended on 6th December 2019 by :

Yilin Zhou

100% automatic metrology with UAV photogrammetry and embedded GPS, and its application in dike monitoring

Composition of the jury :

Supervisor: Marc Pierrot-Deseilligny	IGN-ENSG
Reviewer: Pierre Grussenmeyer	INSA Strasbourg
Reviewer: Peter Sturm	INRIA Grenoble Rhône-Alpes
Examiner: Francesco Nex	University of Twente
Examiner: Marie-Odile Berger	INRIA Nancy Grand Est
President of jury: Pascal Monasse	ENPC
Co-supervisor: Ewelina Rupnik	IGN-ENSG
Invited Member: Paul-Henri Faure	CNR

RÉSUMÉ

Le développement des plateformes de véhicules aériens autonomes (UAV) en fait une source de données précieuse pour les applications d'inspection, de suivi, de cartographie et de modélisation 3D. Le drone ouvre de nouvelles applications dans la photogrammétrie aérienne rapprochée et introduit une alternative peu coûteuse à la photogrammétrie classique pour véhicules pilotés.

La cartographie de corridors, est l'un des domaines d'importance considérable pour la photogrammétrie par drone, car largement sollicitée pour le suivi et la gestion de certaines infrastructures — les autoroutes, les voies ferroviaires, les voies navigables et les oléoducs. En raison de la géométrie particulière de la scène, ceci est un cas à prendre avec précaution. Les erreurs s'accumulent facilement sur la plus longue dimension de la scène et une déformation en bol est souvent observée; de plus, la planéité de la scène introduit de fortes corrélations entre les paramètres à déterminer. Ces deux facteurs réunis rendent plus difficile l'obtention de résultats de haute précision dans la configuration corridor par rapport à une géométrie de prise de vue plus classique.

Cette thèse est un projet de recherche initié par la CNR, un concessionnaire fluvial, responsable de la maintenance et de la surveillance de ses ouvrages hydrauliques, et plus particulièrement des digues. L'objectif est d'appliquer la photogrammétrie par drone pour obtenir un suivi 3D dense, plus rapide et moins chère, pour l'ausculation de ces digues. Dans le cadre de la thèse, nous cherchons à réduire le travail de terrain tout en maintenant une précision cartographique élevée, en l'occurence, diminuer le nombre de points de contrôle au sol (GCP).

Dans un premier temps, des simulations sont réalisées pour mieux comprendre certains problèmes de cartographie de corridors qui impactent la précision finale. Ensuite, des études plus approfondies sont menées sur les trois aspects qui nous intéressent le plus. Le premier porte sur la géométrie de l'acquisition aérienne, et plus précisément sur l'influence des images obliques, des images nadir de différentes hauteurs de vol, ainsi que la possibilité d'une calibration de caméra en vol et son application à une géométrie d'acquisition défavorable. Le deuxième vise à améliorer les performances d'acquisition des caméras métriques haute gamme. La déformation de l'image introduite par la variation de la température de la caméra est étudiée et modélisée. Une méthode de correction de cet effet thermique est proposée, ses performances sont évaluées sur des jeux de données terrestres et aériens en configuration de corridors. Le dernier s'intéresse à l'effet de l'obturateur roulant utilisé dans les caméras grand public, qui est vu couramment sur les plateformes UAV du marché. Deux méthodes sont présentées pour calibrer le temps de lecture de la caméra, une propriété qui n'est souvent pas donnée par les fabricants de caméras. Une méthode en deux étapes est proposée pour la correction de l'effet de l'obturateur roulant, ses performances sont évaluées dans les configurations de bloc et de corridor.

Mots clefs : UAV, suivi de digue, cartographie de corridors, géométrie d'acquisition, effet thermique, obturateur roulant

ABSTRACT

The development of unmanned aerial vehicle (UAV) platform makes it nowadays a valuable source of data for inspection, surveillance, mapping and 3D modeling issues. UAV photogrammetry opens various new applications in close-range aerial domain and introduces a low-cost alternative to classical manned vehicle photogrammetry.

Corridor mapping, one of the fields with substantial importance for UAV photogrammetry, is largely demanded in the surveillance and management of infrastructure assets – highways, railways, waterways and pipelines. Due to the special geometry of the scene, corridor mapping is one case that needs taking precautions. Errors accumulate easily on the longer dimension of the scene and a bowl effect is often observed; the flatness of the scene introduces strong correlations between parameters to be determined, these two factors together, make it more difficult to obtain high accuracy results in corridor configuration than in classical ones.

This thesis is a research project initiated by the CNR, a river concessionary, which has the responsibility of the maintenance and surveillance of its hydraulic facilities, more particularly the dikes. The objective is to apply UAV photogrammetry, which is faster, cheaper and offers a 3D dense reconstruction of the scene, to the monitoring of dikes. While maintaining a high surveying accuracy, a reduced field work, i.e. the number of ground control points (GCPs) is expected.

In the first place, simulations are carried out to gain an insight of several problems of corridor mapping that impact the final accuracy. Then, thorough investigations are conducted on three aspects that interest us the most. The first study focuses on the aerial acquisition geometry, discussions are given on the influence of oblique images, nadir images of different flight heights as well as the possibility of an in-flight camera calibration and its application on unfavourable acquisition geometry. The second study aims to improve the acquisition performance for high-end metric cameras. The image deformation introduced by camera temperature variation is investigated and modelled. A method for the correction of this thermal effect is proposed, its performance is evaluated on both terrestrial and aerial datasets of corridor configuration. The last study interests in the rolling shutter effect for consumer-grade cameras, which is commonly seen in UAV platforms on the market. Two methods are presented to calibrate the camera readout time, a property that is often not given by camera manufacturers. A two-step method is proposed for the correction of rolling shutter effect, its performance is evaluated in both block and corridor configurations.

Keywords : UAV, dike monitoring, corridor mapping, acquisition geometry, thermal effect, rolling shutter

Acknowledgements

Three years of PhD life have passed in the blink of an eye and here I find myself at the end of the journey. I will always cherish the three years I spent here. Not only because it has been a wonderful experience I shared with great people, but also because it taught me that the world is interesting and fascinating when you stay open-minded and curious.

I consider myself fortunate to have had the opportunity to do research and pursue a PhD. I will never take for granted the support, inspiration, and guidance I've received, in a country that is 10000 km away from my home in China, by a bunch of people that come from different cultures and speak different languages than me. Thanks to them, I have never been homesick, except when my stomach fancies Chinese food.

My gratitude first goes to my thesis supervisor, Marc Pierrot-Deseilligny, without whom my thesis would never have been accomplished. Under his supervision, I have learned not only how to work, but also how to be humble and indulgent. I would like to thank him for having given me time to make mistakes, to learn and to progress.

I would also like to thank my industrial supervisor, Paul-Henri Faure, for the financial and operational supports he provided me, on behalf of the Compagnie Nationale du Rhône (CNR).

To the MicMac team with whom I spent three years, I am incredibly happy and thankful. My sincere thanks goes to Ewelina Rupnik, for being a wonderful supervisor, a friend from whom I learned a lot, not to mention all the fines she had for being the prime driver on the way to data acquisitions. To Mehdi Daakir, for being an impeccable friend in both my work and personal lives. He spent countless weekends with me, helping with data processing and writing; he also picked me up when I locked myself out of my apartment. To Giang Nguyen, for all the joy he brought to me with his unintentional humor and his endless creativity. The only way I can possibly thank each of them is through a long-lasting friendship.

My gratitude also extends to all my colleagues from LOEMI, with whom I have always felt like a spoiled child. To Christian Thom, for sharing his wisdon whenever I came to him with problems, and for sharing his insight and understanding of quantum physics. To Christophe Meynard, for unreservedly providing me with help, for sharing with me his passion for the sci-fi novel *The Three-Body Problem* and for suffering through a 20-hour drive with me in a car without air conditioning. To Olivier Martin, for all the technical and instrumental support, for being a great friend with whom I play badmintion, go to market, share tea time, and joke around with. I am sure he will be the best father for his daughter Rose. To Jean-Philippe Souchon, for showing me his great passion about music which encouraged me to pursue my own passion, and for sharing with me the life of his guinea pig. To Jean Michael Müller, for his wisdom, for always providing me help, and for buying me the fabulous movie poster from *Good Morning England*.

I would like to express my appreciation to all the fellows of the research team: Jonathan Lisein, Imane Fikri, Lulin Zhang, Mohamed Amjad Lasri, Ahmad Audi, Evelyn Paiz, Raphael Sulzer, Qasem Safari, Stephane Guinard, Oussama Ennafii, Na-

than Piasco, Teng Wu, Emile Blettery, Olivier Stocker, Benjamin Lauer, and Laurent Caraffa. I am grateful for their knowledge, as well as the experiences and unforgettable moments we shared together. I would like to acknowledge my colleagues from ENSG: Antoine Pinte, Marc Poupée, Jean-François Hangouët, Patricia Pellardi, Jean-Pierre Papelard, Serge Botton, Jacques Beilin, for the help they provided during my thesis. I would like to thank my colleagues from team TS at IGN: Laurent Heydel, Paul Bouquet, Fabien Bergerault and Sylvain Gonnet, for their participation in data acquisition and processing. I would like to acknowledge the staff of Université Paris-Est: Sylvie Cach and Fatima de Freitas, for their help on administration procedures.

A special gratitude goes to Clément Bouché, for always being understanding and supportive. Your one-of-a-kind humor and jokes added an irreplaceable flavour to my PhD student life.

Last but not the least, I would like to thank my parents for always being there for me and for always letting me pursue my dreams. Confucius said, “whilst thy father and mother are living, do not wander afar. If thou must travel, hold a set course.” I hope to live up to their expectations and to never worry them.

Compagnie Nationale du Rhône (CNR)

Direction du Port de Lyon

1, rue de Chalon-sur-Saône

69007 Lyon

France

Institut National de l'Information Géographique et Forestière (IGN)

73 avenue de Paris

94165 SAINT-MANDÉ

France

Ecole Nationale des Sciences Géographiques (ENSG)

6-8 Avenue Blaise Pascal

Cité Descartes

Champs-sur-Marne

77455 Marne la Vallée

France

Table of contents

Chapter 1

Introduction en français

Contents

1.1 Contexte

Selon la définition d'`UVS International`, un drone (UAV) est un avion générique conçu pour fonctionner sans pilote humain à bord (Remondino et al. [2011]). Dans le passé, le développement de systèmes et de plateformes UAV reposait principalement sur des objectifs militaires. De nos jours, les systèmes UAV jouent un rôle croissant dans le domaine de la géomatique. Le drone ouvre de nouvelles applications dans la photogrammétrie aérienne rapprochée et introduit une alternative peu coûteuse à la photogrammétrie aérienne classique (Colomina and de la Tecnologia [2008]; Eisenbeiß [2009]).

La cartographie de corridor, largement utilisée pour le suivi et la gestion des infrastructures — les autoroutes, les voies ferroviaires, les voies navigables et les oléoducs, est l'un des domaines d'importance majeure pour la photogrammétrie par drone. Ce travail de thèse est un projet de recherche en partenariat entre l'`Institut National de l'Information Géographique et Forestière` (`IGN`) et la `Compagnie Nationale du Rhône` (`CNR`). L'objectif est d'utiliser la cartographie de corridor pour réaliser le suivi des ouvrages hydrauliques de la `CNR`, et plus particulièrement des digues.

Malgré le développement rapide des plateformes UAV, des capteurs embarqués et des solutions logicielles de traitement de données, la cartographie de corridor reste difficile à cause de sa géométrie particulière. Dans ce travail, la scène d'intérêt est relevée à des fins d'auscultation. Différentes méthodes sont étudiées pour améliorer la préci-

sion de la cartographie afin de détecter le plus précocement possible des mouvements signalant des défauts potentiels.

1.1.1 IGN

L'Institut National de l'Information Géographique et Forestière (IGN), anciennement nommé Institut Géographique National, est un établissement public français. Fondé en 1940, il produit et gère des informations géographiques pour la France métropolitaine et ses départements et territoires d'outre-mer. Il développe en permanence de nouveaux produits et géo-services pour répondre aux besoins croissants et évolutifs de données cartographiques et d'informations géolocalisées. Grâce aux UMR (Unité Mixte de Recherche) auquels l'institut participe, l'UMR LaSTIG (Laboratoire en Sciences et Technologies de l'Information Géographique), l'UMR IPGP (Institut de Physique du Globe de Paris) et Lif (Laboratoire d'inventaire forestier), l'IGN maintient un haut potentiel d'innovation dans les domaines de la géodésie, de la topographie vectorielle, du traitement d'images et de l'inventaire forestier.

Le travail de cette thèse est réalisé au sein de l'équipe de recherche ACTE du laboratoire LaSTIG. L'équipe de recherche se concentre sur les méthodes et les outils permettant l'acquisition de données géoréférencées et structurées géométriquement. Ses activités de recherche consistent en :

- conception, production et calibration d'instruments métrologiques innovants ;
- estimation fine de la pose et recherche d'images par le contenu ;
- modélisation du signal électromagnétique pour une interprétation physique des images ;
- structuration géométrique et compréhension de la scène.

1.1.2 CNR

La Compagnie Nationale du Rhône (CNR) produit le quart de l'hydroélectricité française et est le premier producteur français d'énergie exclusivement renouvelable. En tant que concessionnaire du Rhône, la CNR gère la navigation sur le fleuve et agit quotidiennement pour assurer la maintenance et la sécurité de ses équipements. La CNR possède notamment un patrimoine de 50 barrages, écluses, centrales hydroélectriques et 400 km de digues.

Le laboratoire CACOH de la CNR est le garant de 80 années d'expérience dans le domaine de l'hydroélectricité et du développement des cours d'eau. Le CACOH se concentre maintenant sur la maîtrise des risques hydrauliques et l'optimisation du fonctionnement des structures. À la pointe de la technologie, il contribue à faire en sorte que la CNR soit en mesure de garantir le plus haut niveau de sureté.

1.1.3 Surveillance de digue

Les digues sont des structures hydrauliques artificelles qui régulent les niveaux d'eau. Elles sont sous l'influence continue des conditions météorologiques et des régimes fluviaux variables. Il est donc très important de surveiller la déformation et de localiser les zones vulnérables pour un traitement en amont.

Pour cette étude, la digue de *La Pallière* de la CNR a été choisie comme site d'intérêt (cf. Figure. 1.1). Cette digue est située sur le Rhône à Culoz, France et a été construite dans les années 1980. Soumise à des tassements depuis sa construction, cette portion de digue fait l'objet d'une surveillance spécifique. Actuellement, la CNR utilise principalement trois procédures de surveillance des digues et de détection des défauts sur le site de *La Pallière* : la surveillance visuelle, la surveillance de la charge hydraulique interne et la surveillance altimétrique.

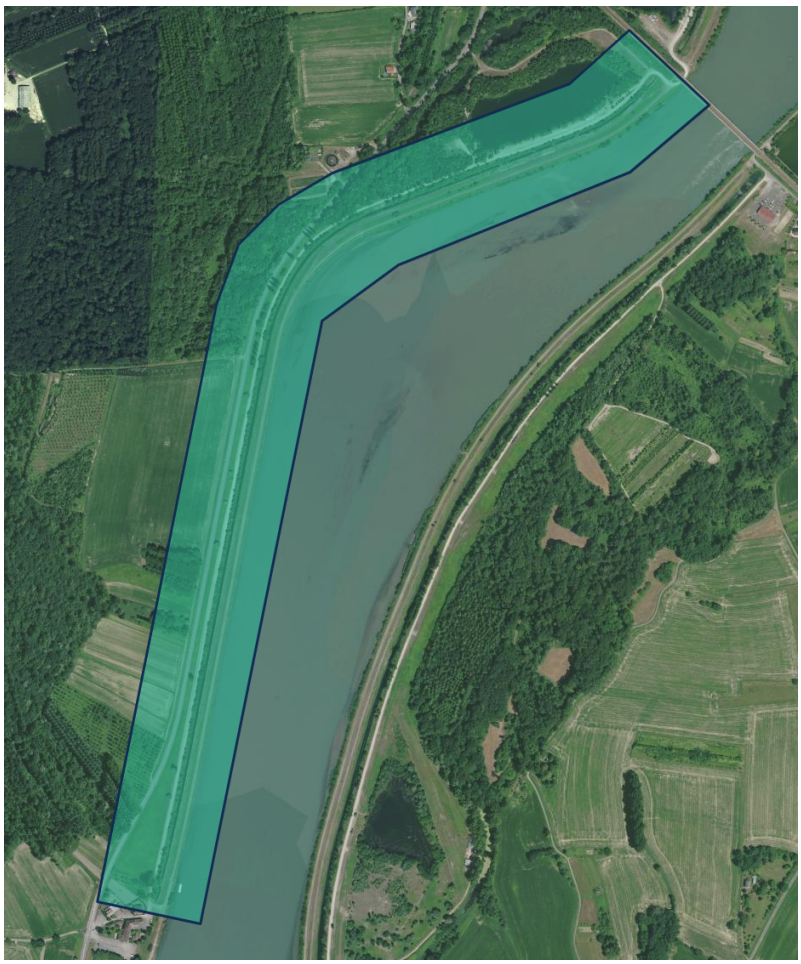

Figure. 1.1 – Le site d'intérêt, *La Pallière*.

Surveillance visuelle Des techniciens effectuent une inspection visuelle à la recherche de défauts visibles tels que des fuites, des affaissements ou tout signe d'avertissement. La surveillance visuelle est efficace pour détecter les signes visibles de défauts. C'est le premier niveau de détection.

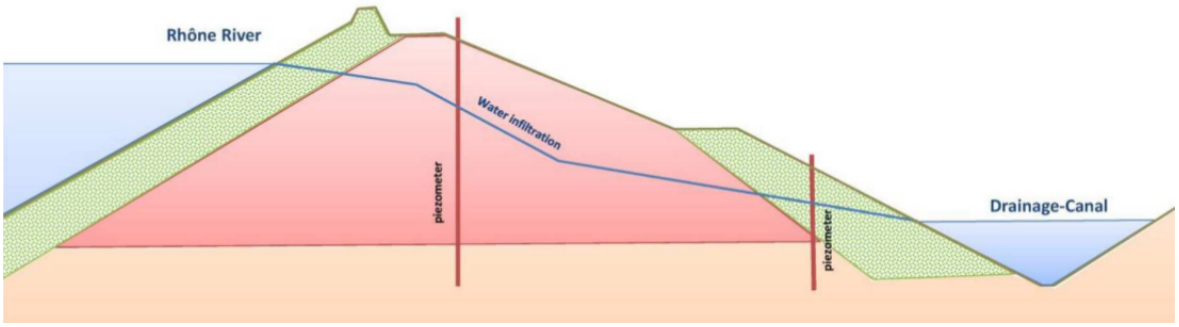

Figure. 1.2 – Un profil transversal de la digue et l'installation de piézomètres. Source : rapport interne du CNR.

Surveillance de la charge hydraulique interne Les digues du Rhône ne sont pas étanches et sont donc conçues pour subir continuellement une charge hydraulique. Des piézomètres sont installés tous les 300 à 500 mètres sur les profils transversaux de la digue (Figure 1.2). Les mesures piézométriques permettent de suivre le rabattement hydraulique entre le Rhône et le canal de drainage. Cette auscultation permet de vérifier le bon fonctionnement hydraulique de l'ouvrage.

Surveillance altimétrique Outre les mesures piézométriques, un réseau de référence altimétrique est installé le long de la structure et régulièrement examiné par nivellement direct. La surveillance altimétrique permet de suivre l'évolution du profil de la structure avec une précision millimétrique sur les points mesurés. Un éventuel affaissement peut être identifié en comparant les profils mesurés à différents moments.

1.2 Besoins et attentes

Le réseau de piézomètres et de références altimétriques permet une surveillance de points identifiés de la digue. Cependant, une surveillance globale ne peut être réalisée, un éventuel défaut entre deux points mesurés peut être négligé. La `CNR` et l'`IGN` établissent donc un partenariat développant des méthodes d'acquisition permettant un suivi 3D dense de la digue. À cette fin, des acquisitions Lidar terrestres et aériennes ont été réalisées dans certaines zones. Un suivi 3D dense peut être réalisée, cependant, ce type d'acquisition reste coûteux (l'application sur une grande surface est limitée), fastidieux (stations multiples, temps d'acquisition important) et insatisfaisant sur la précision finale (précision décimétrique).

L'érosion interne, première cause de rupture de digues, est l'intérêt central du projet `ERINOH` (érosion interne des ouvrages hydrauliques), lancé en 2006 et regroupant 75 organisations collaboratrices. Des tests sur des modèles physiques sont réalisés au sein de `CACOH` (Beguin [2011]), l'étude montre que certaines érosions internes peuvent provoquer des déformations à la surface de la digue (cf. Figure. 1.3). Un effondrement à petite échelle de plusieurs centimètres peut être le signal d'une érosion interne. La détection de ces changements est donc importante pour la surveillance des digues et la prévention des risques.

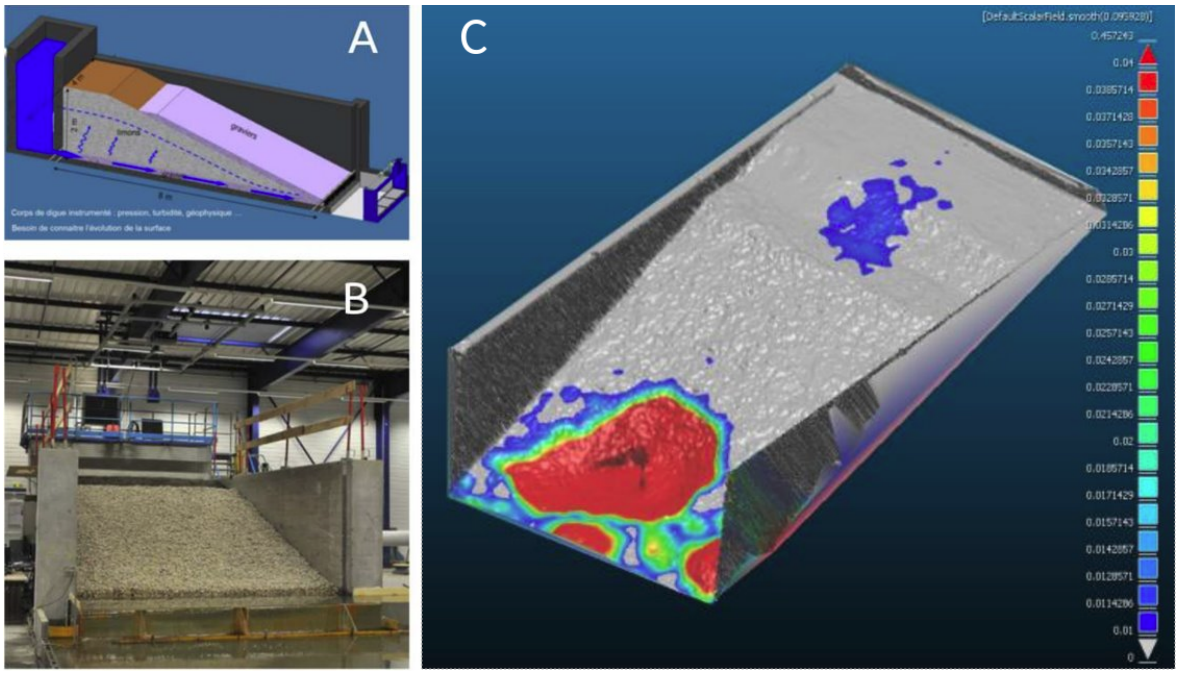

Figure. 1.3 – **A et B** : modèle physique dans lequel l'érosion interne est simulée. **C** : comparaison de modèles 3D dans le cas d'un tassement. Source : rapport interne de la CNR, Beguin [2011]; Tournadre [2015].

C'est ici que la photogrammétrie aérienne devient intéressante. Les modèles de surface topographiques de haute précision et l'analyse diachronique permettent de détecter les défauts de la digue avant que des dommages graves ne se produisent. Dans le cadre de l'optimisation de ses méthodes de surveillance et d'auscultation, la CNR étudie depuis 2011 l'usage des drones et de la photogrammétrie comme moyen complémentaire aux méthodes traditionnelles. Le drone en tant que vecteur offre de multiples avantages : les acquisitions peuvent être effectuées même sur des sites inaccessibles par voie terrestre, la durée d'acquisition est plus courte, le coût d'acquisition est inférieur.

La CNR espère obtenir comme résultat final un modèle de surface numérique (DSM), sous la forme de nuage de points. Dans le cas d'une surveillance régulière, une précision centimétrique est attendue. En cas d'intervention à la suite d'un événement exceptionnel, une précision de 3 cm est attendue (cf. Table. 1.1). Pour répondre à ces attentes, la CNR et l'IGN ont collaboré sur une première thèse portant sur le suivi de digue par photogrammétrie par drone. La thèse Tournadre [2015], démarrée en 2012, avait utilisé des caméras grand public non équipées de système GNSS embarqué. Cette thèse avait mis au point un protocole d'acquisition et de traitement permettant d'arriver à une précision centimétrique avec un point d'appui tous les 100 m. Bien qu'il réponde aux attentes de la CNR, le besoin en densité de points d'appui reste une limitation forte pour le déploiement opérationnel. L'objectif de la présente thèse est d'arriver à la même précision avec peu ou pas de point d'appuis, en bénéficiant des progrès du matériel d'acquisition (caméras photogrammétriques et système GNSS embarqué) et en optimisant les méthodes d'acquisition et de traitement. De nos jours, une reconstruction 3D dense peut être réalisée avec des solutions de pointe. Par conséquent, l'accent de notre thèse sera mis sur l'obtention des orientations intérieure et extérieure de la caméra d'une haute précision.

Type d'Acquisition	Fréquence d'Acquisition	Longueur de Scène	Précision Attendue	Besoin
Régulier	1 fois/an	jusqu'à 1 km	1 cm	Détection de déformations pour la surveillance d'une zone sensible bien définie.
Exceptionnel	si nécessaire	plusieurs kilomètres	3 cm	Comparaison à un état initial après un événement exceptionnel.

Table. 1.1 – Besoins et attentes de la CNR pour la surveillance de digues.

1.3 Organisation et contributions

Au cours de ce travail de thèse, nous étudions trois méthodes qui améliorent la précision des mesures 3D dans des acquisitions photogrammétriques aériennes pour une scène de configuration corridor, tout en minimisant le nombre de points de contrôle au sol.

Une brève présentation de l'état de l'art est donnée dans le **Chapitre 3**. La présentation couvre dans un premier temps les plateformes UAV et les systèmes de navigation embarqués, la photogrammétrie par drones mettant l'accent sur l'orientation des capteurs et la cartographie des corridors. Ensuite, le matériel et les logiciels liés à ce travail sont présentés.

Pour optimiser le protocol d'acquisition et de traitement, il faut prendre compte de tous les aspects de la chaine de travail. Pour orienter la recherche, des études sont effectuées premièrement avec des simulations dans le **Chapitre 4**, sur des problèmes qui nous intéressent potentiellement. En examinant les problèmes avec la simulation, nous obtenons un aperçu du problème avant de déterminer l'axe de recherche et de mener des enquêtes approfondies. Les problèmes abordés dans ce chapitre incluent : la focale erronée dans la précalibration de la caméra et l'influence des images obliques ; la focale progressivement modifiée en raison de l'effet thermique de la caméra ; et l'effet de l'obturateur roulant. Des investigations approfondies sont ensuite menées sur ces trois aspects.

Dans le **Chapitre 5**, nous abordons d'abord la géométrie de l'acquisition aérienne pour la cartographie de corridor, des expériences sur des jeux de données réels sont ménées et analysées. L'influence des images obliques et des images nadir de plusieurs hauteurs de vol est étudiée. La possibilité de la calibration de caméra en vol et son application à une géométrie d'acquisition défavorable sont examinées.

Le **Chapitre 6** se concentre sur l'amélioration de la performance des caméras métriques. La déformation thermique dans l'espace image introduite par la variation de température des caméras métriques est étudiée. La déformation thermique est modélisée avec deux méthodes indépendantes pour l'auto-vérification. Une correction des effets thermiques est proposée pour améliorer la précision des mesures 3D. La performance de la correction proposée est évaluée sur un jeu de données terrestre linéaire et sur un jeu de données aérien de cartographie de corridor.

À la fin, nous prenons du recul pour regarder la chaine de travail dans l'ensemble. Une précision de cartographie élevée peut être obtenue avec une géométrie d'acquisition optimisée et une modélisation appropriée de la caméra métrique. Nous nous posons la

question si les plateformes d'UAV grand public peuvent atteindre le même niveau de précision après des traitements nécessaires. Le **Chapitre 7** étudie un problème majeur qui limite la performance des caméras grand public, l'effet de l'obturateur roulant. Deux méthodes sont proposées pour calibrer le temps de lecture d'une caméra à obturateur roulant. Une approche est proposée et implémentée pour la correction de la déformation de l'image introduite par l'effet de l'obturateur roulant. La performance de la correction est évaluée sur les jeux de données de configuration de blocs et de corridors.

Enfin, les conclusions et les perspectives sont données dans le **Chapitre 8**.

Le travail de la thèse est présenté sous la forme de publications. Pour chaque sujet traité, les publications associées sont répertoriées au début du chapitre. Ici, un résumé des publications est donné comme suit :

Revue internationale avec comité de lecture

- **Zhou, Y.**, Daakir, M., Rupnik, E., Pierrot-Deseilligny, M. (2020). A two-step approach for the correction of rolling shutter distortion in UAV photogrammetry. *ISPRS journal of photogrammetry and remote sensing, 160*, 51-66.
- **Zhou, Y.**, Rupnik, E., Meynard, C., Thom, C., Pierrot-Deseilligny, M (2020). Simulation and Analysis of Photogrammetric UAV Image Blocks : Influence of Camera Calibration Error. *Remote Sensing, 12*(1), 22.
- Daakir, M., **Zhou, Y.**, Pierrot-Deseilligny, M., Thom, C., Martin, O., Rupnik, E. (2019). Improvement of photogrammetric accuracy by modeling and correcting the thermal effect on camera calibration. *ISPRS journal of photogrammetry and remote sensing, 148*, 142-155.
- **Zhou, Y.**, Rupnik, E., Faure, P. H., Pierrot-Deseilligny, M. (2018). GNSS-assisted integrated sensor orientation with sensor pre-calibration for accurate corridor mapping. *Sensors, 18*(9), 2783.

Conférence internationale avec comité de lecture

- **Zhou, Y.**, Rupnik, E., Meynard, C., Thom, C., Pierrot-Deseilligny, M. (2019). Simulation and Analysis of Photogrammetric UAV Image Blocks : Influence of Camera Calibration Error. *ISPRS Annals of Photogrammetry, Remote Sensing and Spatial Information Sciences*, 195-200.

Conférence nationale avec comité de lecture

- **Zhou, Y.**, Rupnik, E., Faure, P. H., Pierrot-Deseilligny, M. (2018). GNSS-assisted accurate corridor mapping with small UAV. *Congrès CFPT, 25-28 june 2018, Paris, France.*

Poster

- Reconstruction 3D de scène type corridor à partir d'images aériennes et de données GNSS. **Zhou, Y.**, Rupnik, E., Pierrot-Deseilligny, M. *Les* 28^{es} *journées de la Recherche de l'IGN, 18-19 april 2019, Paris, France.*

Chapter 2

Introduction

Contents

2.1 Context

According to the definition of `UVS International`, a UAV is a generic aircraft designed to operate with no human pilot on-board (Remondino et al. [2011]). In the past, the development of UAV systems and platforms are mostly driven by military purposes. Nowadays, UAV systems are taking an increasing role in geomatics field. UAV photogrammetry opens various new applications in close-range aerial domain and introduces a low-cost alternative to classical manned aerial photogrammetry (Colomina and de la Tecnologia [2008]; Eisenbeiß [2009]).

One of the fields with substantial importance for UAV photogrammetry is the corridor mapping, which is largely used in the surveillance and management of infrastructure assets – highways, railways, waterways and pipelines. This thesis work is a research project in partnership between the `Institut National de l'Information Géographique et Forestière` (`IGN`) and the `Compagnie Nationale du Rhône` (`CNR`). The aim is to apply corridor mapping in the monitoring and maintenance of CNR's hydraulic facilities – the dikes.

Despite the rapid development of UAV platforms, on-board sensors and data processing software solutions, corridor mapping remains challenging due to its special geometry. In this work, the scene of interest is surveyed for monitoring purposes. Different methods are investigated for the improvement of the mapping accuracy to detect as early as possible the movements that indicate potential defects.

2.1.1 IGN

The Institut national de l'information géographique et forestière (IGN), previously named Institut géographique national, is a French public state administrative establishment. Founded in 1940, it produces and maintains geographical information for France and its overseas departments and territories. It develops constantly new products and geoservices to meet the growing and evolving needs for cartographic data and geolocalized information. Thanks to the research laboratories in which the institute is involved, the UMR LaSTIG (Laboratory in Geographical Information Science and Technology), the UMR IPGP (Institute of Physics of the Globe of Paris) and the Lif (Forest Inventory Laboratory), the IGN maintains a high level of innovation potential in the fields of geodesy, vector topography, image processing and inventory forest.

The work of this thesis is carried out within the research team ACTE of the laboratory LaSTIG. The research team focuses on all methods and tools which allows for the acquisition of georeferenced and geometrically structured data. Its research activities consist of

- design, production and calibration of innovative metrological instruments
- fine pose estimation and content-based image retrieval
- modeling of electromagnetic signal for physical interpretation of images
- geometric structuring and scene understanding

2.1.2 CNR

The Compagnie Nationale du Rhône (CNR) produces a quarter of France's hydroelectricity and is France's leading producer of exclusively renewable energy. As the concessionary of the Rhône, the CNR manages navigation on the river and acts daily to ensure its maintenance and equipment safety. In particular, the CNR has a portfolio of 50 dams, locks, hydroelectric plants and 400 km of dikes.

The laboratory CACOH of CNR, is the result of 80 years' experience in hydroelectricity and river developments. The CACOH now focuses on controlling hydraulic risks and optimising the operation of the structures. At the leading edge of technology, it contributes to ensuring that CNR is capable of guaranteeing the highest level of safety.

2.1.3 Dike surveillance

Dikes are the artificial hydraulic structures which regulate water levels. They are under continuous influence of weather and variable river regimes. It is therefore of great importance to monitor the deformation and to locate vulnerable spots for early treatment.

For this study, the dike *La Pallière* of CNR is chosen as the site of interest (cf. Figure. 2.1). This dike is located on the Rhône at Culoz, France and was built in the 1980s.

Subject to settlements since its construction, this portion of dike requires a specific monitoring. Currently, the `CNR` operates mainly three procedures for dike surveillance and defect detection at the site `La Pallière` : the visual surveillance, the internal hydraulic load surveillance and the altimetric surveillance.

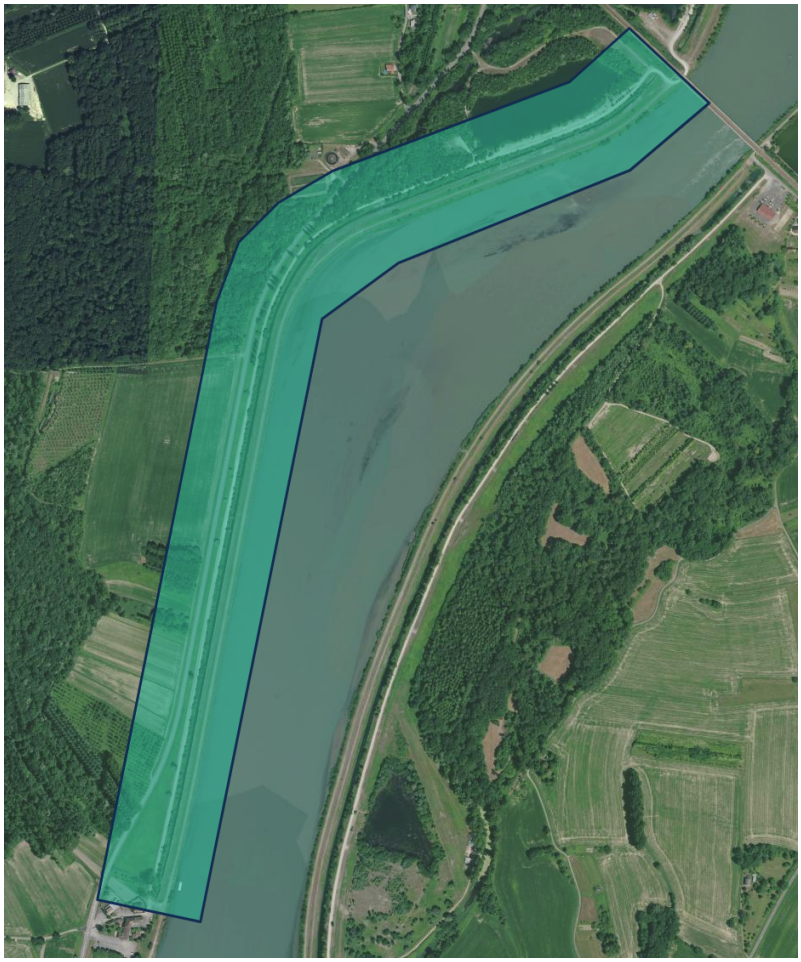

Figure. 2.1 – The site of interest, *La Pallière*.

Visual surveillance Technicians inspect visually in search of visible defects such as leaks, collapses or any warning signs. Visual surveillance is effective for detecting visible signs of defects. It is the first level of detection.

Internal hydraulic load surveillance The dikes of the Rhône are not waterproof and are therefore designed to undergo a continuous hydraulic load. Piezometers are installed on the transversal profiles of the dike every 300 to 500 meters (Figure 2.2). Piezometric measurements make it possible to monitor hydraulic drawdowns between the Rhône and the drainage canal. This surveillance makes it possible to verify the good hydraulic functioning of the structure.

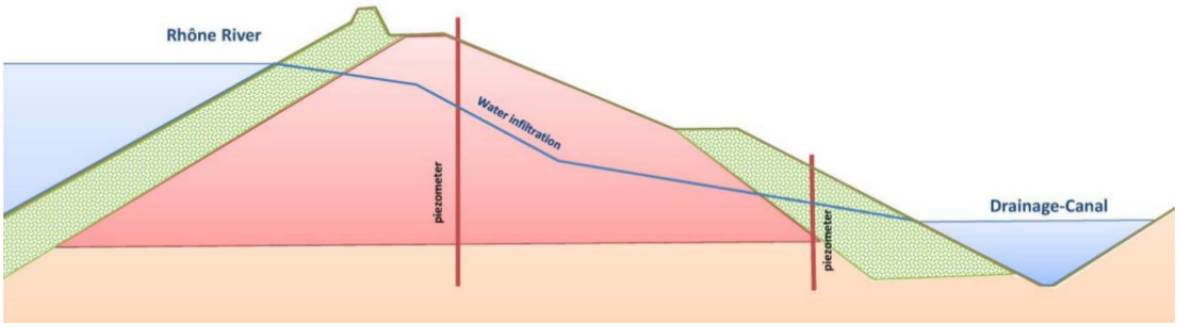

Figure. 2.2 – A transversal profile of the dike and the installation of piezometers. Source : CNR internal report.

Altimetric surveillance In addition to piezometric measurements, an altimetric reference network is installed along the structure and regularly examined by direct leveling. The altimetric surveillance makes it possible to follow the evolution of the structure profile with a millimeter accuracy on measured points. A possible collapse can be identified by comparing profiles measured at different times.

2.2 Needs and expectations

The network of piezometers and altimetric references allows for a punctate surveillance of the dike. However, a global monitoring can not be achieved, a possible defect between two measured points can be neglected. The `CNR` and the `IGN` establish therefore a partnership developing acquisition methods that allows for a continuous geometric surveillance of the dike. For this purpose, terrestrial and aerial Lidar acquisitions have been conducted on certain areas. Yet a continuous surveillance can be achieved, this kind of acquisition remains expensive (the application on large area is limited), tedious (multiple stations, important acquisition time) and unsatisfying on the final accuracy (decimetric accuracy).

Internal erosion, the first cause of dike breakdowns, is the central interest of the project ERINOH (Internal Erosion of Hydraulic works) which debuted in 2006 and has 75 collaborate organizations. Tests on physical models are carried out within CACOH (Beguin [2011]), the study shows that certain internal erosion can cause deformations on the surface of the dike (cf. Figure. 2.3). Small-scale collapse of several centimeters may be a precursor of the internal erosion, the detection of these changes is therefore important for dike surveillance and risk prevention.

This is where aerial photogrammetry becomes interesting. High-precision topographic surface models and diachronic analysis make it possible to detect disorders of the dike before severe damages take place. In order to optimize its surveillance and monitoring methods, the `CNR` has been studying since 2011 the combination of drones and photogrammetry as a mean of complementing traditional methods. The drone being the carrier offers multiple advantages : acquisitions can be performed even on sites that are difficult to access by land, the acquisition time is shorter, the acquisition cost is lower.

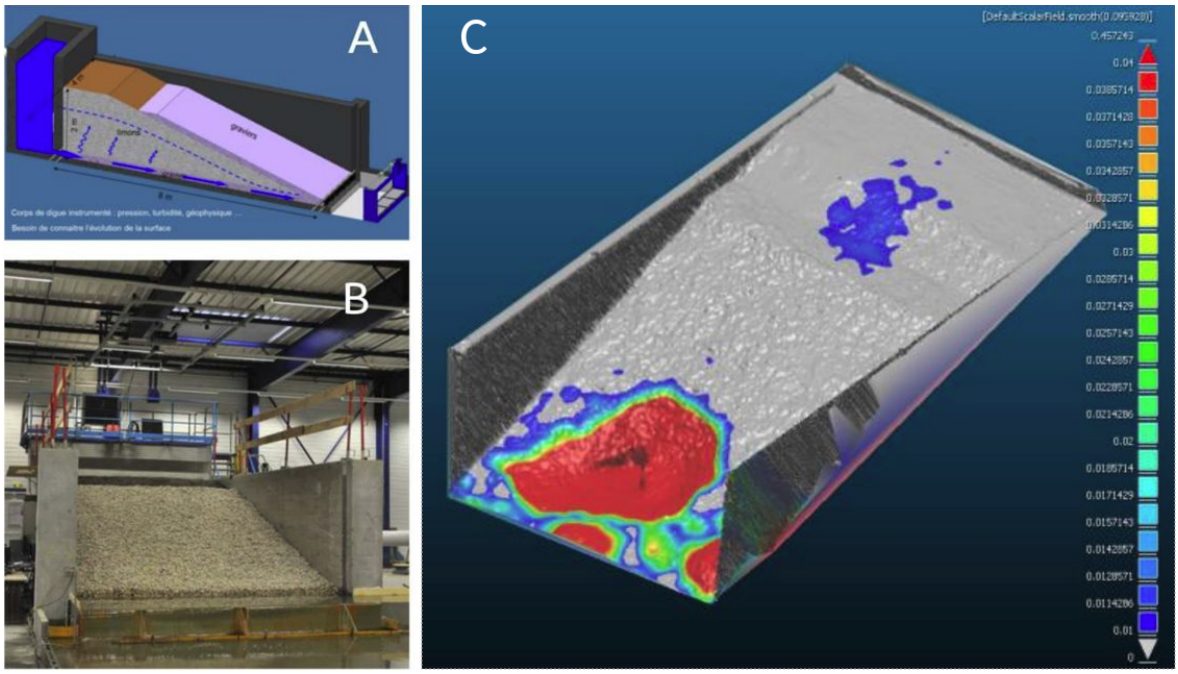

Figure. 2.3 – **A and B** : physical model in which the internal erosion is simulated. **C** : 3D model comparison result in the case of a collapse. Source : CNR internal report, Beguin [2011]; Tournadre [2015].

The CNR expects to obtain as final result a digital surface model (DSM), in the form of cloud points. In the case of regular monitoring, a centimetric accuracy is expected. In the case of an intervention following an exceptional event, an accuracy of 3 cm is expected (cf. Table. 2.1). To meet these expectations, the CNR and the IGN collaborated on a first thesis to apply UAV photogrammetry in dike monitoring. The thesis Tournadre [2015], started in 2012, performed UAV photogrammetric acquisitions with consumer grade cameras that were not equipped with on-board GNSS system. This thesis had develeoped a protocol of UAV acquisition and data processing, allowing to reach centimetric accuracy with one ground control point every 100 m. Though it meets the expectations of the CNR, the need of a dense ground control point network remains a strong limitation. The objective of our thesis work is, by benefiting from the development of acquisition equipment (e.g. metric cameras and embedded GNSS system) and optimizing acquisition and data processing methods, to achieve the same level of mapping accuracy with less or zero ground control points. A 3D dense reconstruction can nowadays be solved with state-of-the-art solutions. Therefore, the focus of our thesis will be given to obtaining camera interior and exterior orientations with high accuracy.

Acquisition Type	Acquisition Frequency	Length of Scene	Expected Accuracy	Need
Regular	1 time/year	up to 1 km	1 cm	Detection of deformations for the monitoring of a well defined sensitive area.
Exceptional	when needed	several kilometers	3 cm	Comparison to an initial state after an exceptional event.

Table. 2.1 – Needs and expectations of CNR for dike surveillance.

2.3 Organization and contributions

In this work, we investigate three methods that improve the 3D measurement accuracy of aerial photogrammetric acquisitions for a scene of corridor configuration, while minimizing the number of ground control points.

A brief presentation of the state of the art is given in **Chapter 3**. The presentation covers firstly UAV plateforms as well as on-board navigation systems, UAV photogrammetry with emphasis on sensor orientation and the corridor mapping. Afterwards, hardware and software related to this work are introduced.

To optimize the data processing method, considerations should be given to every step since they affect each other in one way or another. To orient the research direction, studies are carried out with simulations in **Chapter 4** on several problems that interest us potentially. By investigating the issues with simulation in the first place, we get to have an insight on the addressed problem before determining the research focus and taking thorough investigations. The addressed problems include : erroneous focal length in camera pre-calibration and the influence of oblique images ; gradually varied focal length due to thermal effect of the camera ; and the rolling shutter effect. Then, thorough investigations are conducted on these three aspects.

In **Chapter 5**, we first tackle the aerial acquisition geometry for corridor mapping, real-case experiments are conducted and analyzed. The influence of oblique images and nadir images of multiple flight heights are investigated. The possibility of an in-flight camera calibration and its application on unfavourable acquisition geometry is examined.

Chapter 6 focuses on the performance improvement for metric cameras. The thermal deformation in image space introduced by temperature variation of metric cameras is studied. The thermal deformation is modeled with two independent methods for auto-verification. A thermal effect correction is proposed to improve the 3D measurement accuracy, the performance of the proposed correction is evaluated on one linearly acquired terrestrial dataset and one aerial corridor mapping dataset.

At the end, we take a step back to view the global acquisition flow. A high mapping accuracy can be achieved with optimized acquisition geometry and proper modeling of metric camera. Yet, can consumer-grade UAV platforms achieve the same level of accuracy after necessary processing ? **Chapter 7** studies one major problem that limits the performance of consumer-grade cameras, the rolling shutter effect. Two methods are proposed to calibrate the readout time of rolling shutter camera. An approach is proposed and implemented for the correction of image deformation introduced by the rolling shutter effect. The performance of the correction approach is evaluated on both block and corridor configuration datasets.

Finally, conclusions and perspectives are given in **Chapter 8**.

The work of the thesis is presented in the form of published articles. For each addressed topic, related publications are listed at the beginning of the chapter. Here, a summary of publications is given as follows :

International journal with peer review

- **Zhou, Y.**, Daakir, M., Rupnik, E., Pierrot-Deseilligny, M. (2020). A two-step approach for the correction of rolling shutter distortion in UAV photogrammetry. *ISPRS journal of photogrammetry and remote sensing, 160*, 51-66.
- **Zhou, Y.**, Rupnik, E., Meynard, C., Thom, C., Pierrot-Deseilligny, M (2020). Simulation and Analysis of Photogrammetric UAV Image Blocks : Influence of Camera Calibration Error. *Remote Sensing, 12*(1), 22.
- Daakir, M., **Zhou, Y.**, Pierrot-Deseilligny, M., Thom, C., Martin, O., Rupnik, E. (2019). Improvement of photogrammetric accuracy by modeling and correcting the thermal effect on camera calibration. *ISPRS journal of photogrammetry and remote sensing, 148*, 142-155.
- **Zhou, Y.**, Rupnik, E., Faure, P. H., Pierrot-Deseilligny, M. (2018). GNSS-assisted integrated sensor orientation with sensor pre-calibration for accurate corridor mapping. *Sensors, 18*(9), 2783.

International conference with peer review

- **Zhou, Y.**, Rupnik, E., Meynard, C., Thom, C., Pierrot-Deseilligny, M. (2019). Simulation and Analysis of Photogrammetric UAV Image Blocks : Influence of Camera Calibration Error. *ISPRS Annals of Photogrammetry, Remote Sensing and Spatial Information Sciences*, 195-200.

National conference with peer review

- **Zhou, Y.**, Rupnik, E., Faure, P. H., Pierrot-Deseilligny, M. (2018). GNSS-assisted accurate corridor mapping with small UAV. *Congrès CFPT, 25-28 june 2018, Paris, France.*

Poster

- Reconstruction 3D de scène type corridor à partir d'images aériennes et de données GNSS. **Zhou, Y.**, Rupnik, E., Pierrot-Deseilligny, M. *Les* 28^{es} *journées de la Recherche de l'IGN, 18-19 april 2019, Paris, France.*

Chapter 3

State of the art

Contents

3.1 UAV plateforms

An UAV is a generic aircraft designed to operate without a human pilot aboard (http://www.uvs-international.org/). With the development of unmanned aerial vehicle (UAV) platforms, it has become nowadays a valuable source of data for inspection, surveillance, mapping and 3D modeling issues (Nex and Remondino [2014]).

The primary airframe types are fixed and rotary wings. Both categories can fly in manual, semi-automated and autonomous modes. Depending on the on-board instrumentation, payload, flight autonomy, type of platform and degree of automation needed, a typical UAV platform for geomatics purposes can cost from 1000€ up to 50000€. Among diverse on-board instrumentation, the embedded navigation system provides

aerial control of position, orientation and velocity from measurements of GNSS and IMU systems.

3.1.1 GNSS

GNSS refers to the Global Navigation Satellite System, which contains a constellation of satellites for providing geo-spatial positions. As of August 2019, three GNSS systmes are fully operational and provide global services, the `Global Positioning System` (`GPS`) of the United States, the `GLObal NAvigation Satellite System` (`GLONASS`) of Russia and the `BeiDou Navigation Satellite System` (`BDS` or `COMPASS`) of China. The `Galileo` system of the European Union is expected to be fully operational by 2020. The `Quasi-Zenith Satellite System` (`QZSS`) of Japan is a regional time transfer system and a `GPS` satellite-based augmentation system, it aims to enhance the accuracy of `GPS` in Japan and its neighbouring area ; a `GPS`-independent satellite navigation system is scheduled for 2023. India has functioning `Indian Regional Navigation Satellite System` (`IRNSS`) with an operational name of `NAVIC`, it is an autonomous regional satellite navigation system that provides accurate real-time positioning and timing services.

In GNSS processing, the positions are computed with range measurements to the satellites and triangulation techniques. The positions can either be calculated in absolute (single point) mode or in relative (differential) mode. In absolute mode, the position of the GNSS antenna is determined directly from the observations and the position of the satellites, in the same reference frame. In relative mode, the vector separating the antenna of unknown position and one or more reference stations is estimated. This is more accurate since it eliminates systematic errors (broadcast ephemeris, atmospheric effects, clock errors) by realizing differences in observations between stations (Figure 3.1).

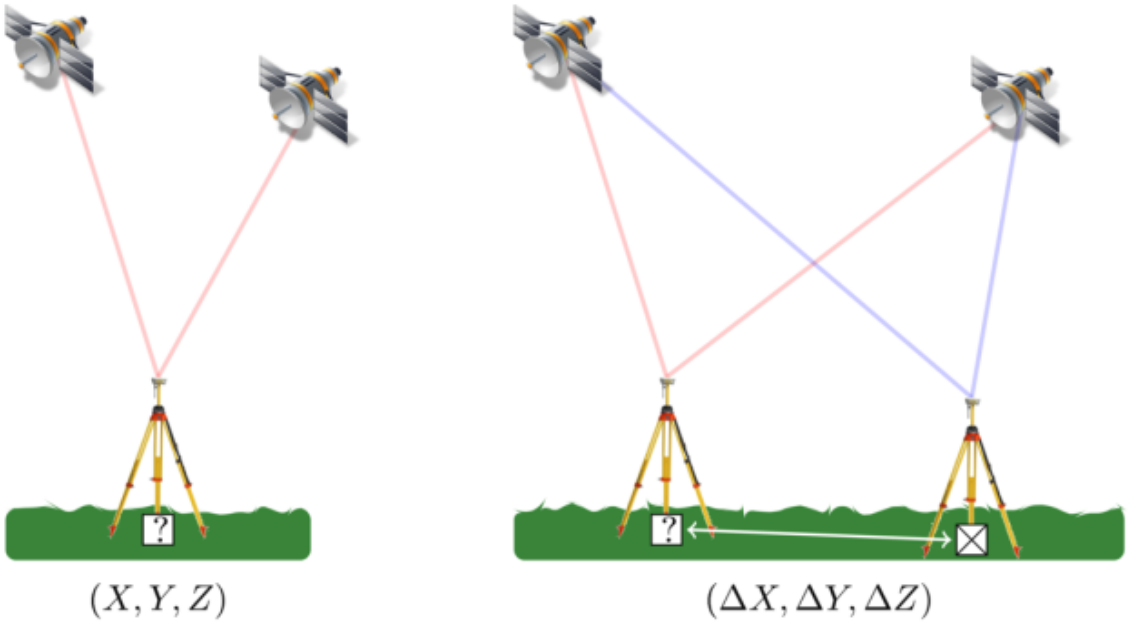

Figure. 3.1 – absolute mode (left) and relative mode (right) of positioning

The range to the satellites can be measured either with the code measurement or

phase measurement. When measuring with code, the signal travel time is determined by comparing the ”pseudo random code” generated by the receiver with an identical code contained in the signal and the result is precise to the meter level. As for phase measurement, the range to a satellite is expressed in units of cycles of the carrier frequency ; as long as the integer number of wavelengths (approximately 19 cm) to each satellite can be determined, decimeter accuracy can be obtained.

3.1.2 IMU

An inertial measurement unit (IMU) is an electronic device that measures the specific force and angular rate of a body with triads of accelerometers and gyros. The position, velocity and orientation are then computed with Newton's equations of motion on the rotating earth by integrating acceleration and angular rates sensed by the IMU. The IMU is required to be initialized with known position and velocity from GNSS, and aligned with respect to the true vertical and true North. The alignment sets the local-level mathematical frame of reference of the computation. The solution that IMU produces is dynamically accurate ; however, since an integration process is performed, any errors in the accelerometers and gyros will integrate into slowly growing position, velocity and orientation errors.

3.1.3 GNSS-aided INS

GNSS-aided inertial navigation system (INS) is comprised of four main components : an IMU, a low-noise GNSS receiver, a real-time computer system and a post-processing software suite. The software implements the sophisticated signal processing algorithms that couple GNSS measurements with the inertial navigation solutions, to produce a position and orientation solution that retains the dynamic accuracy of the inertial navigation solution but has the absolute accuracy of the GNSS.

To compute accurately the position and the attitude of an embedded sensor, several criteria are to be met (Hutton and Mostafa [2005]) :

— the IMU module need to be rigidly attached to the sensor to avoid flexure between the center of the sensor and the IMU

— the physical alignment of the IMU frame with respect to the sensor (boresight) need to be calibrated

— the offsets from the sensor center to the IMU and to the phase center of GNSS antenna (lever-arm) need to be calibrated

— the sensor system and the GNSS/INS system need to be synchronized

When the aforementioned criteria are met, the theoretical accuracy of the GNSS/INS navigation system can be at the centimeter level for position and millidegrees range for attitude (Mian et al. [2015]).

3.2 UAV Photogrammetry

According to the American Society for Photogrammetry and Remote Sensing, photogrammetry is the art, science and technology of obtaining reliable information about physical objects and the environment through the process of recording, measuring and interpreting photographic images (Jones [1982]; Rupnik et al. [2017]). It can also be summarized as the procedure of extracting three-dimensional measurements from two-dimensional data (i.e. images). Its combination with robotic, computer vision and geometric technologies has established a new paradigm of photogrammetry. Nowadays, large image block orientation is almost automatic thanks to the development of 3D reconstruction algorithms and software.

The first application of UAVs in Geomatics field took place three decades ago, but only recently UAVs became a common platform in Geomatics field (Nex and Remondino [2014]). UAV photogrammetry opens various new applications in the close-range aerial domain, offering a low-cost alternative to the classical manned aerial photogrammetry (Colomina and de la Tecnologia [2008]; Eisenbeiß [2009]). During the past two decades, UAV photogrammetry has undergone an unprecedented evolution thanks to the development of low-cost platforms, on-board imaging sensors and GNSS/INS systems.

One of the advantages of UAVs compared to manned aerial systems is that UAVs can be used under high risk situations without putting in danger the pilot. It can also be flown in areas that are difficult to access by land, at low altitude and close to the objects. The majority of commercially available UAV systems on the market focus on providing a low-cost solution, therefore advantages the cost of UAV photogrammetry.

3.3 Photogrammetry Processing

In general, the photogrammetric data processing consists of the following steps :

- Extraction of tie points
- Interior orientation
- Exterior orientation
- Georeferencing
- Least squares refinement
- Dense matching
- Product generation

More attention is given here to the interior/exterior orientations and their refinement.

3.3.1 Interior orientation

This step is to determine the interior parameters of the imaging sensor. The interior parameters normally include the camera focal length, the principal point and the camera distortion correction coefficients. The determination of interior orientation is also referred to as camera calibration.

Several mathematical models have been developed for the distortion correction when performing camera calibration. In general, these models fall into two categories. The first category consists of physical models which mitigate systematic errors according to their assumed physical behavior (Duane [1971]; Fraser [1997]; Schut [1979]). In the second category individual error sources are not explicitly treated. Instead, numerical models are designed to compensate the total systematic errors (Ebner [1976]; Gruen [1978]).

The camera calibration can be performed shortly before or after the photogrammetric acquisition (Remondino and Fraser [2006]). This is referred to as pre-calibration. The pre-calibration is often carried out in laboratory with convergent images and varying scene depth. Lichti et al. [2008] indicated that the laboratory camera calibration still has issues in the context of aerial photogrammetry since the depth of the calibration scene and the acquisition scene do not vary within the same scale and proposed an aerial approach for the camera calibration. The camera calibration can also be performed simultaneously within the self-calibrating bundle block adjustment and the interior orientation parameters are estimated as additional parameters.

3.3.2 Exterior orientation

The (absolute) exterior orientation settles the camera pose (camera orientation and camera position) in the absolute frame. It is always described by 3 rotation parameters and 3 position parameters. The exterior orientation is also referred to as the sensor orientation.

Indirect sensor orientation (InSO) For sensor orientation determination, the traditional method is bundle block adjustment (BBA). By performing the BBA procedure, exterior orientation parameters of every image are estimated with a network of ground control points (GCPs) and tie points. Therefore, the number of tie points, the number of GCPs as well as the well-establishment of the GCP network strongly influence the precision of photogrammetric products (Remondino et al. [2011]; Vallet et al. [2011]). However, the traditional BBA method requires a large amount of interactive editing and supervision of highly skilled operators; furthermore, the establishment of GCP networks can be substantially costly (Cramer et al. [2000]). Thereafter, this approach is referred to as indirect sensor orientation (InSO).

Direct sensor orientation (DiSO) With embedded GNSS system and inertial navigation system, it is possible to have knowledge of the position and orientation of aerial mapping sensors and every pixel of image is georeferenced to earth without any

ground information. This direct sensor orientation (DiSO) can eliminate the need of GCPs when precise observations are available and the robustness and accuracy can be enhanced (Colomina [1999]).

Integrated sensor orientation (ISO) The DiSO approach can be completed with several GCPs to improve the redundancy and to identify potential biases in GNSS/INS measurements (Ackermann [1992]; Heipke et al. [2002b]). The GNSS/INS data and image information are processed simultaneously to determine the exterior orientation parameters in a BBA procedure. This approach is called integrated sensor orientation (ISO).

The concept of InSO and DiSO are depicted in Figure 3.2. Compared to InSO, DiSO reduces significantly or eliminate the cost of the establishment of GCP network and makes remote locations accessible (Ip et al. [2004]). Since it does not require measurement of image coordinates, it is also the fastest among the above-mentioned three approaches. Nevertheless, it can not benefit from self-calibration and depends critically on the quality of GNSS/INS sensors and the accuracy of the measurements. ISO can include camera self-calibration and the potential bias in GNSS/INS-derived exterior orientation parameters can be corrected when several GCPs are available. While it is recommended to check the ISO results with independently determined ground check points, it is the only means of quality control for DiSO. Table 3.1 and 3.2 show the observations and properties of InSO, ISO and DiSO. ISO benefits from aerial control, image information and achieves comparable results with respect to InSO with less field labor work.

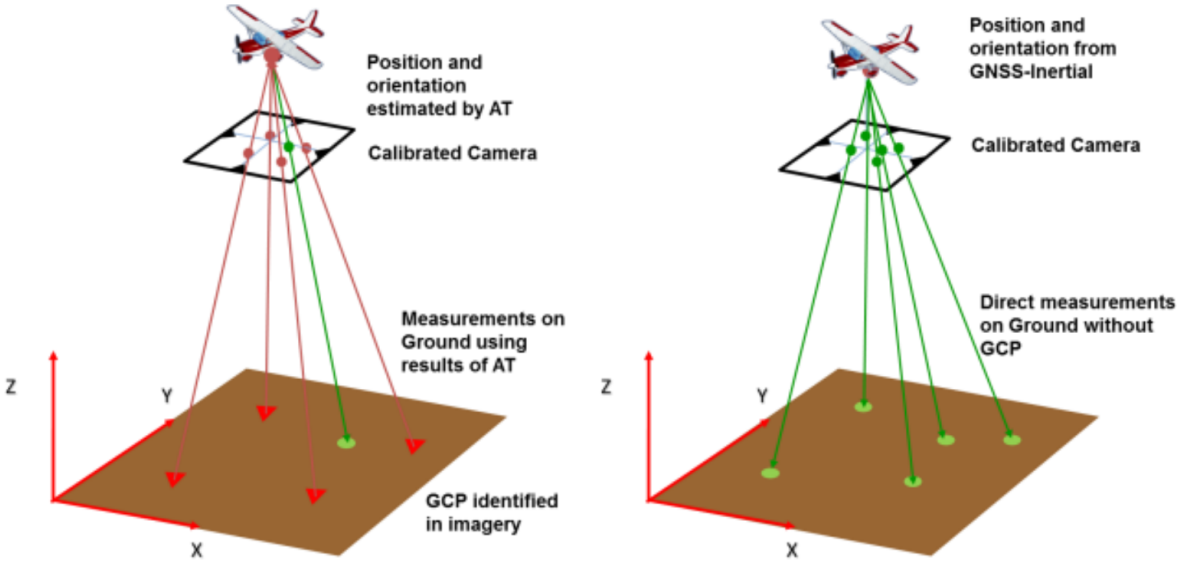

Figure. 3.2 – Indirect sensor orientation (left) versus direct sensor orientation (Mian et al. [2015])

Within the ISO realm, with accurate position aerial control, one can compete with geometric accuracies achieved by means of InSO and well distributed GCPs (Gerke and Przybilla [2016]; Mian et al. [2015]; Rehak and Skaloud [2016]; Skaloud et al. [2014]). However, accurate attitude control is more challenging to establish and the attitude measurements issued from low-cost IMU devices is not able to improve the quality of

Observations	InSO	ISO	DiSO
Aerial control	no	yes	yes
GCPs	yes, many	yes, few	no
Image coordinates	yes, many	yes, many	no

Table. 3.1 – Observations of InSO, ISO and DiSO

Properties	InSO	ISO	DiSO
Precision	+	+	-
Accuracy	+	+	-
Reliability	+	+	-
Cost	+	0	-
Time	+	0	-
+ : high	0 : average		- : low

Table. 3.2 – Properties of InSO, ISO and DiSO

final results (Jozkow and Toth [2014]; Pfeifer et al. [2012]). The limited availability of weight, power and volume in the UAV payload poses a major challenge for having high quality sensors. Certian studies propose a relative aerial control, instead of applying the absolute position and attitude for each image, the relative position and attitude information issued from the IMU is applied on successive images. Relative aerial control eliminates the need of boresight determination and the effect of possible systematic errors in satellite positioning is mitigated ; the procedure is simplified and is more resilient to poor geometry such as absence of cross strips and poor distributed GCPs (Blázquez and Colomina [2012b]; Li et al. [1993]; Rehak and Skaloud [2016]; Skaloud et al. [2014]). However, relative aerial control sacrifices absolute information and reintroduces the need of ground control. Cucci et al. [2017] proposed a dynamic network which permits a tightly coupled integration of image, inertial and GNSS observations and outperforms the conventional approach for difficult mapping scenarios such as corridor mapping or GNSS outages. The use of velocity measurements in addition to position and attitude measurements allows the estimation of GNSS/INS-to-camera synchronization parameters (Blázquez and Colomina [2012a]) while it can also be estimated as an additional parameter in BBA procedure (Rehak and Skaloud [2017]).

3.3.3 Bundle block adjustment (BBA)

The bundle block adjustment is a refinement problem to produce jointly optimal interior and exterior parameter estimates (Triggs et al. [1999]). Its name is based on the fact that the rays from the projection center to the photo points form a bundle of rays. The basic observations using in BBA are the image 2D coordinates, other additional observations such as GNSS-positions of the projection centers , 3D coordinates of ground control points allow to improve the estimation results.

Triggs et al. [1999] gives a survey of the theory and methods of BBA. The topics include : the choice of cost function, the gauge freedom and the inner constraints. Lourakis and Argyros [2004] presents detailed explanations on the standardized BBA procedures. The Levenberg-Marquardt (LM) algorithm has been the most popular

choice for BBA (Levenberg [1944]). This method is yet questioned in Lourakis and Argyros [2005] and the dog leg (DL) algorithm is proposed. The DL algorithm employs a trust region which reflects the fitness of the approximated linear model by checking if the cost decreases. In Ni et al. [2007], an out-of-core BBA which follows a divide-and-conquer approach is proposed. When given a good graph cut and initialization, a large-scale system can be reconstructed by caching submap linearizations for the full separator system.

There have been several attempts during the last few years to solve the linear system more efficiently in BBA. The key to these attempts is to replace the Cholesky factorization in LM algorithm with preconditioned conjugate gradients (PCG). Byröd and Åström [2009] applies a structural layout of variables for the better preconditioning of conjugate gradients (CG) such that the CG steps affect more directly an explicit change in the parameters. Agarwal et al. [2011] proposes the adaptive use of a sparse direct method for Cholesky factorization and a block diagonal PCG.

3.4 Corridor mapping

Corridor mapping is one of the fields with substantial importance for UAV photogrammetry. It is largely used in the surveillance and management of linear infrastructure assets – highways, railways, waterways and pipelines (Hauet et al. [2009]; Zhang et al. [2008]).

Indeed, the corridor mapping is a configuration in which continuously overlapping images are taken in series. Unlike block configuration, it constitutes only few parallel strips, cross strips are ofter absent. These characters make it an unfavorable configuration. Moreover, the lack of difference in altitude introduces a strong correlation among the altitude of camera, the focal length of the camera and the lever-arm vector from camera perspective center to the GNSS antenna phase center. To tackle the problem of the poor geometry, one can either establish a well distributed GCP network with sufficient number of GCPs or perform a block-structure flying path (Rehak and Skaloud [2015]). Both ways are time consuming and require intense field labor work. The `CNR` expects to achieve a centimeter-level accuracy while minimizing the field labor work, more generally, the number of GCPs.

When including GNSS measurements as additional measurements, the requirement of GCPs can be eliminated if a geometrically stable block of tie-points is available (Heipke et al. [2001, 2002b]; Jacobsen [2004]). However, in the case of weak geometry, typically in a single strip, the elimination of GCP network degrades significantly the precision of attitude determination (Colomina [1999]). With complete and accurate aerial control of position and attitude, the problem can be overcome in most situations (Mostafa [2002]; Skaloud et al. [1996]; Skaloud and Schwarz [2000]). Nevertheless, the limited payload, power and volumn of UAVs makes it challenging to have accurate aerial control of position and attitude. With a tightly coupled integration of image, inertial and GNSS measurements, the results achieved in a corridor configuration with only accurate position aerial control are comparable with the ones obtained in a block configuration with accurate position and attitude aerial control (Cucci et al. [2017]).

3.5 Hardware

3.5.1 Off-the-shelf UAV platforms

A large number of off-the-shelf UAV platforms dedicated to aerial photogrammetric acquisition are available in this competitive and ever-changing market. New technologies are integrated, particularly in the areas of tracking and recognition of subjects and at the level of detection and avoidance of obstacles. The trend of off-the-shelf UAV solutions is resolutely to portability and miniaturization.

In Figure. 3.3, six popular off-the-shelf UAV platforms are presented, see Table. 3.3 for specifications.

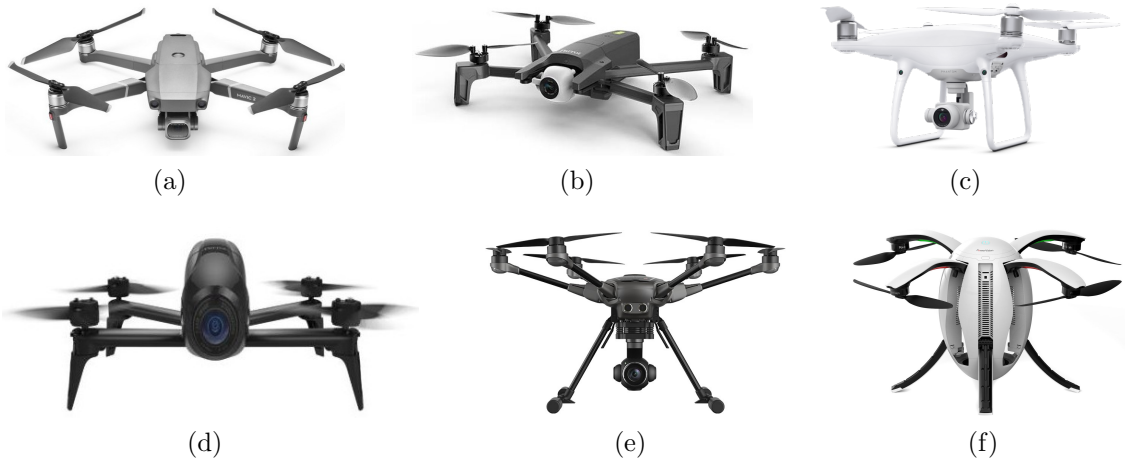

(a) (b) (c)

(d) (e) (f)

Figure. 3.3 – Popular Off-the-Shelf UAV platforms. (a) DJI Mavic 2 Pro, (b) Parrot Anafi, (c) DJI Phantom 4 RTK, (d) Parrot Bebop 2 Power, (e) Yuneec Typhoon H Plus and (f) PowerVision PowerEgg.

	Mass (g)	Autonomy (min)	GNSS	Sensor	Image Size	Lens (mm)	Shutter	Price (€)
DJI Mavic 2 Pro	907	31	GPS+GLONASS	1″ CMOS	20MP	28	Rolling	1499
Parrot Anafi	320	25	GPS+GLONASS	1/2.4″ CMOS	21MP	23-69	Rolling	699
DJI Phantom 4 RTK	1391	30	GPS+GLONASS+Galileo	1″ CMOS	20MP	8.8/24	Global	5700
Parrot Bebop 2 Power	525	30	GPS+GLONASS	1/2.3″ CMOS	14MP	wide-angle	Rolling	569
Yuneec Typhoon H Plus	2100	28	GPS	1″ CMOS	20MP	23	Rolling	1500
PowerVision PowerEgg	2100	23	GPS+BeiDou	1/2.3″ CMOS	14MP	15	not sure	745

Table. 3.3 – Specifications of popular UAV platforms in the market.

3.5.2 IGN lightweight metric camera

Consumer grade or professional cameras available on the market and adopted for metrological applications are not strictly metric. To improve the camera mechanical stability, aperture and focus locking screws are often applied (Pauly et al. [2017]). Alternatively, companies provide cameras that are optimized for UAV acquisitions (Francois and Yannick [2017]). Sometimes, research institutions like DLR (Kraft et al. [2017]) or IGN (Martin et al. [2014]) manufacture their own camera systems that are able to meet

the weight constraints imposed by UAV platforms and the satisfying stability a metric camera demands (Kraft et al. [2016]).

CamLight, the IGN's metric camera used within this research work, is presented in Figure. 3.4. The camera has been employed in several research applications, e.g. for linear aerial photogrammetric acquisition in the context of DEM restitution of dikes (Zhou et al. [2018]) ; for metrology with an integrated single-frequency GPS receiver (Daakir et al. [2017]) ; for online on-chip processing of motion blur caused by erratic UAV movements (Audi et al. [2017]).

Figure. 3.4 – CamLight, the light metric camera for UAV applications developed at IGN.

The camera employs a global shutter to avoid the shearing effect ; the sensor chip is a monochromatic 20M pixels (5120×3840) CMOSIS CMV20000 that records at up to 30 images per second (CMOSIS [2015]). Thanks to the integrated GPS chip, a synchronous GPS/image registration of high-precision is possible. See Table. 3.4 for the summary of camera characteristics.

Mass	160g
Sensor	full frame CMOS
Shutter	electronic global sensor
Image Size	20 MP
Lens	fixed, Leica 35 mm

Table. 3.4 – Specification of CamLight.

3.5.3 IGN GeoCube

The GNSS module employed in our research is GeoCube, a multi-sensor geo-monitoring system developed in team LOEMI of IGN. It was firstly designed for long-period deformation monitoring applications in static scenarios (Benoit et al. [2015]). In the framework of this research, the GeoCube is integrated in the lightweight metric camera and works in kinematic scenarios. The current version works with GPS chip u-blox NEO M8T and receives GPS signals on L1 band. The post-processing in relative mode with respect to a reference station gives highly accurate position information of the camera at exposure thanks to a good synchronization between GNSS and camera module.

Figure. 3.5 – IGN GeoCube

3.6 Software

3.6.1 MicMac

In the framework of the thesis, photogrammetric data processing and implementation of proposed methods are carried out with `MicMac`, a free open-source photogrammetric solution.

`MicMac` has been developed since 2003 at `IGN` with an initial purpose of serving for its cartographic production. In 2005, independent tools were interfaced via an XML framework, which gave the users the possibility to parameterize freely calculations at all stages. In 2007, the `IGN` started to distribute freely `MicMac` under the `CECILL-B` license, a free software license adapted to both international and French legal matters, in the spirit of and retaining compatibility with the `GNU General Public License` (`GNU GPL`). In 2008, the `Apero` tool saw the light of day, offering from then on the possibility to estimate the camera interior and exterior orientations. In 2010, the XML interface was replaced by command lines, which led to a great improvement on the accessibility, the diffusion as well as the visibility of the software. Thanks to the involvement in multiple french and european project, `MicMac` has yet been undergoing significant evolutions since 2010.

The major advantage of `MicMac` with respect to its alternatives is its high flexibility of use (cf. Figure. 3.6). An inexperienced user can carry out the processing with simple command lines with parameters set to default values. An experienced user can operate with the same command lines and adapt parameters to its need. An expert in photogrammetry can access any parameters at all stages via XML files. In addition to all that, developers and scientists can use `MicMac` as a library and implement their own algorithms.

Main algorithms used in `MicMac` are :

- `SIFT` : detection and description for points of interest
- `ANN` : matching for points of interest
- `BBA` : estimation of interior and exterior orientation

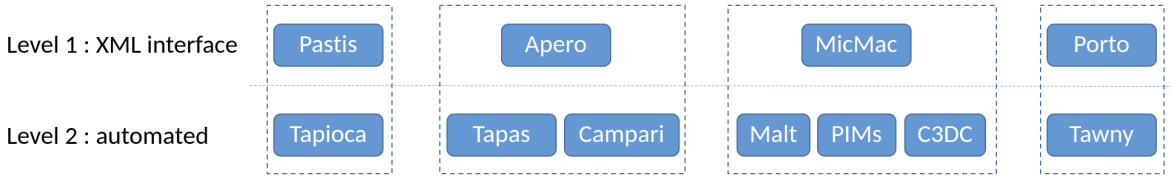

Figure. 3.6 – The low-level and high-level core modules dependencies of `MicMac`. Source : Rupnik et al. [2017].

- `SGM` : depth reconstruction

As the heart of the processing pipeline, the bundle block adjustment (BBA) is carried out with the bootstrap solution (i.e. structure from motion). Performing direct algorithm on a single image, a pair or a triplet of images, the global orientation is deduced sequentially starting from a seed image pair. The camera calibration can be performed either during the BBA procedure with the self-calibration strategy, or given as *a priori* information with the pre-calibration strategy. The BBA procedure can take tie points, GNSS-derived camera positions, GCP coordinates, image measurements and relative orientation between cameras as observation.

Aforementioned observations being redundant, the cost function is minimized with least square smethod. Three strategies are implied here to determine the observation weighting. The first strategy weights observations by their true standard deviation known a priori (similar to Gauss–Markov model). The second strategy controls observation weights of each category, which avoids over-weighting one single category only due to its abundance (e.g., tie point observations are abundant compared to GCP observations). The third strategy handles robustness ; a higher weight is given to observations having small residuals during BBA procedure. The minimization problem is solved with Levenberg–Marquardt (L-M) method. The L-M is in essence the Gauss–Newton method enriched with a damping factor to handle rank-deficient Jacobian matrices (Wright and Nocedal [1999]).

3.6.2 RTKLib

The GNSS data post-processing within the research work is carried out with `RTKLib`, an open-source program package for standard and precise positioning with GNSS (Takasu [2013]). It has been developed by *Takasu Tomoji* at `Tokyo University of Marine Science and Technology` since 2006, the original intention was to develop an application platform for precise positioning system (Takasu and Yasuda [2009]). At an initial stage, it only contained simple functions for carrier-based relative positioning and `RINEX` file handling for post processing. Nowadays, it has become a portable program library which also offers several APs (application programs) utilizing the library. In 2009, `RTKLib` was distributed as an open source program package under the `BSD 2` clause license. Table. 3.5 gives the GUI and CUI APs included in `RTKLib`.

`RTKLib` supports standard and precise positioning algorithms with most GNSS systems available nowadays : `GPS`, `GLONASS`, `Galileo`, `QZSS`, `BeiDou` and `SBAS`. Various positioning modes for both real-time and post-processing are supported : `single`, `DGPS/DGNSS`, `Kinematic`, `Static`, etc. It can deal with single frequency, double fre-

Function	GUI	CUI
AP Laucher	RTKLAUNCH	-
Real-Time Positioning	RTKNAVI	RTKRCV
Communication Server	STRSVR	STR2STR
Post-Processing Analysis	RTKPOST	RNX2RTKP
RINEX Converter	RTKCONV	CONVBIN
Plot Solutions and Observation Data	RTKPLOT	-
Downloader for GNSS Products and Data	RTKGET	-
NTRIP Browser	SRCTBLBROWS	-

Table. 3.5 – GUI and CUI APs in `RTKLib`

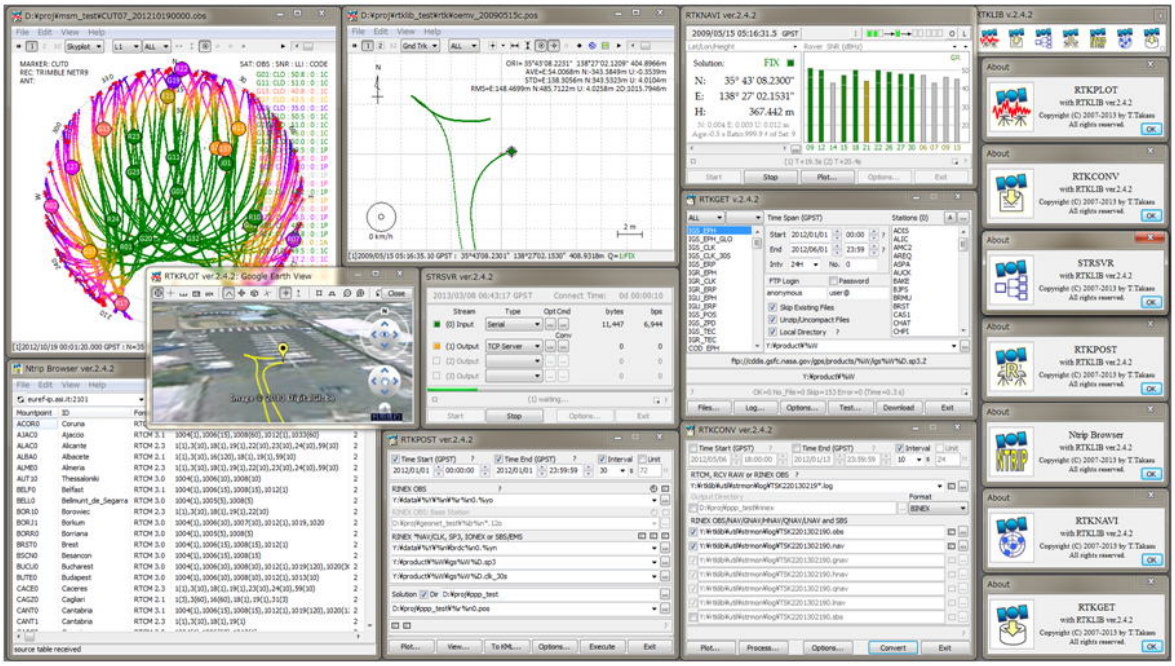

Figure. 3.7 – Some GUI APs in `RTKLib`. Source : Takasu [2013].

quency and triple frequency receivers and offers common GNSS data processing tools such as `PRN` filters, `SNR` filter on carrier-phase measurements, and atmospheric corrections. Different strategies are available for the determination of Interger Ambiguity Resolution : `continuous`, `instantaneous` and `fix-and-hold`. One that is particularly effective is the `fix-and-hold` strategy. It takes the concept of feeding information derived from the current epoch forward to subsequent epochs one step farther. An Kalman filter update is done using pseudo-measurements derived from the fixed solution, this is only done when the fixed solution is valid. The Kalman filter can be parameterized to meet the receiver specifications, especially for low-cost GNSS receivers.

Chapter 4

Simulation and analysis

Contents

This chapter corresponds to the following publications :

- Zhou, Y., Rupnik, E., Meynard, C., Thom, C., Pierrot-Deseilligny, M. (2019). Simulation and Analysis of Photogrammetric UAV Image Blocks : Influence of Camera Calibration Error. *ISPRS Annals of Photogrammetry, Remote Sensing and Spatial Information Sciences*, 195-200.
- **Zhou, Y.**, Rupnik, E., Meynard, C., Thom, C., Pierrot-Deseilligny, M (2020). Simulation and Analysis of Photogrammetric UAV Image Blocks : Influence of Camera Calibration Error. *Remote Sensing, 12*(1), 22.

The first publication is presented at the conference *ISPRS Geospatial Week 2019*, workshop *UAV-g*. The second publication is an extension version of the conference paper, and is submitted to the journal *Remote Sensing*.

In this chapiter, we tackle several issues that interest us with simulations in the first place. From a real aerial image block representing a flat, corridor configuration scene, a synthetic, error-free dataset is generated. This dataset gives us the possibility to investigate one problem at a time, without the perturbation coming from other sources. The analysis of the conducted simulations provide a first insight of the problems to be tackled. The study interest is then specified into three major problems which will be investigated thoroughly in the next three chapters.

4.1 Introduction

The derivation of geospatial information from unmanned aerial vehicles (UAV) is becoming increasingly ubiquitous (Nex and Remondino [2014]). By applying proper processing, the image pose can be derived from aerial images with high accuracy. The bundle block adjustment is a basic tool for photogrammetric pose estimation. In essence, the procedure consists of identifying common feature points between overlapping images and recovering their poses (i.e. positions and orientations) at first in a relative coordinate system, followed by the georeferencing phase with the help of, e.g. ground control points (GCP), or the camera positions measured with global navigation satellite system (GNSS) (Cramer et al. [2000]; Heipke et al. [2002a]). Camera calibration parameters can be considered pre-calibrated and constant, or their values can be re-estimated in the self-calibrating bundle block adjustement (Fonstad et al. [2013]; Westoby et al. [2012]).

In corridor mapping, the deformation caused by the accumulation of camera calibration errors often appears ; this phenomenon is called *doming effect* or *bowl effect*(James and Robson [2014]). Hence, precautions should be taken to determining properly interior orientation parameters and camera modeling. If the area of interest is largely flat, the estimation of the focal length may be inaccurate due to its high correlation with camera height. Cross flight patterns, different flight heights and the addition of oblique images may render the estimation more reliable (Zhou et al. [2018]). Nonetheless, in a corridor scene, the flight configuration is limited and cross flight patterns are not easy to achieve.

In this chapter, we are interested in investigating the impact of different camera calibration problems on the final accuracy. To avoid the potential perturbation introduced by other errors than that of interest, we generate a synthetic, error-free aerial image block which is of flat, corridor configuration. The addressed problem is then simulated and added to the dataset. The impacts of each camera calibration problem and photogrammetric accuracy are investigated.

4.2 Data generation and research design

4.2.1 Generation of a synthetic dataset

A real aerial image block is employed for the generation of a synthetic, error-free image block. In this way, a realistic tie point multiplicity and distribution as well as image overlapping are ensured. The acquisition field consists of a north-south oriented dike of 200 m, which presents a flat, corridor configuration. A total of three flights are performed : one single-height nadir-looking flight of 3 strips at 50 m (*50vt*), one nadir-looking flight of 2 strip with one strip at 30 m and the other at 70 m (*3070vt*), and one single-height oblique-looking flight of 3 strips at 50 m (*50ob*). See Figure 4.1 and Table 4.1 for more details on conducted flights. We are interested in these flight configurations since, the single-height nadir-looking flight (*50vt*) is often the routine flight configuration whereas it is not always favourable. The single-height oblique-looking flight (*50ob*) is on the contrary interesting, but not always easy to conduct. The multi-height nadir-looking flight (*3070vt*) is a possible alternative to *50ob* since it introduces different flight heights and eases the correlation between parameters on the vertical axe (Zhou et al. [2018]).

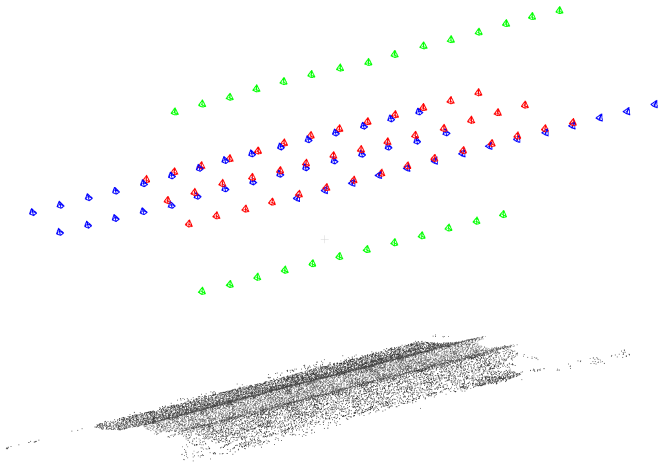

Figure. 4.1 – Illustration of conducted flights : nadir flight of 3 strips at 50 m (in red), oblique flight of 3 strips at 50 m (in blue) and nadir flights of 2 strip at 30/70 m (in green).

The original camera poses and camera calibration (camera distortion model : *Fraser* Fraser [1997]) are considered as ground truth and the synthetic dataset is generated basing on it. A set of 3D points is obtained by performing pseudo-intersection with original tie points. Afterwards, this set of 3D points is reprojected in all images for the generation of synthetic tie points. Note that the tie points generated this way intersect perfectly. A subset of these 3D points also serve as GCPs/CPs, their corresponding reprojections on images will serve as image measurements of GCPs/CPs. Figure 4.2 depicts how synthetic dataset is generated.

The synthetic dataset consists of synthetic tie points, synthetic GCPs/CPs and their image measurements, original camera calibration and original camera poses. For the synthetic dataset, the RMS of its reprojection error on images equals to 38.4 nm/0.006

Flight		***50vt***	***3070vt***	***50ob***
Nb of images		42	27	44
Height (m)		50	30, 70	50
Orientation		nadir	nadir	oblique
Nb of strips		3	2	3
Overlap	forward		80	
(%)	side		70	
GCP accuracy	horizontal		1.3	
(mm)	vertical		1	
camera focal length (mm)			35	
GSD (mm)		10	6, 14	10

Table. 4.1 – Details on the conducted flights.

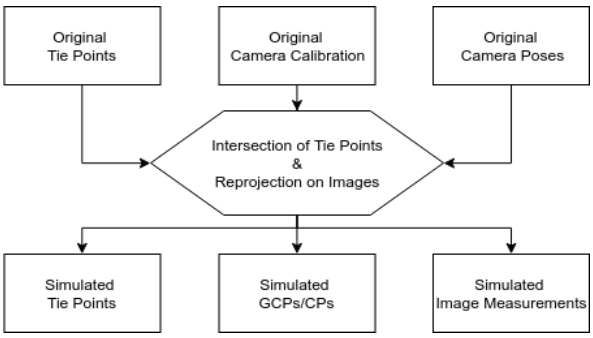

Figure. 4.2 – Workflow of synthetic dataset generation.

pixels, the RMS of its residuals on CPs is 3.1 nm, these two indicate a good consistency among tie points, camera poses, camera calibration and GCPs/CPs. It also indicates the highest accuracy one can obtain with this synthetic dataset.

4.2.2 Problem simulation and result evaluation

According to the research purposes, different camera calibration problems are simulated and added on the synthetic dataset. The photogrammetric processing is performed with a free, open-source photogrammetric software *MicMac* (Rupnik et al. [2017]).

A bundle block adjustment is carried out with tie points as observations ; camera calibration and camera poses are given as initial solutions. Depending on the investigation purpose, camera calibration parameters are either fixed or re-estimated during the bundle block adjustment. Specifications will be given for each case. Once bundle block adjustment is done, ten well-distributed GCPs are employed for the determination of a 3D spatial similarity and the camera poses are transformed into an absolute frame. The accuracy of the 3D scene will be evaluated on the RMS of residuals on five thousand well-distributed CPs.

4.3 Experiments and results

In this section, we present three issues of camera calibration, conducted experiments and corresponding results.

4.3.1 Erroneous focal length

The first issue is an erroneous focal length in the case of camera pre-calibration. To investigate how camera poses and 3D accuracy are impacted by the error on focal length, an error which varies from -50 pixels to +50 pixels with a step of 10 pixels is added on the original focal length (original value : 5510 pixels). During the bundle block adjustment, the focal length is fixed while other camera calibration parameters are freed and re-estimated. Two cases have been investigated : in the first case, images of all flights are introduced to the bundle block adjustment ; in the second case, only nadir images of three different heights are introduced (*50vt,3070vt*). Figure 4.3 depicts the variation of residuals on CPs and of camera average height for both cases.

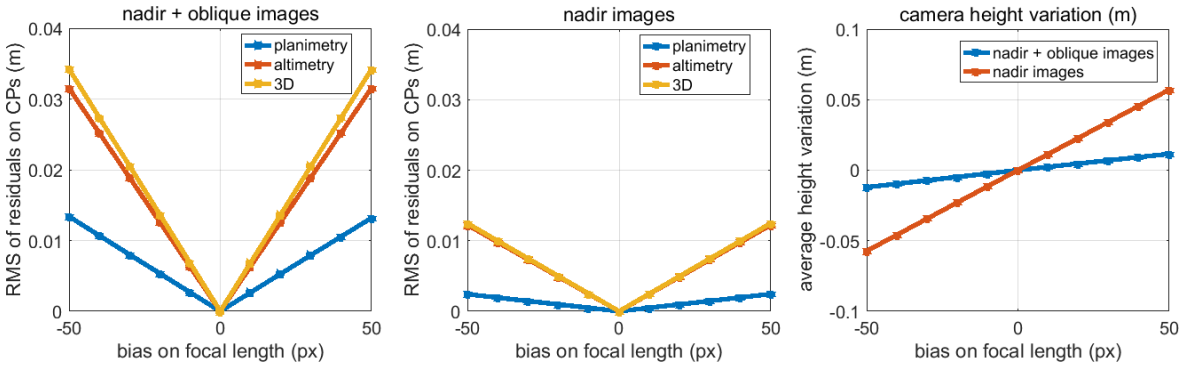

Figure. 4.3 – Variation of residuals on CPs and camera height with error on the focal length. **Left** : variation of residuals on CPs with error on focal length when all images are introduced to bundle block adjustment. **Middle** : variation of residuals on CPs with error on focal length when only nadir images are introduced to bundle block adjustment. **Right** : variation of average camera height with error on focal length.

One can see that in both cases, the residuals increase linearly with the error on focal length. The sign of the error does not affect the amplitude of residual RMS. For the case with only nadir images, the RMS is much smaller than in the other case. Secondly, the change of average camera height also changes linearly with the applied error ; when only nadir images are involved, the change of average camera height is greater. It can be explained by the fact that, during the bundle block adjustment the RMS is minimized by drifting the height of the camera, accuracy on camera poses degrades for the trade-off of higher 3D accuracy. The presence of oblique images adds constraints on camera heights therefore the obtained camera poses are closer to theoretical values whereas the 3D accuracy is compromised.

4.3.2 Gradually varied focal length

In this part, another possibility of false focal length is simulated : the camera focal length varies gradually during the acquisition whereas this variation is not taken into account during the processing. The variation of focal length is often encountered when the acquisition is carried out with a high frame rate. The internal temperature of the camera can increase significantly and leads to a gradual change of the effective focal length (Daakir et al. [2019]). However, during photogrammetric processings, one often assumes that the camera calibration parameters do not vary and one camera calibration is applied to the whole dataset.

To simulate this problem, one camera calibration is calculated (all parameters are freed and re-estimated) per image with synthetic tie points and original camera poses. The focal length is modified so that it varies during the acquisition. We generate a linear focal length variation which is expressed by the equation :

$$f^{'}(n) = f + b \cdot n \tag{4.1}$$

where : n is the image index
f is the original focal length ;
b is the increment, here b equals to 0.0275 pixels ;
$f'(n)$ is the modified focal length for image n ;

It is not sure that the focal length increases linearly in real life, but this simple model of variation gives a first hint of how the variation impacts the results. The focal length of the last image (5513.48 pixels) is 3.10 pixels greater then that of the first image (5510.38 pixels), according to the relation between the focal length and the camera internal temperature given by (Daakir et al. [2019]), an increase of 3.10 pixels corresponds to a temperature increase of around 40°C for a focal length of 35 mm as in our experiments.

Tie points and GCPs/CPs image measurements are regenerated based on original camera poses and modified camera calibrations. After that, the dataset is processed with one camera calibration for all images as which is usually done in the practice. During the bundle block adjustment, no elimination is performed on tie points, all camera calibration parameters are freed and re-estimated.

To investigate the impact of the flight configuration and the flight order of which the focal length variation takes place, as well to see if there exists one flight configuration that can minimize the influence of varied focal length, different flight combinations and flight orders are exploited. Note that the temperature increment per image is set to 0.0275 pixels as in Equation 4.1, and is independent of the order of which flights are carried out. The mapping accuracy for each configuration is given in Table 4.2.

Though the residuals on CPs may seem small, its order of magnitude is coherent with what is obtained in the previous case *erroneous focal length*. A bias of 10 pixels on focal length causes residuals about 5 mm, when both nadir and oblique images are included. In the case *50vt+50ob+3070vt*, the focal length has a variation of 3.1 pixels, the estimate of the focal length differs from the real value by 1.5 pixels at most.

		focal length variation (pixel)	Order 1						Order 2						Order 3					
			50vt, 50ob, 3070vt						50ob, 50vt, 3070vt						50vt,3070vt, 50ob					
			RMS (cm)			STD (cm)			RMS (cm)			STD (cm)			RMS (cm)			STD (cm)		
			xy	z	xyz	xy	z	xyz	xy	z	xyz	xy	z	xyz	xy	z	xyz	xy	z	xyz
1 flight	50vt	1.11	0.02	1.01	1.01	0.01	0.13	0.13	/	/	/	/	/	/	/	/	/	/	/	/
	50ob	1.21	/	/	/	/	/	/	0.05	0.05	0.07	0.02	0.04	0.03	/	/	/	/	/	/
2 flights	50vt+50ob	2.36	0.02	0.09	0.09	0.01	0.04	0.04	0.01	0.01	0.02	0.01	0.01	0.01	/	/	/	/	/	/
	50vt+3070vt	1.89	/	/	/	/	/	/	/	/	/	/	/	/	0.05	1.08	1.08	0.00	0.14	0.14
3 flights	50vt+50ob+3070vt	3.10	0.02	0.11	0.11	0.00	0.06	0.06	0.01	0.03	0.04	0.00	0.03	0.02	0.03	0.17	0.17	0.01	0.05	0.05

Table. 4.2 – Mapping accuracy with different flight configurations and flight orders.

Three flight orders are investigated, for each flight order, the number of flights needed to obtain a satisfying accuracy is studied.

1 flight If survey the field with one flight, the oblique-looking flight at 50 m (*50ob*) gives better results than the nadir-looking flight (*50vt*). Similar to the case *erroneous focal length*, the presence of oblique images prevents the camera position from drifting to compensate the incoherence on focal length, thus leads to better results. When performing the single-height nadir-looking flight (*50vt*), a slight focal length variation of 1.11 pixels can cause an accuracy degradation of 1 cm.

2 flights If two flights are conducted for mapping, the best solution is to perform a nadir-looking flight (*50vt*) in addition to an oblique one (*50ob*). However, when inverting the flight order, though the addition of oblique flight improves significantly the mapping accuracy with respect one nadir flight, it is less satisfying than performing one oblique flight. It is not recommended to add nadir strips of different flight height (*3070vt*) to the flight *50vt*, since it enlarges the focal length variation, and does not limit camera position drift as oblique images.

3 flights We see that though same flights are conducted, the order of flight influences the final accuracy. The best order is to perform firstly oblique-looking flights, then nadir ones. By comparing with **2 flights** cases, the inclusion of multi-height nadir-looking flights (*3070vt*) has negative influence when the acquisition suffers from thermal effect. This said, the addition of multi-height nadir-looking flights still brings improvements on other aspects, for instance, it ease the correlation between camera focal length, camera height and lever-arm for mapping of flat scenes (Zhou et al. [2018]).

4.3.3 Error coming from rolling shutter effect

This section studies the rolling shutter effect and its impact on aerial photogrammetric accuracy. Nowadays, the majority of consumer grade cameras are equipped with rolling shutter. Unlike global shutter cameras, rolling shutter cameras acquire images line by line. In aerial photogrammetry, the UAV surveys at a high speed (e.g. 2 m/s-10 m/s), mainstream rolling shutter cameras available on the market for aerial acquisitions have a readout time varying between 30 ms and 80 ms (definition of readout time and its value for several widely-used cameras are given in (https://www.pix4d.com/blog/rolling-shutter-correction). This means the position of the camera can be changed by several centimeters during exposure, the tur-

bulence of UAV adds as well camera orientation changes. This effect is often not taken into account either in the camera calibration or in the photogrammetric processing. It is also difficult to quantify the deformation in images introduced by the effect, which reduces the possibility of having effective corrections.

To understand better how the rolling shutter effect impacts the final results and by which level, image observations are modified such that each line is acquired with a different camera pose. We assume a uniform camera motion during the exposure. The parameters employed for the generation of simulated camera motion are listed, the value and the justification are given as follows :

- T : time interval between two images, 2.5 s, conforms to real acquisition condition
- τ : readout time of rolling shutter camera, 50 ms, a middle value among widely-used rolling shutter cameras
- $\mathbf{v}_T$: camera translational velocity, $\sim$ 3 m/s, for each image i, the instantaneous velocity is calculated as the ratio between the displacement and the time interval T of image i and $i+1$, the value conforms to real acquisition condition
- $\mathbf{v}_R$: camera rotational velocity, $\mathbf{v}_R \sim \mathcal{N}(\mu, \sigma)$ with μ=0.02°/s and σ=0.016°/s, the rotational axis is generated randomly, the amplitude of rotation angle follows the Gaussian distribution, the value of parameters μ and σ comes from IMU data of previous lab acquisitions.

The simulated rolling shutter effect is added to the synthetic dataset by modifying image measurements. After that, the dataset is processed without taking into account camera motion during exposure. During the bundle block adjustment, no elimination is performed on tie points, all camera calibration parameters are freed and re-estimated. In order to simplify the analysis, the camera rotational motion and translational motion are separated. To investigate the impact of flight configuration and to see if there exist one flight configuration that can minimize the rolling shutter effect, four flight configurations are investigated : (a) *50vt*, (b) *50vt+3070vt*, (c) *50vt+50ob*, (d) all flights (cf. Figure 4.4). Figure 4.5 - 4.8 illustrate the spatial distribution of residual on CPs for each case and Table 4.3 gives statistic information.

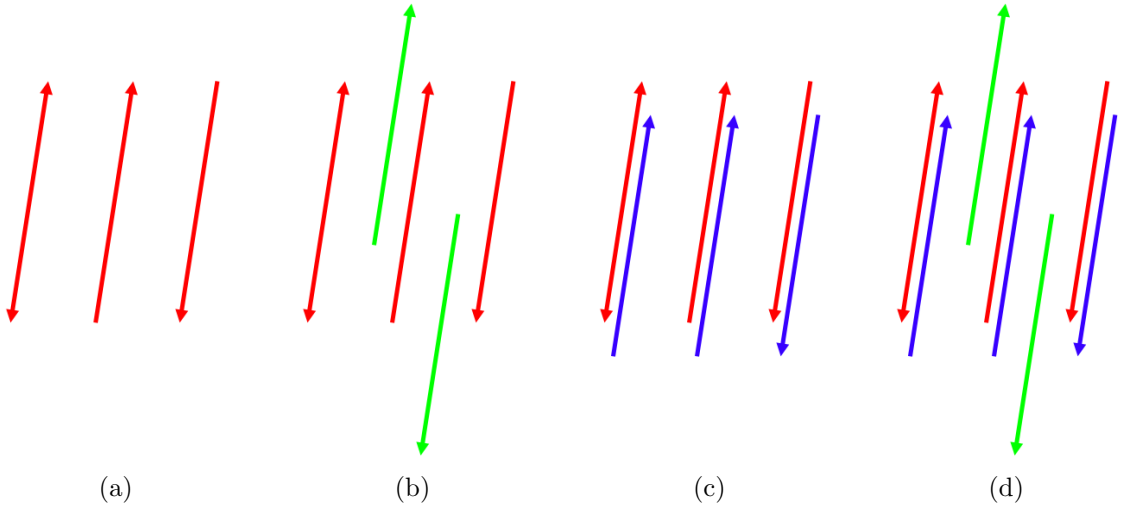

Figure. 4.4 – Four flight configurations : **(a)** *50vt* **(b)** *50vt+3070vt* **(c)** *50vt+50ob* **(d)** all flights. The arrows indicate the flight direction, the colors differentiate the flights.

	planimetry (cm)	altimetry (cm)	3D (cm)
Rotation, case **(a)**	0.07±0.03	0.19±0.19	0.20±0.12
Rotation, case **(b)**	0.02±0.01	0.09±0.08	0.09±0.05
Rotation, case **(c)**	0.03±0.01	0.01±0.01	0.03±0.01
Rotation, case **(d)**	0.02±0.01	0.01±0.01	0.03±0.01
Translation, case **(a)**	1.44±0.62	2.61±2.50	2.98±1.51
Translation, case **(b)**	18.23±7.93	5.36±5.14	19.00±7.88
Translation, case **(c)**	1.44±0.61	2.52±2.43	2.90±1.46
Translation, case **(d)**	6.88±2.97	0.71±0.77	6.93±2.97

Table. 4.3 – Statistics of the residuals on CPs, the root mean square (RMS) and the unbiased standard deviation (STD) are given.

In Figure 4.5 - 4.6, we see that the rotational motion introduces little residuals in planimetry and can be diminished with the inclusion of nadir flights of different heights and oblique images. The altimetric residuals introduced by the rotational motion is slightly higher when there is no oblique images (case **(a)** and **(b)**). Once oblique images present, the altimetric residuals decrease significantly (case **(c)** and **(d)**). The spatial distribution of residuals changes with flight configuration, we can see a minor bowl effect in all four cases, presenting in different forms.

In Figure 4.7 - 4.8, we see that inclusion of nadir images of different heights degrades largely the accuracy both in planimetry and altimetry. The inclusion of oblique images does not bring significant improvements. The spatial distribution of residuals changes with flight configuration. There is no one flight configuration that is satisfying.

It is worth noting that, the residuals introduced by camera rotational motion can be easily eliminated with the inclusion of more flight strips, such as oblique image and nadir flights of different height. Compared to the residuals introduced by camera translational motion, the one introduced by rotational motion can be considered negligible. The camera translational motion can largely decrease the accuracy of obtained results, and improvement on flight patterns can not really solve the problem. Therefore, it is essential to perform corrections when processing with rolling shutter datasets.

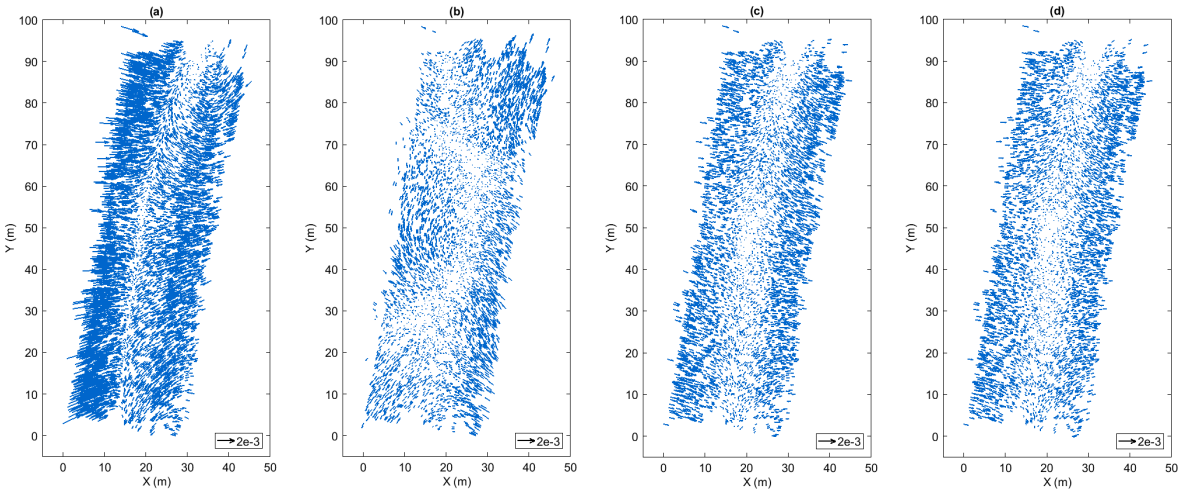

Figure. 4.5 – The spatial distribution of **planimetric** residuals when the camera **rotational** motion is added. The presented four cases correspond to the four flight configurations shown in Figure 4.4. Vector direction and magnitude represent residual direction and magnitude, respectively.

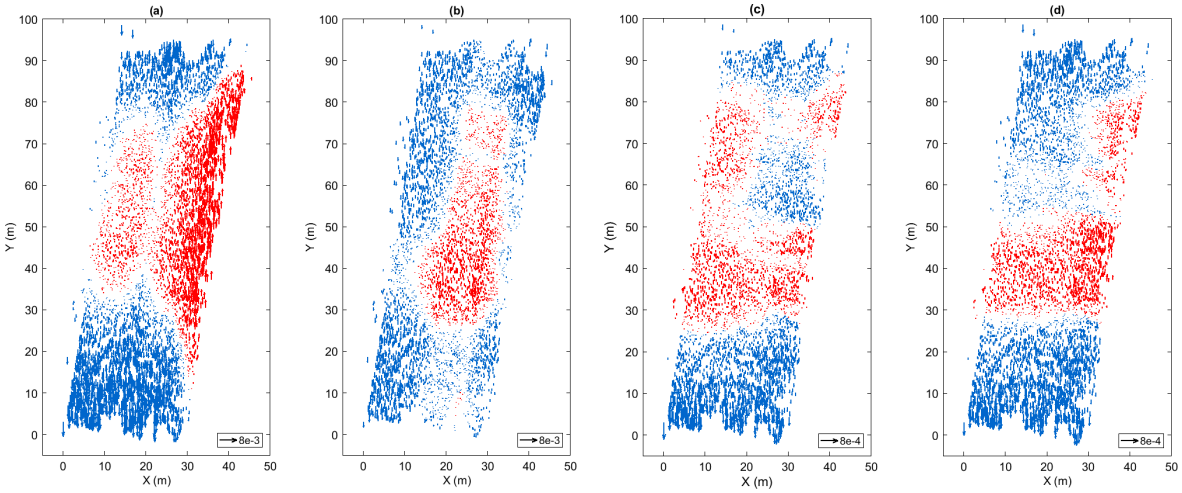

Figure. 4.6 – The spatial distribution of **altimetric** residuals when the camera **rotational** motion is added. The presented four cases correspond to the four flight configurations shown in Figure 4.4. Vector direction and color represent the sign of residuals, upward red means positive, downward blue means negative ; vector magnitude represents residual magnitude. Note that the four figures do not share the same scale.

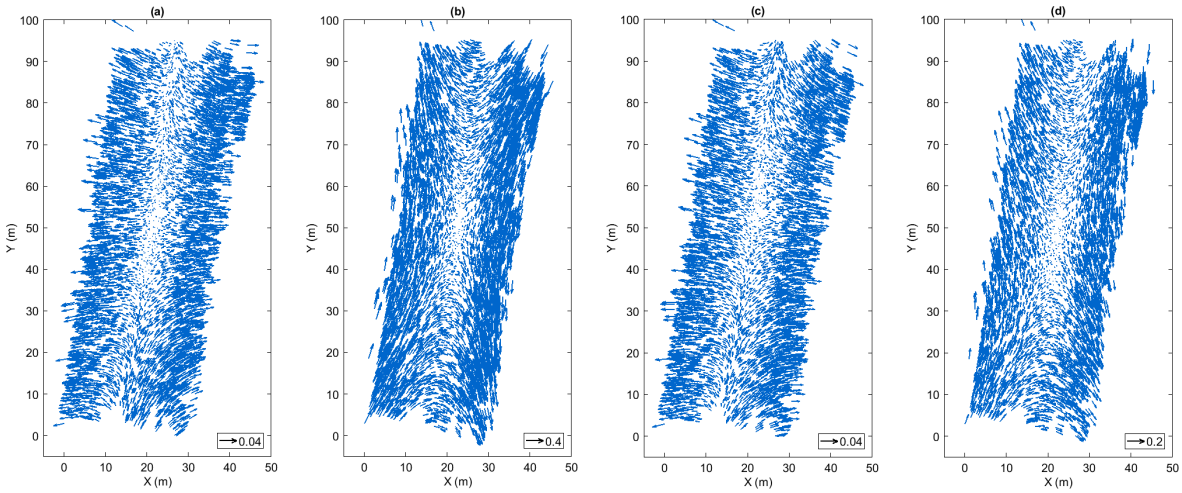

Figure. 4.7 – The spatial distribution of **planimetric** residuals when the camera **translational** motion is added. The presented four cases correspond to the four flight configurations shown in Figure 4.4. Vector direction and magnitude represent residual direction and magnitude, respectively. Note that the last figure does not share the same scale with the other ones.

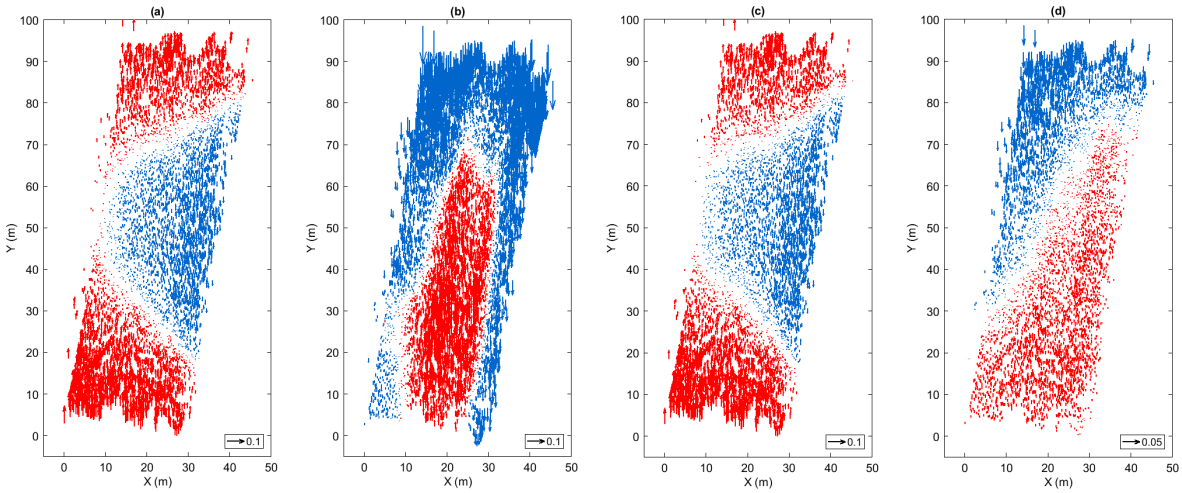

Figure. 4.8 – The spatial distribution of **altimetric** residuals when the camera **translational** motion is added. The presented four cases correspond to the four flight configurations shown in Figure 4.4. Vector direction and color represent the sign of residuals, upward red means positive, downward blue means negative ; vector magnitude represents residual magnitude. Note that the four figures do not share the same scale.

4.4 Conclusion and Discussion

This chapter studied the impact of different camera calibration issues with a synthetic aerial image block of flat, corridor configuration. The synthetic, error-free aerial image block gives the possibility to investigate the problematic of interest without the perturbation of other sources.

For a camera calibration given as initial solution, the error on focal length can be corrected during the bundle block adjustment with a good acquisition configuration. However, when an erroneous focal length is given and not re-estimated during the bundle block adjustment, camera heights drift from theoretical values to compensate for the error introduced by the erroneous focal length. The presence of oblique images limits this drift, therefore camera poses closer to theoretical values are obtained whereas the accuracy of 3D measurement is compromised.

Secondly, the focal length is likely to vary during acquisitions due to the temperature change of the camera. When this variation is not taken into consideration and one camera calibration is given for the whole dataset, an important degradation of accuracy can occur, mainly in altimetry. When only nadir images are present, a variation of 1 pixel on the focal length can decrease the 3D accuracy by 1 cm. The inclusion of oblique images brings a significant improvement, which is a good solution to the problem. It is even more recommended to perform oblique flight before nadir ones. The single-strip nadir-looking flights (*3070vt*) does not have visible improvements on the problem.

As for the degradation of rolling shutter effect, the degradation introduced by camera rotational motion can be easily eliminated with the inclusion of more flight strips. However, this improvement is negligible compared to the degradation brought by camera translational motion. There is no flight configurations that really work out, the more efficient solution should be a correction on image measurements that are impacted by the rolling shutter effect.

Chapter 5

Study of aerial acquisition geometry

Contents

This chapter corresponds to the following articles :

- Zhou, Y., Rupnik, E., Faure, P. H., Pierrot-Deseilligny, M. (2018). GNSS-assisted accurate corridor mapping with small UAV. *Congrès CFPT, 25-28 juin 2018, Paris, France.*
- Zhou, Y., Rupnik, E., Faure, P. H., Pierrot-Deseilligny, M. (2018). GNSS-assisted integrated sensor orientation with sensor pre-calibration for accurate corridor mapping. *Sensors, 18*(9), 2783.

In this chapter, the first problem of interest, the aerial acquisition geometry and its influence on corridor configuration scenes are investigated. Given the flight pattern, the number and distribution of GCPs, and the camera calibration method, the corresponding 3D accuracy one can achieve is presented. The suggestions for future acquisitions are given based on the expected accuracy and the cost.

5.1 Introduction

For traditional aerial photogrammetry with unmanned aerial vehicles (UAVs), camera poses (position and orientation) are determined indirectly using the well-known method bundle block adjustment (BBA). The BBA method is effective and widely employed for photogrammetric production when the scene is well-textured and the automated tie point extraction is possible.

The photogrammetric accuracy is strongly dependent on the acquisition geometry and the number of ground control points (GCPs) as well as their distribution within the image block (Remondino et al. [2011]; Vallet et al. [2011]). Among different configurations of UAV acquisitions, the corridor mapping is of particular interest, for instance in dike surveillance, highway planning and power line surveys (Tournadre et al. [2014]). Nevertheless, it is challenging in many aspects. The challenges come mainly from the special network geometry, and the fact that a well-distributed GCP network is not easy to ensure. The acquired images are often in strips, which makes it difficult to have satisfying cross-track overlaps and thus results in a less accurate camera pose determination. While the employment of a large number of GCPs prevents stereo model distortion (James and Robson [2014]), the field work of GCP establishment can be substantially expensive and time-consuming.

With the appearance and development of global navigation satellite system (GNSS), it is possible to know the accurate camera projection center positions at exposure and thus to reduce, or even eliminate, the requirement of GCPs within the image block (Rehak and Skaloud [2015]; Skaloud et al. [2014]). Several GCPs are still used for the purpose of improving the redundancy and identifying possible bias in GNSS positioning (Ackermann [1992]; Heipke et al. [2002b]). When coupling this GNSS-assisted bundle block adjustment approach to an inertial navigation system (INS), camera poses can be determined directly for each image without the need of traditional BBA procedure. This said, for small UAVs, an accurate position and attitude aerial control remains challenging due to the limited availability of payload, power and volume.

5.2 State of the art

Different studies have been carried out to mitigate the errors in INS/GNSS system. The linear offset lever-arm can be determined indirectly by computing the difference between GNSS-derived positions of the antenna reference point and the camera projection centers issued from bundle block adjustment (Ellum and El-Sheimy [2002]). This offset can also be estimated as an additional parameter during the bundle block

adjustment, however, the accuracy is limited due to its correlation with camera interior orientation parameters (Daakir et al. [2017]; Lichti et al. [2008]; Skaloud and Vallet [2002]). While, with classical methods (by a calliper or by photogrammetric approaches), the linear offset lever-arm can be determined, it is not possible for the boresight calibration to reach sufficient accuracy in the same way. Accordingly, several boresight calibration methods have been proposed (Cramer and Stallmann [2002]; Kruck [2001]; Mostafa [2002]; Skaloud et al. [1996]). It can be performed either with "one-step" method (i.e., estimation within the BBA process) or with "two-step" method (i.e., comparison of the INS/GNSS-derived attitude with that obtained by BBA process). Moreover, taking into account the remaining temporal correlations within the navigation system can lead to a more realistic estimation (Skaloud and Schaer [2003]). Despite the possibilities of improving the INS/GNSS system accuracy, the INS system demands more effort to reduce errors and often needs accurate GNSS positions as constraints for error control. Given the limited UAV payload capability, this demand on accuracy and thus on high quality of INS/GNSS sensors can be difficult to meet.

Therefore, for small UAV photogrammetric acquisitions, the position aerial control of GNSS systems outperforms the attitude aerial control of INS systems with its better accuracy, lower cost and lower payload requirements. The assisted bundle block adjustment with GNSS data, tie points and GCPs seems to be a more interesting approach. This approach is also referred to as Integrated Sensor Orientation (ISO). On the other hand, due to the substantial inconvenience and cost of GCP establishment, especially in areas with difficult access, the number of GCPs is to be reduced to a minimum.

In 2002, a multi-site test investigating sensor orientation is carried out by the European Organization for Experimental Photogrammetric Research (OEEPE) (Heipke et al. [2002a]) using the state-of-the-art GNSS/IMU technology of 1999. It shows that the direct sensor orientation can reach an accuracy of 5–10 cm in planimetry and 10–15 cm in altimetry, which is larger than the standard photogrammetric result by a factor of 2–3. The additional introduction of tie points into BBA procedure without GCPs improves in particular the accuracy in height and an accuracy of 5–10 cm is reached. If a minimum of GCPs is introduced, one can achieve an accuracy in object space very similar to that of conventional photogrammetry. Though with direct sensor orientation, the time and cost decrease significantly, integrated sensor orientation is preferable when very high accuracy is indispensable.

In Mian et al. [2015], an aerial acquisition of block configuration is performed on a 250 m $\times$300 m block with an embarked GNSS-inertial system integrated with a Sony a7R camera. Eight north–south strips and one cross strip are flown at 80 m, resulting in a GSD of 1 cm. With aerial control issued from the GNSS-inertial system and one GCP included in the BBA procedure, an accuracy of 3 cm is obtained in both horizontal axis and 11 cm in vertical component.

For a corridor mapping, two flight strips are flown at 135 m (Jozkow and Toth [2014]). Data of a high-grade dual-frequency GPS receiver are introduced in BBA procedure as aerial position control. With pre-calibrated camera and without GCPs, an accuracy of 12, 11 and 64 cm are reached in northing, easting and height components, respectively.

With the aid of precise aerial position control together with a pre-calibrated camera,

two case studies for accurate mapping are presented without GCPs (Rehak and Skaloud [2015]). The first one being block configuration, a self-calibration is performed within the BBA procedure without GCPs. The obtained accuracy with this configuration is 4.3 cm horizontal and 4 cm vertical. The second case study is a corridor configuration of 1200 × 180 m and the camera is pre-calibrated. Without GCPs in BBA procedure, an accuracy of 5.9, 3.3 and 7.0 cm is reached on x, y and z components, respectively.

A new approach concerning relative aerial control is proposed for integrated sensor orientation in Blázquez and Colomina [2012b]. To some extent, the procedure is simpler since the boresight matrix vanishes from the model ; moreover, high-grade dual-frequency GNSS receiver can be replaced by single-frequency and carrier-phase GNSS receiver since relative aerial control is more resistant to GNSS bias. A block configuration is carried out with relative aerial control (Skaloud et al. [2014]). With one GCP and partially biased GNSS data, the accuracy is maintained compared to without GNSS bias and is of 2.9, 2.2 and 3.8 cm on x, y and z components, respectively.

An dynamic network is proposed to tightly integrate GNSS/INS measurements into BBA procedure in Cucci et al. [2017]. For a two-flight-strip acquisition of corridor configuration with pre-calibrated boresight, lever-arm and camera intrinsics, an accuracy of 2.5, 1.5 and 1.2 cm on easting, northing and vertical components, respectively, is obtained without GCPs.

5.3 System design

5.3.1 UAV

The chosen UAV is a Copter 1B of SURVEY Copter (see Figure 5.1). It has a wingspan of 1.82 m and a length of 1.66 m. Powered by a gasoline engine, the maximal payload capacity of the UAV is 4.1 kg and the endurance is up to 60 minutes. The nominal flying altitude of the UAV is 150 m and the maximal flight speed is 10 m. The UAV possesses a radio communication with its command station. Given a pre-set flight plan registered in the command station, the flight can be performed automatically. Thus, a steady longitudinal/lateral overlap can be assured. An aluminium base mounted on the UAV was adopted for rigid camera installation and cable fixation.

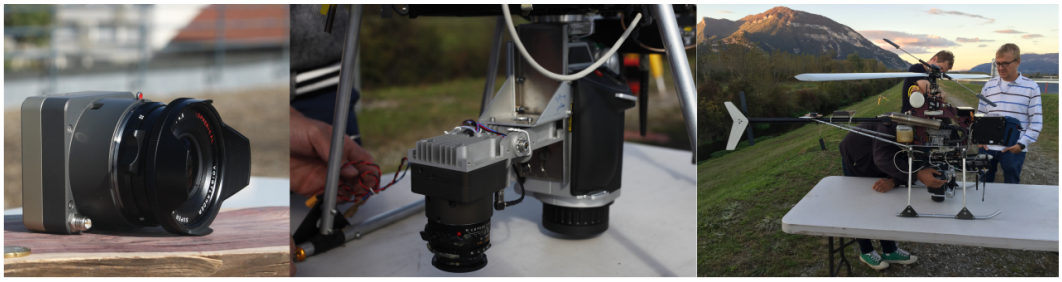

Figure. 5.1 – **Left** : CamLight **Middle** : camera set-up on UAV (**Right**) : UAV.

5.3.2 Camera

The camera chosen for data acquisition is an in-house metric camera CamLight (see Figure 5.1), designed by team Loemi (Laboratoire d'Opto-éléctronique, de Métrologie et d'Instrumentation) of laboratory LaSTIG, IGN (Institut National de l'Information Géographique et Forestière) to meet the needs of photogrammetric UAV acquisitions (Martin et al. [2014]). The compact camera body (without lens) has a low mass of 160 g and is compatible with most commercially available lenses. The camera is equipped with a full frame sensor of 5120×3840 pixels and a 35 mm lens (140 g). During acquisition, the camera is powered by the on-board power supply and is triggered with an intervalometer every 2.5 s.

5.3.3 GNSS module

The GNSS module chosen to be integrated to the camera system is a u-blox Neo M8T chip with a L1 GPS antenna. The GPS time of exposures is provided by the GPS module and is registered in the header file for each image. During the acquisition, the GPS sampling rate was set to 1 Hz.

5.4 Methodology

Figure 5.2 depicts the global data processing workflow. With the aid of *a priori* information coming from GNSS trajectories, tie points were extracted solely on overlapping images with the algorithm SIFT (Scale Invariant Feature Transform Lowe et al. [1999]). A first BBA procedure including only tie points was performed to recover the observed scene. At this step, we get information of the camera attitudes and the tie points on overlapping image couples are completed by taking this into account. A second BBA procedure including complete tie points was performed for estimating camera poses in a relative scale. GNSS-derived camera positions were used to transform the estimated relative camera poses to absolute ones by estimating a spatial similarity. Afterwards, the tie points, the GCPs, the GNSS-derived camera positions and the image measurements were used as observations for an absolute BBA. Finally, the accuracy was evaluated with CPs.

The bundle block adjustment is carried out with bootstrap solutions. Performing direct algorithm on a single image, a pair or a triplet of images, the global orientation is deduced sequentially starting from a seed image pair (Rupnik et al. [2017]). The camera is self-calibrated during the relative BBA process with a two-step procedure. Firstly, the center of distortion (CD) and the radial symmetric distortion (RSD) are estimated (the latter with a polynomial up to R^{15}). Then, the RSD and the CD parameters are fixed, and the asymmetric radial distortion is estimated. The objective of the second phase is to model the sensor and lens discrepancies that have no physical explanations. The refined camera model, especially the high degree polynomial for radial distortion correction, mitigates significantly the recurrent *bowl effect* without over-parameterizing (James and Robson [2014]; Tournadre [2015]). The estimated parameters of the camera

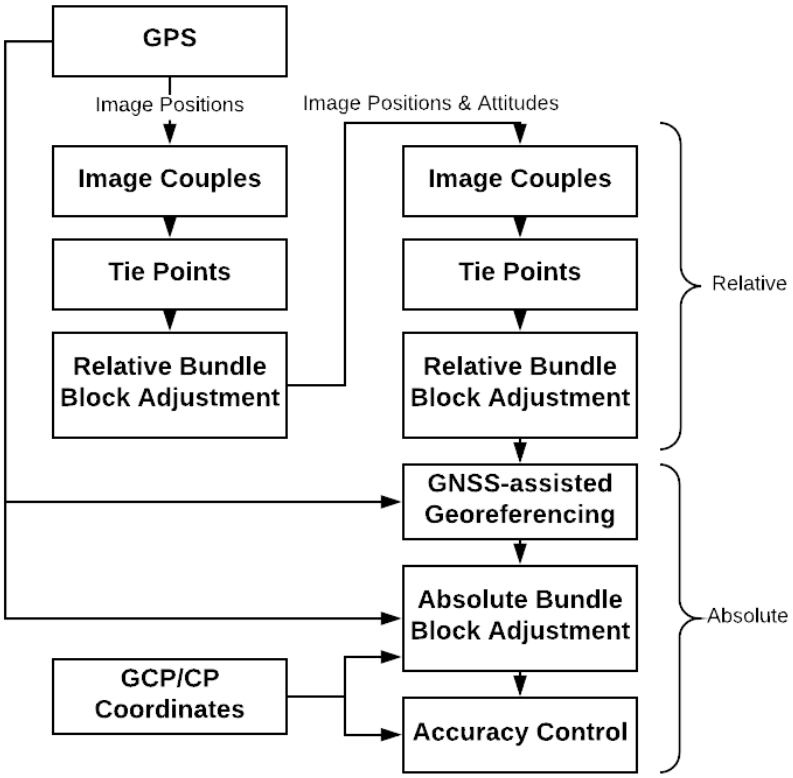

Figure. 5.2 – Data processing workflow.

model then serve as input for an absolute bundle block adjustment and can be either re-estimated or fixed within the procedure. This absolute BBA procedure takes tie points, GNSS-derived camera positions, GCP coordinates and image measurements as observations. Aforementioned observations being redundant, the cost function is minimized with least square method.

The mathematical model of the performed bundle block adjustment is presented as follows. The cost function to minimize is :

$$\mathcal{E} = \sum_{l=1}^{L}\sum_{m=1}^{M} \frac{\left(p_{l,m} - \zeta(\pi(R_m(P_l - C_m)))\right)^2}{\sigma_{im}^A} \tag{5.1}$$

$$+ \sum_{z=1}^{Z}\sum_{k=1}^{K} \frac{\left(R_k(C_k - C_{\text{gnss},k}) - \vec{\theta}_z\right)^2}{\sigma_{gnss}} \tag{5.2}$$

$$+ \sum_{n=1}^{N} \frac{\left(P_n - P_{\text{gcp},n}\right)^2}{\sigma_{gcp}} \tag{5.3}$$

$$+ \sum_{n=1}^{N}\sum_{m=1}^{M} \frac{\left(p_{n,m} - \zeta(\pi(R_m(P_{\text{gcp},n} - C_m)))\right)^2}{\sigma_{im}^H} \tag{5.4}$$

where : l is the index of tie points ;
m is the image index ;
z is the index of image blocks assorted by lever-arm ;
k is the index of images with GNSS measurements ;
n is the index of GCPs ;
ζ is the camera model ;

π is the projection function ;
$p_{l,m}$ is the 2D position of tie point l in image m ;
(R_m, C_m) is the pose of image m ;
P_l is the 3D position of tie point l ;
C_k is the camera projection center of image k ;
$C_{\text{gnss},k}$ is the phase center of GNSS antenna of image k ;
R_k is the world to camera rotation ;
$\vec{\theta}_z$ is the lever-arm of image block z ;
P_n is the pseudo-intersection position of GCP n ;
$P_{\text{gcp},n}$ is the ground measurement of GCP n ;
$p_{n,m}$ is the image measurement of GCP n in image m ;
σ_{im}^{A} is the weight of tie points in images ;
σ_{gnss} is the weight of GNSS measurements ;
σ_{gcp} is the weight of GCPs ; and
σ_{im}^{H} is the weight of image measurements of GCPs.

The global cost function is composed of four parts : (1) the cost of tie points ; (2) the cost of GNSS measurements ; (3) the cost of GCPs ; and (4) the cost of image measurements of GCPs. Three strategies are implied here to determine the observation weight. The first strategy weights observations by their true standard deviation known a priori (similar to Gauss–Markov model). The second strategy controlls observation weights of each category, which avoids overweighting one single category only due to its abundance (e.g., tie point observations are abundant compared to GCP observations). The third strategy handles robustness ; a higher weight is given to observations having small residuals during BBA procedure. The minimization problem is solved with Levenberg–Marquardt (L-M) method. The L-M is in essence the Gauss–Newton method enriched with a damping factor to handle rank-deficient Jacobian matrices (Wright and Nocedal [1999]).

Typically, a single lever-arm is estimated per image block. Here, to deal with an image block of multiple flight configurations (i.e., nadir and oblique camera-looking flights), the cost function is extended to take into account multiple lever-arms in one image block.

5.5 Data acquisition

5.5.1 Acquisition field

On 4 October 2017, several flights were conducted in Culoz, France. The surveying object of interest is a north–south orientated dike of about 1.2 km long with a turn on the north end. The scene has a corridor configuration with little height difference. Thirty-one ground points are regularly placed along the corridor and surveyed to be used either as ground control points (GCP) or check points (CP).

5.5.2 Flight design

According to the flight authorization issued by the DGAC (Direction Générale de l'Aviation Civile), the distance between the telepilot and the employed UAV could not surpass 600 m during the acquisition. Therefore, the acquisition field is divided into two segments of 600 m and surveyed separately. The first segment of 600 m consists of the south part of the dike, while the second segment consists of the rest of the dike including the turn at the north end.

The first segment is surveyed with the routine acquisition configuration, a nadir flight of 3 strips at 50 m (denoted as *s1-n50*). This configuration is simple and economic, whereas not preferable when high photogrammetric accuracy is demanded. It introduces correlations among the camera focal length, the height of the camera and the lever-arm between camera and GNSS antenna. Consequently, parameters can not be accurately estimated. The second segment consists of three flights, a nadir flight of 3 strips at 50 m (denoted as *s2-n50*), an oblique flight of 3 strips at 50 m (denoted as *s2-o50*) and a nadir flight of 2 strips with the first strip at 70 m and the second strip at 30 m (denoted as *s2-n3070*). When mixing oblique and nadir images, images acquired from different flight heights, the above-mentioned correlations can be significantly mitigated and these parameters are better estimated. This configuration of multiple acquisition angles and multiple flight heights is desirable though costly. The objective of the study is to investigate, given a good camera model and a correct lever-arm, the achievable accuracy of a simple while not preferable network configuration. The estimated camera model and lever-arm of the image block of segment 2 (*s2-n50* + *s2-o50* + *s2-n3070*) is considered of high accuracy and used for sensor pre-calibration of the image block of Segment 1 (*s1-n50*).

Figure 5.3 depicts the conducted flights, the flight information is given in Table 5.1.

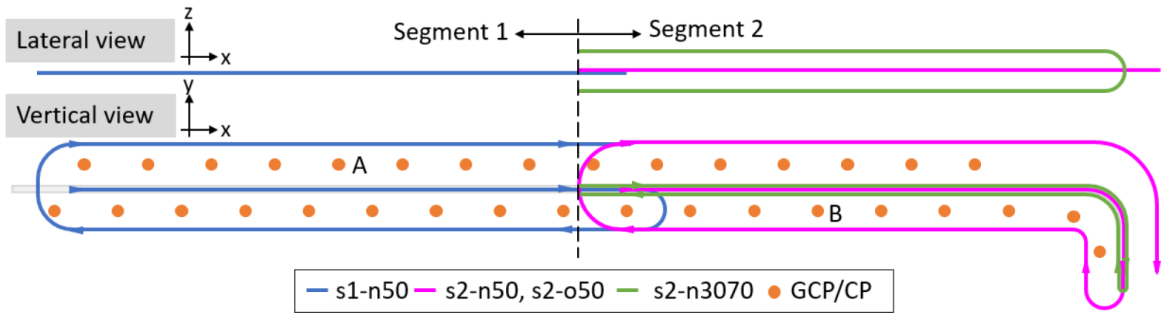

Figure. 5.3 – An illustration of the conducted flights.

Flight		***s1-n50***	***s2-n50***	***s2-n3070***	***s2-o50***
Nb of images		395	315	200	323
Height (m)		50	50	30, 70	50
Orientation		nadir	nadir	nadir	oblique
Nb of strips		3	3	2	3
Overlap	forward	80			
(%)	side	70			
GCP accuracy	horizontal	1.3			
(mm)	vertical	1			
camera focal length (mm)		35			
GSD (mm)		10	10	6, 14	10

Table. 5.1 – Details on the conducted flights.

5.6 Data processing

5.6.1 Topographic data processing

The measurements of ground points were carried out with a Leica total station. Seven stations in total were employed in *free* station mode and the measurements were performed over two days. A Leica Viva GNSS receiver was installed on the south end of the dike to give absolute georeferencing information. Its position was precisely determined by processing a ∼26 h static observation session over two days with the service provided by the IGN. The compensation of the topographic measurements was carried out with Comp3D, a geodesic micro-compensation software developed at IGN.

5.6.2 GNSS data processing

The GNSS raw data were post-processed by RTKLib open source software in the carrier-phase differential mode with respect to the Leica Viva GNSS receiver mentioned in Section 5.6.1 as base station. Table 5.2 presents the configuration of main parameters used in RTKLib for the GNSS trajectory processing. The ratio of epochs with a fixed solution to total epochs of the GNSS trajectory solution is 99.17% and the mean standard deviation along x, y and z axes amounts to 8.4, 5.5 and 9.6 mm, respectively.

Positioning Mode	Kinematic	Troposphere Correction	Saastamoinen
Frequencies	L1	Satellite Ephemeris	Broadcast
Filter type	Combined	Navigation System	GPS
Elevation Mask	15°	Integer Ambiguity Resolution	Fix and Hold
Ionosphere Correction	Broadcast	Min Ratio to Fix Ambiguity	3.0

Table. 5.2 – RTKLib parameterization of GNSS trajectory processing.

5.6.3 Synchronization of GNSS and camera modules

With a GPS sampling rate of 1 Hz, a position is calculated every second. Nevertheless, the frequency of image acquisition is 0.4 Hz, which introduces a desynchronization

between GNSS and camera system. To determine the position of the camera at exposure, a parabolic interpolation was carried out taking into account the GNSS-derived position accuracy and velocity. Figure 5.4 depicts the desynchronization between the two systems ; circles in blue represent GNSS-derived positions and pyramids represent camera frames.

Figure. 5.4 – An illustration of the desynchronization between GNSS (blue circles) and camera (pyramid) modules.

5.6.4 Photogrammetric data processing

The photogrammetric data processing is performed with MicMac, a free open-source photogrammetric software developed at IGN and ENSG (Ecole Nationale des Sciences Géographiques) since 2003 (Rupnik et al. [2017]).

To reduce memory requirements and processing time, a tie point reduction is then performed on SIFT-extracted tie points while maintaining tie point multiplicity with a stand-alone tool in MicMac (Martinez-Rubi [2016]). Figures 5.5a and 5.5b depict the distribution and multiplicity of SIFT-reduced tie points.

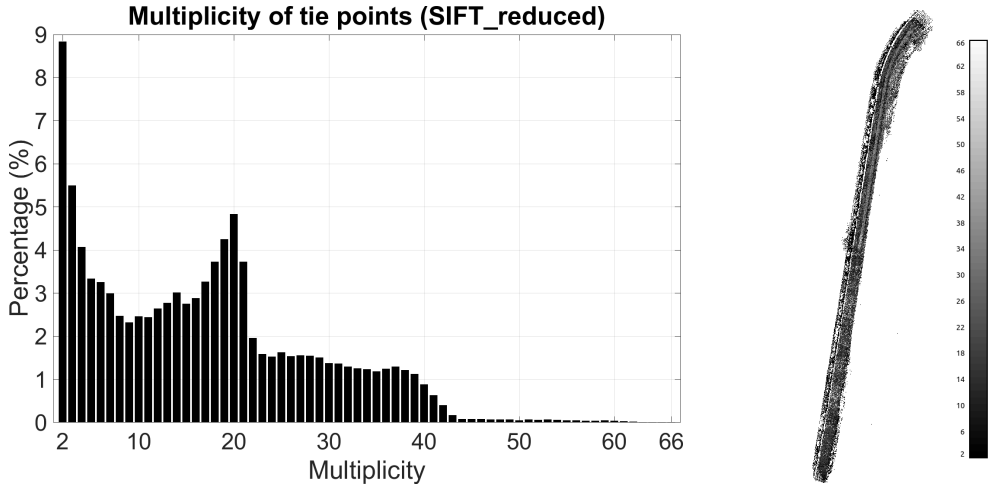

(a) (b)

Figure. 5.5 – **(a)** Multiplicity histogram of SIFT-reduced tie points. **(b)** Distribution of SIFT-reduced tie points with multiplicity represented by grey scale.

Image measurements of GCPs/CPs are performed manually. Figure 5.6 depicts the image measurement error on GCPs/CPs ordered according to their position along the south–north direction (point A : 10th, point B : 24th).

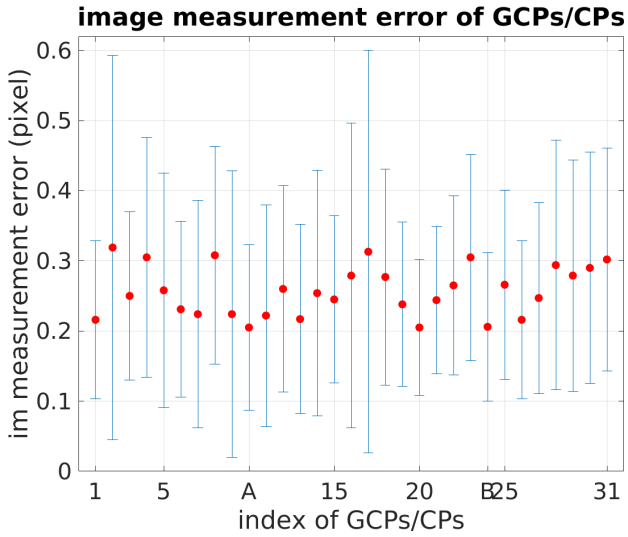

Figure. 5.6 – Image measurement error of GCPs/CPs.

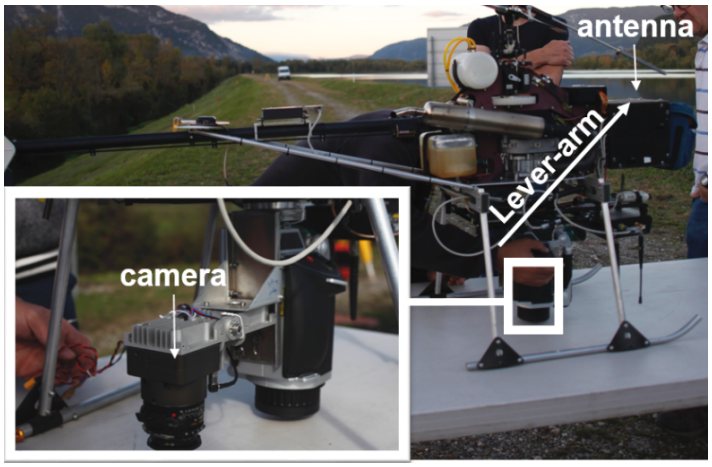

Figure. 5.7 – An illustration of the relative position between the camera and the GNSS receiver antenna.

5.7 Results

The photogrammetric data processing results are reported in Table 5.3. Flights of Segment 2 (*s2-n50*, *s2-o50*, and *s2-n3070*) were used for camera and lever-arm calibration. The camera model and lever-arm were considered unknown and were estimated during the BBA procedure. The accuracy was evaluated with CPs and the root-mean-square (RMS) of residuals on CPs was used as the accuracy criteria (the GCPs included in the BBA procedure were not used as CPs for accuracy evaluation). The camera model and lever-arm that gave better accuracy were then used as a priori information for Flight *s1-n50*. For each image block, the photogrammetric accuracy and estimation results were given in two cases : without GCP and with one GCP used in the BBA procedure. The internal photogrammetric accuracy was measured by σ, the standard deviation of all image measurement residuals for the entire block. The lower σ, the less tension within the BBA solution. Typically, a σ in the range of 4–7 mm (0.6–1 pixel) is an indication of a high quality internal block adjustment. The external photogrammetric accuracy is measured by the RMS calculated on check point 3D coordinates

(GCP used during BBA is excluded). Estimated lever-arms are given in the camera frame (the original point is the camera optical center). Figure 5.7 depicts the relative position between the GNSS receiver antenna and the camera body, which corresponds to the lever-arm vector.

Given the little elevation difference along the dike, a strong correlation exists between the camera focal length, the height of the camera and the z component of the lever-arm. The correlation coefficients of these parameters are given for each configuration.

In the following, the results are discussed in more details focusing on the influence of the adopted acquisition geometry on the final accuracy in object space.

	GCP	Parameter Liberation	σ [mm]	RMS [cm]			Lever-Arm [cm]				$\delta_{LA_z,f}$	Correlation	
				xy	z	3D		xy	z	3D		δ_{C_z,LA_z}	$\delta_{C_z,f}$
Calibration													
s2-n50 + s2-o50	0	camera model, lever-arm	5.2	1.9	8.3	8.5	na :	51.4	34.8	62.1	0.18	0.99 ± 0.00	0.18 ± 0.00
							ob :	63.2	12.7	64.5			
	1 (pt B)	camera model, lever-arm	4.9	0.9	0.6	1.1	na :	51.0	41.8	65.9	0.84	0.80 ± 0.06	0.68 ± 0.05
							ob :	66.2	18.8	68.8			
s2-n50 + s2-o50 + s2-n3070	0	camera model, lever-arm	5.0	1.9	5.9	6.2	na :	51.9	36.8	63.7	0.07	0.99 ± 0.00	0.07 ± 0.00
							ob :	64.8	14.6	66.4			
	1 (pt B)	camera model, lever-arm	4.7	0.7	0.8	1.0	na :	51.7	42.3	66.8	0.55	0.62 ± 0.09	0.33 ± 0.06
							ob :	66.5	19.4	69.3			
	14 (all)	camera model, lever-arm	4.7	/	/	/	na :	51.7	42.8	67.2	0.85	0.44 ± 0.09	0.39 ± 0.08
							ob :	66.6	19.9	69.5			
Acquisition													
s1-n50	0	camera model, lever-arm	4.8	3.3	15.0	15.3	na :	53.8	47.7	71.9	0.28	0.99 ± 0.00	0.28 ± 0.00
	1 (pt A)	camera model, lever-arm	4.8	3.3	0.9	3.4	na :	54.1	33.0	63.4	0.92	0.98 ± 0.02	0.91 ± 0.01
	0	N/A, given	5.2	3.3	2.1	3.9	na :	51.7	42.8	67.2	/	/	/
	1 (pt A)	N/A, given	5.1	3.4	2.1	4.0	na :	51.7	42.8	67.2	/	/	/

σ represents the sigma naught in bundle adjustment ; $\delta_{LA_z,f}$ represents the correlation coefficient between the nadir flight lever-arm on z-axis and the focal length ; δ_{C_z,LA_z} represents the correlation coefficient between the camera height and the nadir flight lever-arm on z-axis ; $\delta_{C_z,f}$ represents the correlation coefficient between the camera height and the focal length ; and N/A means the camera model and the lever-arm are not estimated but given as *a priori* informations

Table. 5.3 – Results of photogrammetric data processing.

5.7.1 Influence of oblique images

Two datasets are processed for camera and lever-arm calibration. The first dataset combines nadir and oblique images of Flights *s2-n50* and *s2-o50*. The inclusion of oblique images eases the correlation between the focal length and the lever-arm as well as between the focal length and the camera height ($\delta_{LA_z,f} = 0.18$ and $\delta_{C_z,f} = 0.18$). However, when no GCP is included in BBA procedure, the z component of lever-arm remains highly correlated with the camera height ($\delta_{C_z,LA_z} = 0.99$). By including one GCP (Point B, as shown in Figure 5.3), the z component of lever-arm is better decorrelated from the height of camera (correlation coefficient $\delta_{C_z,LA_z} = 0.80$). With the added information, more constraints are applied within the BBA procedure and the correlations between the focal length and other two parameters increased ($\delta_{LA_z,f} = 0.84$, $\delta_{C_z,f} = 0.68$). The internal photogrammetric accuracy is also slightly improved (σ is decreased by 0.3 µm). Moreover, the RMS of residuals on CPs decreases considerably, especially along z-axis. This gain is mainly due to the proper estimation of the z component of lever-arm. We can see that the RMS of residuals on CPs decreases by 7.6 cm on vertical direction while the estimated lever-arm vector has an increase of 7 and 6.1 cm on z axis for nadir and oblique flight, respectively.

5.7.2 Influence of multiple flight heights

In the second dataset, nadir images of different flight heights (*s2-n3070*) are added to the first dataset (*s2-n50*, *s2-o50*). Without any GCP, the addition of images of different flight heights eases the correlation of the focal length with other two parameters ($\delta_{LA_z,f} = 0.07$ and $\delta_{C_z,f} = 0.07$) while the lever-arm on z-axis is still strongly correlated to camera height ($\delta_{C_z,LA_z} = 0.99$). The RMS of 3D point residuals is improved by 2.4 cm and the lever-arm estimation of nadir image is diminished by 2 cm. With one GCP being included, the addition of images of different flight heights largely reduces the correlations among these three parameters ($\delta_{LA_z,f}$ decreases from 0.84 to 0.55, δ_{C_z,LA_z} decreases from 0.80 to 0.62, and $\delta_{C_z,f}$ decreases from 0.68 to 0.33). The internal and the external photogrammetric accuracies are further improved and the RMS of 3D point residuals is decreased to 1.0 cm. For camera model and lever-arm calibration, all GCPs of Segment 2 are included for computing an optimal BBA solution. Parameter estimates issued from this BBA procedure are then used as a priori information for the Flight *s1-n50*.

5.7.3 Basic flight configuration

For a simple, economic while not preferable flight configuration such as *s1-n50*, with neither *a priori* information on the camera model and the lever-arm, nor any GCP being included in the BBA procedure, an important residual is observed on the z component. The camera height and the lever-arm are strongly correlated ($\delta_{C_z,LA_z} = 0.99$). The inclusion of one GCP (Point A, as shown in Figure 5.3) improves to a large extent the photogrammetric accuracy, especially on the z axis. However, due to the poor geometry of the acquisition network, the correlation between the lever-arm and the height of camera remains high. Though residuals are small on z axis, the z

component of the lever-arm is far from being correct. The accuracy is less satisfying than when oblique images are also taken into account.

Given a good calibration of the camera model and the lever-arm estimated with the image block of Segment 2 (*s2-n50 + s2-o50 + s2-n3070*) with all GCPs, the photogrammetric accuracy is further improved. Without any GCPs, the RMS of 3D point residuals on CPs is equal to 3.9 cm. It is worth noting that when giving well calibrated camera and lever-arm, the results obtained with a nadir flight of 3 strips (*s1-n50* + 0 GCP) outperform that obtained with the second dataset (*s2-n50 + s2-o50 + s2-n3070* + 0 GCP). The inclusion of one GCP does not improve the external photogrammetric accuracy on z, which can be explained by the fact that the camera model and lever-arm are already well-calibrated and fixed during the BBA procedure. However, even with well-calibrated parameters, the accuracy of image block *s1-n50* does not exceed the one of the image block *s2-n50 + s2-o50 + s2-n3070* when employing one GCP. It is possibly due to the better quality (better multiplicity and distribution) of tie points extracting from the latter image block.

5.8 Discussion

Four flights were conducted on two segments of a 1.2 km long dike and about 1100 images were acquired. In this study, unlike what most commercially available photogrammetric softwares do, we performed an estimation of multiple lever-arms within the BBA procedure. It liberates us from the physical constraint between the camera and the GNSS antenna and makes it possible to merge image blocks of different configurations. For camera calibration strategy, instead of performing laboratory calibration in a close range configuration, we proposed an in-flight calibration which describes the true acquisition condition and gives more accurate camera calibration. Despite the poor geometry of the dike, our approach obtained a centimetric accuracy with one GCP and an accuracy of 3.9 cm with 0 GCP when in-flight calibration of camera and lever-arm is provided. The results outperform that of the majority of literature works.

Based on the experiments presented in the article, we suggest that the best acquisition geometry for corridor mapping is the inclusion of nadir and oblique images of different flight heights. The mapping accuracy can reach 1 cm when good GNSS data and at least one GCP are given. For the acquisitions with lower accuracy demands and limited budget, one nadir flight is sufficient for achieving an accuracy of 4 cm with a well-calibrated camera and lever-arm. Under the condition where well-calibrated camera and lever-arm are unavailable, the combination of one nadir and one oblique flight can reach an accuracy of 8–10 cm without any GCPs.

Chapter 6

Study of thermal effect

Contents

This chapter corresponds to the following publication :

- Daakir, M., Zhou, Y., Pierrot-Deseilligny, M., Thom, C., Martin, O., Rupnik, E. (2019). Improvement of photogrammetric accuracy by modeling and correcting the thermal effect on camera calibration. *ISPRS journal of photogrammetry and remote sensing, 148*, 142-155.

In this chapter, a method of improving the photogrammetric accuracy for metric cameras is proposed. It consists of correcting the image deformation introduced by camera temperature change. The thermal effect is firstly modeled, then the correction is applied on both terrestrial and aerial datasets for performance evaluation.

6.1 Introduction

Photogrammetry has undergone an unprecedented evolution in the past two decades. It benefits from the development of cameras, the even higher computing power computers, the rise of aerial photogrammetry, and the quasi-automatic data processing software. Today, photogrammetry has become a standard technique for contactless metrological applications thanks to its adaptable accuracy, which is determined by parameters such as for instance, the ground sampling distance (GSD), the image overlap, and the acquisition geometry.

A part from these, the stability of camera internal parameters is as well a crucial factor to the final accuracy. Metric cameras are often preferable for metrological applications because of its good performance on this aspect. To achieve this, high quality lens and reliable construction are employed, the number of moving parts are reduced. Nonetheless, several physical phenomena should still be paid attention to when a high measurement accuracy is requested. For example, the temperature change of a camera can impact its internal geometry and lead to variations of internal parameters. While performing an image-variant camera calibration may be a good solution, it can be numerically unstable given the large number of parameters to estimate and the strong correlation between the camera internal and external parameters (Remondino and Fraser [2006]). Another solution, which is to be presented in this chapter, is to model the variation of internal parameters introduced by the camera temperature change, and to correct the image deformation due to this thermal effect.

6.2 State of the art

Photogrammmetry has become a standard technique for contacless metrological applications and is particularly interesting in engineering applications where high measurement accuracy is requested (Kölbl [1976]; Luhmann [2010]; Rieke-Zapp and Nearing [2005]). Metric cameras are ofter favored for metrological works because of the good stability of its internal parameters.

Charge-coupled device (CCD) image sensor and complementary metal-oxide semiconductor (CMOS) image sensor are commonly used in metric cameras. For CCD sensors, the electrons can be thermally excited into the conduction band, which causes an intrinsic noise called dark current (Saks [1980]; Widenhorn et al. [2002]). This thermally activated process is strongly temperature dependent and limits the performance of CCD sensors in low light level conditions.

Therefore, CMOS image sensor has become the major player in the imaging market,

also because of its lower cost and lower power consumption. Schwartz [2010] points out that the temperature range of CMOS sensors is quite an improvement compared to that of CCD image sensors. Nonetheless, the temperature change of CMOS image sensors during image acquisitions can still introduce a thermal effect on images. Lin et al. [2010] quantifies the radiometric effect on a CMOS image sensor, fixed pattern noise is observed to increase with temperature. Sauer [2001] presents a method correcting fixed pattern noise of a CMOS image sensor which can be a result of temperature changes during standard operation.

The influence of temperature on the internal parameters of the camera is a known effect since the appearance of aerial photogrammetry. Hothmer [1958] lists various sources of errors to be considered in the context of aerial mapping. Among the sources it is mentioned that "the effect of temperature can possibly be considerable". Yastikli and Jacobsen [2005] specifies that, during flight conditions, the vertical temperature gradient causes a significant deformation of the camera lens. Investigations carried out with an aerial camera show that the effect of temperature change induces a variation of focal length of 0.5 µm/C° (0.068 pixels/C°) for a Nikor lens of 20 mm (2575 pixels) (Merchant [2006, 2012]). Merchant adds : "For a flight with a height of 2000m above ground, this (focal length variation) corresponds to a systematic elevation error of 1 m compared to a position determined by GPS". Experience with the Helimap Mapping System highlights the importance of the calibration step in the process pipeline and particularly the stability of the camera calibration (Vallet [2007]). The various datasets acquired with this system show that the focal length and the principal point are not very stable. These parameters are mainly influenced by the variation of temperature and vibrations. Over a period of one year, the observed variation in focal length is 30 µm (for a 35 mm lens, value in pixel is not reported) and 15 µm for principal point. Smith and Cope [2010] presents a study that investigates the influence of temperature on a commercial digital camera. The experiment consists of leaving the camera for several hours in a fridge to lower its internal temperature. The variation observed in the focal length is 1 µm/C° (0.13 pixels/C°) for a 28 mm lens (3590 pixels). Fiedler and Müller [2012] study the thermal effect on the Kinect sensor. By alternating and combining different states - variation of internal and external temperature, the impact on sensor measurements is proved to be considerable. The distribution of observations show that the increase in temperature can be interpreted as a zoom-in effect.

6.3 IGN lightweight metric camera

Consumer grade or professional cameras available on the market and adopted for metrological applications are not strictly metric. To improve the camera mechanical stability, aperture and focus locking screws are often applied (Pauly et al. [2017]). Alternatively, companies provide cameras that are optimized for UAV-acquisitions (Francois and Yannick [2017]). Sometimes, research institutions like DLR (Kraft et al. [2017]) or IGN (Martin et al. [2014]) manufacture their own camera systems that are able to meet the weight constraints imposed by UAV platforms and the satisfying stability a metric camera demands (Kraft et al. [2016]).

6.3.1 Generalities

CamLight, the IGN's metric camera used within this research work , is presented in Figure. 6.1. The camera has been employed in several research applications, e.g. for linear aerial photogrammetric acquisition in the context of DEM restitution of dykes (Zhou et al. [2018]) ; for metrology with an integrated single-frequency GPS receiver (Daakir et al. [2017]) ; for online on-chip processing of motion blur caused by erratic UAV movements (Audi et al. [2017]).

The camera employs a global shutter to avoid the shearing effect ; the sensor chip is a monochromatic 20M pixels (5120 × 3840) CMOSIS CMV20000 that records at up to 30 images per second (CMOSIS [2015]). Thanks to the integrated GPS chip, a synchronous GPS/image registration of high-precision is possible. See Table. 6.1 for the summary of camera characteristics.

Figure. 6.1 – CamLight, the light metric camera for UAV applications developed at IGN.

sensor	
type	CMOS
shutter	electronic global shutter
spectral range	monochromatic
format	24.5 × 32.7 mm
image format	3840 × 5120 pixels
pixel size	6.4 × 6.4 µm
lens	
focal length	fixed, Leica 35 mm (5489 pixels)

Table. 6.1 – Specification of CamLight.

6.3.2 Temperature registration

The chip CMOSIS CMV2000 incorporates a temperature sensor (CMOSIS [2013]). The temperature measurements are translated to the device temperature with the help of Equation (6.1)

$$T_r = a \cdot T_a + b \tag{6.1}$$

where : T_r = registered temperature ;
a = coefficient between registered temperature and absolute temperature ;
T_a = absolute temperature ;
b = offset

Typical values of the coefficient a and the offset b are given by the manufacturer. The registered temperature T_r is quite close to the absolute temperature T_a as we use typical calibration values offered by constructors. However, these parameters vary slightly from recorders and need to be recalibrated when the absolute temperature is required. In our research, we are only interested in the variation of the temperature but not the absolute value.

Note that the measured image sensor temperature does not fully represent the thermal state of the camera. Temperature of the external environment has equally an impact on the camera's internal parameters (Pan et al. [2015]). Within this work we do not discuss the influence of the external temperature, during the experiments we reduce the variation of the environment temperature to a minimum by, (i) for the indoor case, conduct the experiments in a space of constant temperature, and (ii) for the outdoor case, conducting it in a short period of time.

6.4 Calibration of thermal effect

In this section, we seek to calibrate with two methods the variation of camera interior orientation with temperature change. The first calibration method relies on the image correlation technique and assumes a constant exterior orientation. The second calibration method consists of space resection and bundle adjustment. Both methods infer the sensor response to the raising temperature with the variation of focal length (i.e. scale factor), the translation and the rotation of the image.

6.4.1 Thermal model

The thermal effect has an impact on the camera internal parameters and manifests in 2D displacements in image space. We model and analysis in the first place the induced displacement with a 4-parameter 2D spatial similarity transformation (cf. Eq. 6.2). The choice of the model is driven by its simplicity of physical interpretations. In practice, generic polynomials are applied to ensure a finer modeling (cf. Eq. 6.3).

$$\begin{bmatrix} i_D \\ j_D \end{bmatrix} = \begin{bmatrix} u(T) \\ v(T) \end{bmatrix} + k(T) \begin{bmatrix} cos(\theta(T)) & -sin(\theta(T)) \\ sin(\theta(T)) & cos(\theta(T)) \end{bmatrix} \times \begin{bmatrix} i_R \\ j_R \end{bmatrix} \tag{6.2}$$

where : T = temperature of the camera ;
$[i_D, j_D]^t$ = deformed image coordinates ;
$[u(T), v(T))]^t$ = vector of translation ;
$k(T)$ = scale factor ;
$\theta(T)$ = angle of rotation ;
$[i_R, j_R]^t$ = original image coordinates.

The parameters are estimated with the least squares solver. All pixels of the deformation map computed with image correlation technique (see 6.4.2) are used as observation.

We assume the thermal effect to be a deterministic function of temperature. For one image taken under a given temperature T, the deformation $\mathcal{M}_{T_0}^{T}(x, y)$ with respect to the image of reference taken under T_0 is computed. To obtain the deformation $\mathcal{M}_{T_0}^{T}(x, y)$ for all values of T, we interpolate from a set of computed deformations $(\mathcal{M}_{T_0}^{T_1}, \mathcal{M}_{T_0}^{T_2}, \cdots, \mathcal{M}_{T_0}^{T_N})$. The estimated deformation model can be expressed by Equation. (6.3).

$$\mathcal{M}_{T_0}^{T}(x, y) = \sum_{k=1}^{3} \sum_{i=1}^{4} \sum_{j=1}^{4} a_{k,i,j} T^k x^i y^j \tag{6.3}$$

All image pixels are used as observation for the coefficient determination of the said model. Therefore, there is no risk of over-parameterization even though the number of estimated parameters is high. Once the deformation function is determined, the corresponding correction is computed. Image measurements are then corrected as presented in the processing workflow (Figure. 6.2).

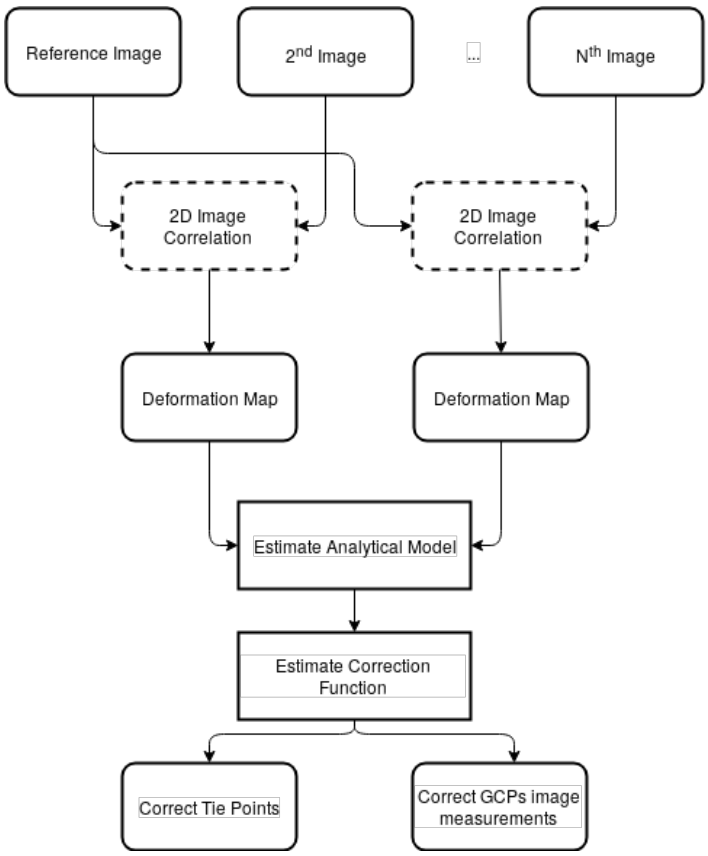

Figure. 6.2 – General workflow for thermal deformation modeling.

6.4.2 Deformation determination with 2D correlation

6.4.2.1 Parameterization

2D sub-pixel image correlation implemented in Pierrot-Deseilligny and Paparoditis [2006] is used as the deformation measurement technique. Image correlation is a well-established method for determining 2D displacement maps in the field of Earth Sciences (Rosu et al. [2015]) and in industrial applications (Maas and Hampel [2006]).

Our camera is fixed to a heavy tripod and is considered static during the experiments. Therefore, any displacement in image space corresponds to the deformation introduced by temperature variation. Among the essential correlation parameters there are : searching interval (SI), discretization step (DS), correlation threshold (CT), correlation weight (CW), number of exploited directions (DIR) and the correlation window size (CWS). The SI defines the displacement search area, the DS is the sub-pixels precision, the CT is the value below which two pixels will be regarded as not correlated, the CW is a weight that increases the significance of the better-correlating pixels within the optimization, and the DIR corresponds to the number of direction exploited in optimization phase. The parameter values should be adapted to the nature of the anticipated displacements. Here, as the thermal effect causes 2D movements of low amplitude, parameter values similar to those defined in Rosu et al. [2015] for analyzing seismic events are adequate. The reader is referred to this publication for more detailed understanding of the individual parameters as well as to Hirschmuller [2008] regarding the correlation optimization scheme. See Table. 6.2 for the list of parameters and their values.

Parameter	Value
Searching interval (px)	6
Discretization step (px)	0.2
Correlation threshold	0.5
Weight of correlation	2
Number of directions	7
Size of window (px)	20

Table. 6.2 – Selected parameters for image correlation

6.4.2.2 Experiment design

Two cameras are fixed on one heavy tripod, they observe a textured wall and perform two independent acquisitions (see Figure. 6.3). The objective is on the one hand to collect a wide range of temperature scenarios ; on the other hand, we want to verify that the deformations are repeatable for similar temperature scenarios.

We note the acquisitions with two types. Type I acquisition consists of taking image sequences from the same point of view as the camera temperature increases. Type II acquisition uses a second camera with a cooling system attached to its back. The cooling system is a Peltier solid-state active heat pump which transfers heat from one side of the device to the other (https://en.wikipedia.org/wiki/Thermoelectric_cooling).

Figure. 6.3 – The scene of the textured wall (left) and the installation of cameras and Peltier cooler (right).

Type I acquisition Three acquisitions of type I are performed. The first two are acquired successively on the same day with the temperature rounding to an integer ; the third acquisition is obtained on another day with the temperature rounding to an increment of 0.3 °C or 0.4 °C. This setting is to study the influence of temperature precision on the quality of maps and to ensure that the deformation is stable over time. The frame rate is set to approximately one image every 4 seconds to get a significant increase of the camera temperature. For each acquisition, the first image is considered as the image of reference. Deformation maps are generated by comparing each successive image with the image of reference. Figure. 6.4 shows an example of the correlation map, which can be an indicator of the matching quality between images, and an example of the deformation map.

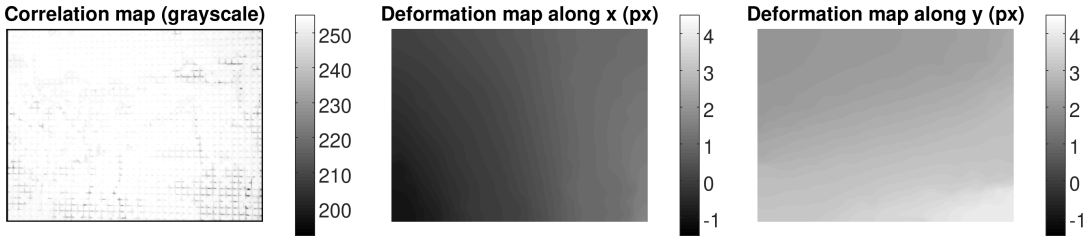

Figure. 6.4 – An example of the correlation map (left) and the 2D deformation map along x (center) and y axis (right)

Type II acquisition One acquisition of type II is performed. The acquisition frame rate is decreased to one image per minute. With the cooling effect behind, the camera temperature varies within a small range. The temperature is rounded to an increment of 0.3 °C or 0.4 °C. Here, to verify the absence of deformation when there is no change on the camera temperature, two image couples taken under the same temperature with a long time interval are considered. Table. 6.4 provides details on the investigated image couples.

Table. 6.3 presents details of the conducted acquisitions, Figure. 6.5 depicts the temperature variation for each acquisition.

	Type	Acquisition time (min)	Nb of images	Temperature range (°C)
Dataset 1	I	38	597	[24, 49]
Dataset 2	I	44	716	[25, 50]
Dataset 3	I	30	377	[24.8, 56.2]
Dataset 4	II	37	37	[22.9, 23.6]

Table. 6.3 – Information of 2D correlation datasets

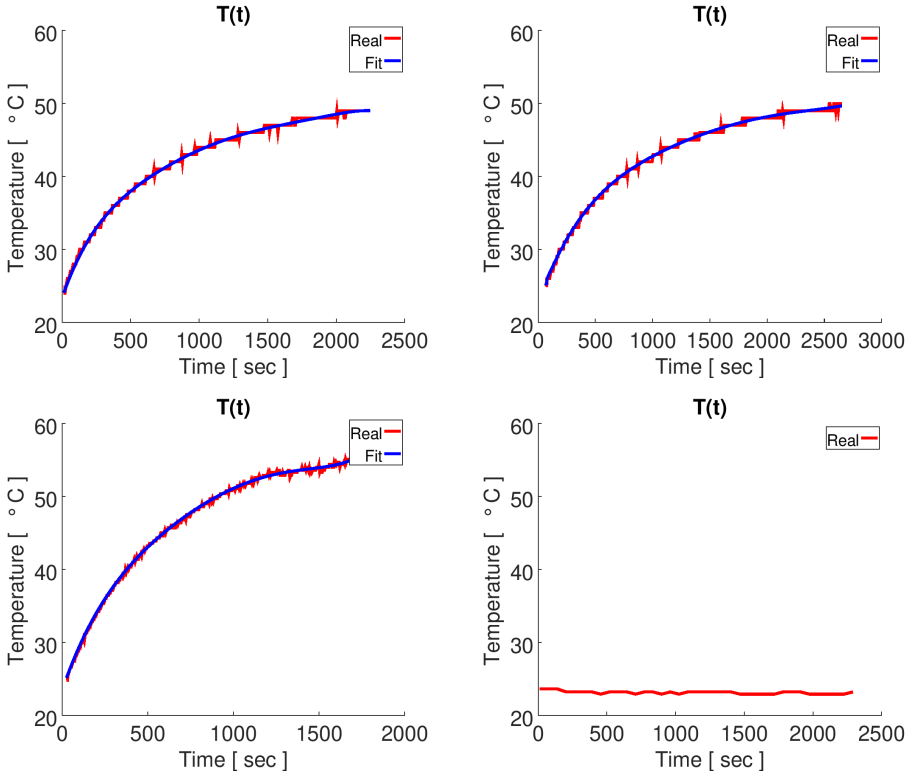

Figure. 6.5 – Temperature variation of Type I acquisition : dataset 1-3. Temperature variation of Type II acquisition : dataset 4 (lower right)

	Temperature (°C)	Time interval (min)
Couple 1	22.9	29
Couple 2	23.2	28

Table. 6.4 – The investigated image couples in Type II acquisition.

6.4.2.3 Results

Type I acquisition The 4 parameters of the 2D spatial similarity transformation that models the induced image deformations is presented in Figure. 6.6-6.8. The focal length depicted is the estimated mean scaling factor on all image pixels. All parameters increase with the temperature. The variation of the translation corresponds to the deviation of the principal point. The variation of the focal length and the rotation can be interpreted as image sensor deformation caused by component dilatation. For Dataset 1 and Dataset 2 acquired on the same day, all the 4 parameters vary in the same way and a good repeatability of the thermal effect is observed. Dataset 3, acquired

4 months later, has a similar focal length variation, whereas the variation of translation and rotation differ from Dataset 1 and 2. For all 3 datasets, the variation of rotation remains insignificant during the acquisition (less than 0.02 px/°C). The thermal effect is reproducible but not repeatable over time for all parameters. We are not yet able to explain why translation varies differently over time. To be mentioned, the slope of the focal length variation 0.4-0.5 µm/°C (0.07-0.08 px/°C) is of the same scale as the result 0.5 µm/°C (0.068 px/°C) presented in Merchant [2006, 2012].

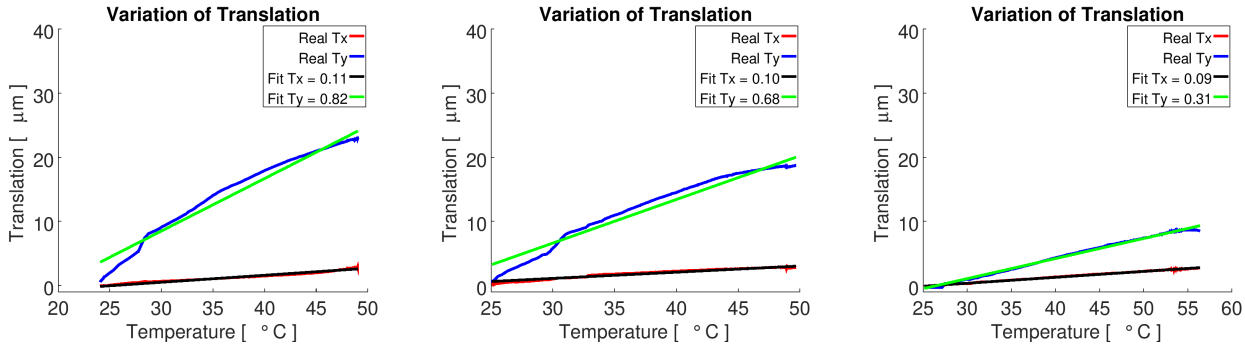

Figure. 6.6 – Estimated translation : dataset 1-3 (from left to right). T_x and T_y are the translations along respective axes.

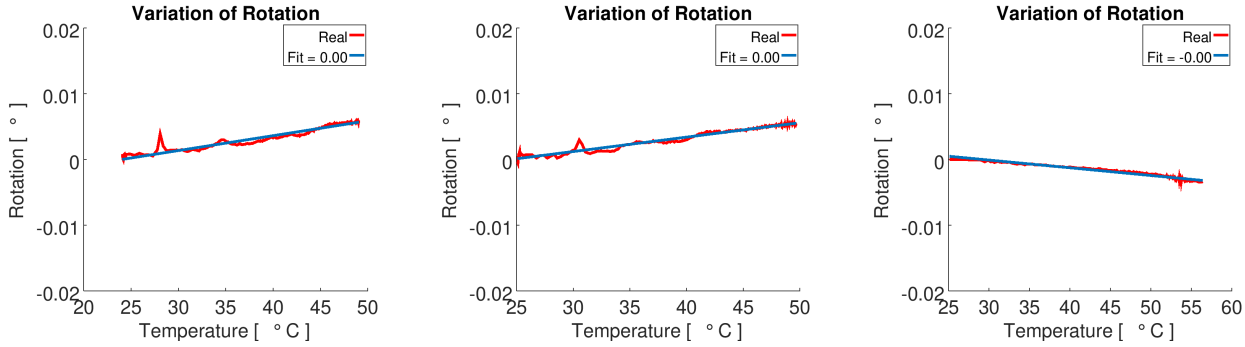

Figure. 6.7 – Estimated rotation : dataset 1-3 (from left to right).

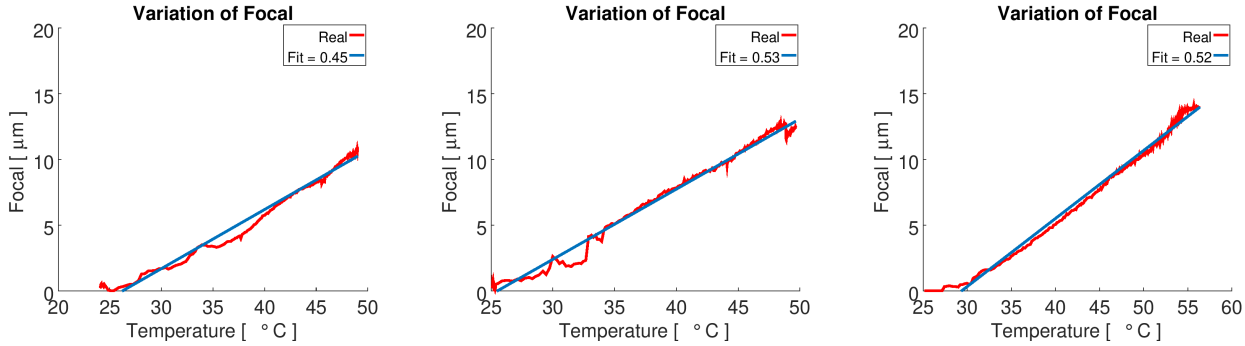

Figure. 6.8 – Estimated focal length : dataset 1-3 (from left to right).

Type II acquisition The sensor temperature barely changes during the experiment. Consequently, the acquisition serves to quantify the impact of unidentified and uncontrolled sensor deformations, e.g. the ambient humidity or ambient temperature. The 2D deformation maps calculated for image couples are homogeneous across the image plane

and demonstrate no displacements along the x,y axes (cf. Figure. 6.9 and Table. 6.5). The result justifies that external factors have negligible effect and the observed deformation within type I acquisition is the sensor response to the raising internal temperature.

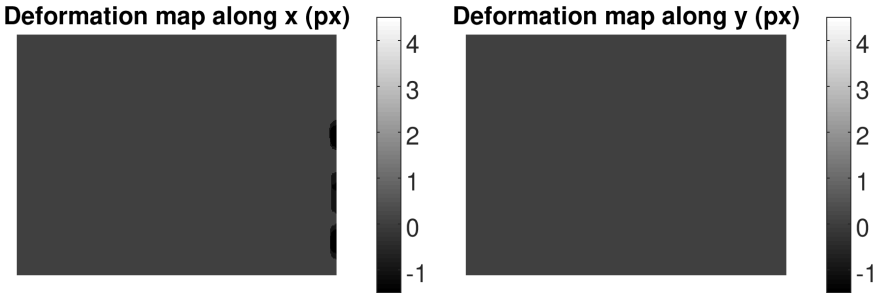

Figure. 6.9 – Example of deformation maps calculated along x and y in type II acquisition.

	min (px)	max (px)	mean (px)	std (px)
Axis X Couple 1	-0.04	0	-0.01	0.01
Axis Y Couple 1	0	0	0	0
Axis X Couple 2	-0.04	0.04	-0.01	0.02
Axis Y Couple 2	0	0	0	0

Table. 6.5 – Deformation computed for two image couples of type II acquisition.

6.4.3 Deformation determination with bundle adjustment

To confirm our previous findings, an independent method using the space resection algorithm and the bundle adjustment is conducted.

6.4.3.1 Experiment design

During the acquisition, the camera is fixed on a heavy tripod and observes a calibration field with GCPs. The camera temperature increases progressively as shown in Figure 6.10. The camera poses of a pre-calibrated camera (camera model Fraser [1997]) are firstly recovered with the space resection algorithm using all GCPs. Then, a bundle adjustment is performed where the previously computed poses are considered constant, and solely the focal length and the principal point are reestimated. The GCP image measurements are done manually in the first image. For subsequent images, automated cross correlation with respect to the first image is performed for GCP image measurements. See Table. 6.6 for information on temperature ranges, the calibration field and GSD.

6.4.3.2 Results

Figure 6.11 shows the reprojection error for each GCP. The red curve depicts the GCP reprojection error of the first image and gives an indication of the pose estimation

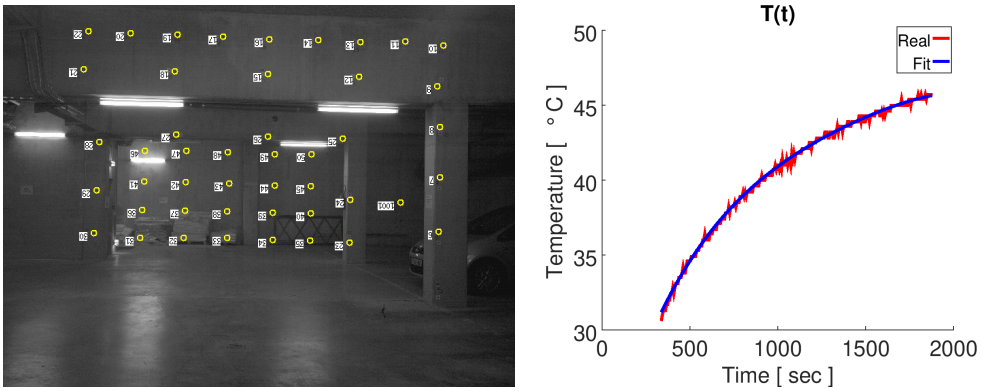

Figure. 6.10 – The calibration field with GCPs (left) and temperature variation (right)

Acquisition time (min)	26
Number of images	263
Temperature range (°)C	[30.6, 45.7]
Mean Nb of GCPs / image	21
GSD range (mm)	[1.6, 4.0]
DOF Topometric Network	488
Mean GCP accuracy (mm)	1.7

Table. 6.6 – Information of dataset.

quality. The blue curve shows the average GCP reprojection error by estimating a focal length and a principal point per image. The reprojection error of the first image has an average of 0.57 px and a dispersion of 0.34 px while for the mean reprojection error, the average is of 0.16 px and the dispersion of 0.07 px. Small residuals indicate an accurate pose estimation and justify the imposition of the first image camera pose on other images. The estimation of the focal length and the principal point for images is therefore considered reliable.

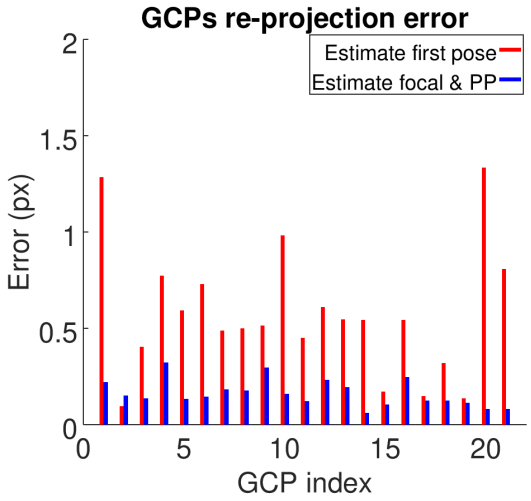

Figure. 6.11 – GCP reprojection error of the first image and mean GCP reprojection error of all images ; x-axis represents the GCP index

Figure. 6.12 shows the variation of the focal length and the principal point with temperature. The variation of the focal length is coherent with the results obtained in Section 6.4.2 but the planimetric trend of the principal point does not correspond to the translation parameters. This is partly due to the fact that the acquisitions spread over a long time. With this, however, one can conclude that the thermal deformation can be modeled and is reproducible at least for focal length.

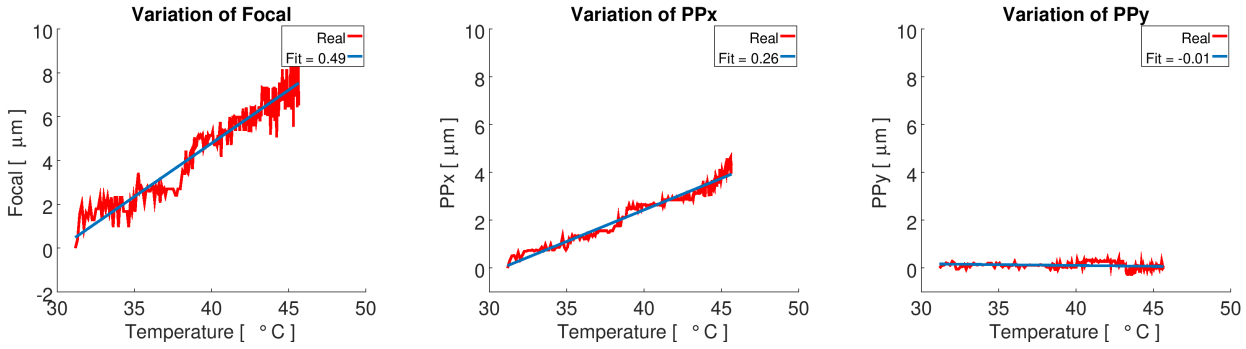

Figure. 6.12 – Evolution of estimated focal length and principal point values.

6.5 Experimental evaluation

The thermal model estimated in the previous section is here applied to two real case studies, one terrestrial (cf. Section-6.5.1) and one aerial (cf. Sections-6.5.2).

The mean absolute residual on GCPs and a loop closing error are the measures adopted to evaluate the precision of respective experiments. Firstly, the photogrammetric restituition is performed in a relative scale with only tie points as observation. Then, the relative result is moved to the coordinate system of GCPs with a 7-parameter 3D similarity transformation and no bundle block adjustment is followed. Therefore, the weight of GCPs is not discussed thereafter. Note that even though for some experiments the accuracy of GCPs is of the same order as the image GSD, one can still draw conclusion on the internal accuracy. Figure. 6.13 presents the processing work flow. At all instances, the results corrected for the thermal effect are compared with the results based on original images. To avoid the increase of the computation time, corrections are not applied on the totality of pixels but on tie points and GCP image observations.

6.5.1 Terrestrial acquisition

The dataset is composed of a sequence of images taken around a pylon (cf. Figure. 6.14). Convergent images and images rotated by 90° are acquired. The first and the last image pairs are taken from the same viewpoint forming a closed acquisition loop. Table. 6.7 gives details on the terrestrial dataset.

The camera relative orientations are calculated in a self-calibrating bundle block adjustment using only SIFT tie points as observations. The camera calibration model employed is Fraser [1997].

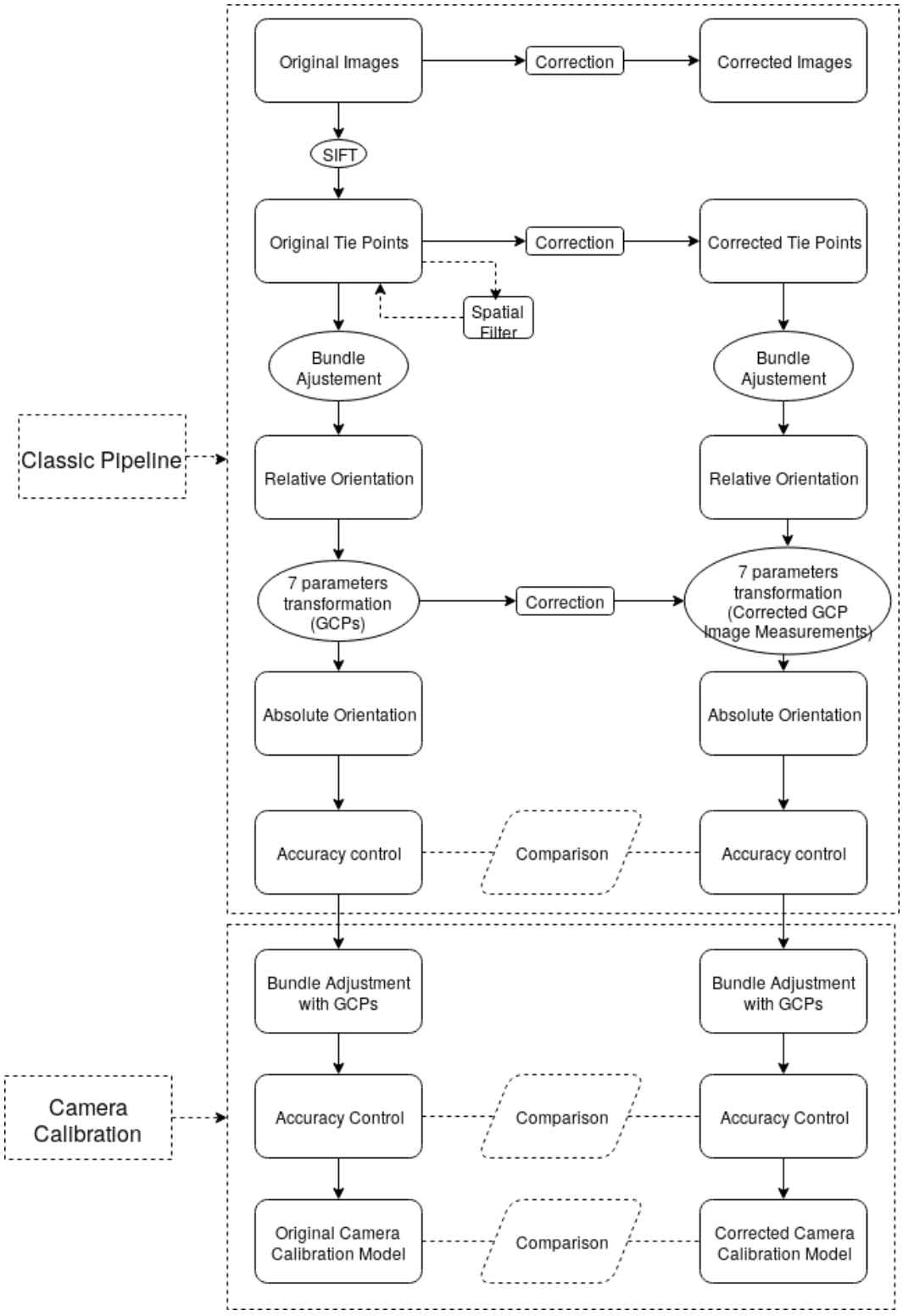

Figure. 6.13 – Processing workflow.

The scene is equipped with a network of GCPs measured with a total station (cf. Table. 6.8). Six stations are employed to avoid grazing angle measurements and each target is visible from at least 4 stations. The stations are installed with a ”forced centering” strategy to overcome the centering errors. To avoid the height measurement errors, the survey is completed in a free station mode. The measurements are adjusted in Comp3D – a geodetic adjustment software developed at IGN.

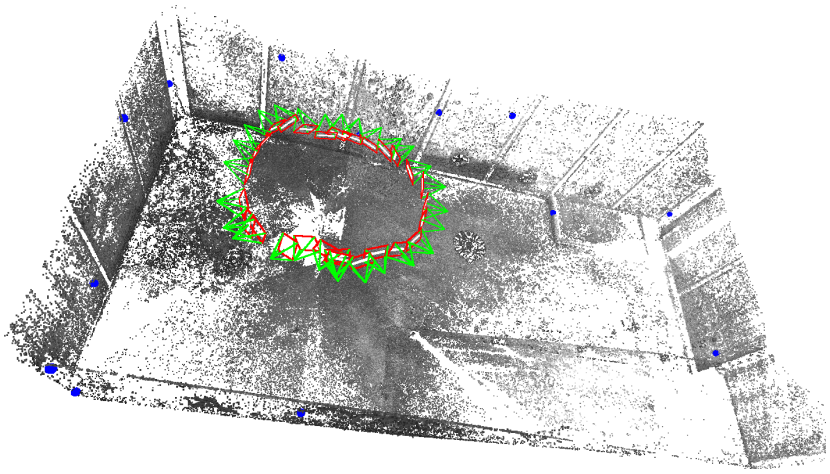

Figure. 6.14 – Geometry of terrestrial photogrammetric acquisition with GCPs (blue)

Number of images	28
Number of GCPs	13
Acquisition time (min)	14
Temperature range (°C)	[23,31]
GSD range (mm)	[0.5,1.5]

Table. 6.7 – Information on terrestrial dataset

Horizontal angle uncertainty	5.4×10^{-4}°
Vertical angle uncertainty	5.4×10^{-4}°
Distance uncertainty	1 mm
DOF of Topometric Network	111
Mean GCP accuracy (mm)	0.3

Table. 6.8 – Specifications of the total station

The GCPs are exploited in both two following experiments for relative to absolute transformation. Nonetheless, to evaluate the results, GPCs are used only in the **with closed loop** case in Section 6.5.1.1. In Section 6.5.1.2, a GCP-free evaluation is performed in the **without closed loop** scenario.

6.5.1.1 Results with closed loop

Three correction maps issued from the three type I acquisitions (cf. Section 6.4.2) are applied to the acquired dataset. Note that we presented the thermal model as 2D similarity transformation because of its simplicity of physical interpretation. In practice, generic polynomials are applied to ensure a finer modeling. The GCP residuals are presented in Table. 6.9.

The order of the GCP residual is relatively high compared to the GSD size. It is due to the fact that no bundle block adjustment is performed after the 7-parameter 3D similarity transformation. One can observe, however, that the relative accuracy is improved when thermal corrections are introduced. Out of the three correction stra-

	min (mm)	max (mm)	mean (mm)	std (mm)
Original	1.8	7.9	4.7	1.8
Correction 1	2.2	6.7	4.2	1.4
Correction 2	2.4	6.5	4.2	1.3
Correction 3	0.5	7.3	3.2	2.0

Table. 6.9 – Residuals on GCPs after the 7-parameters transformation. Correction 1-3 are issued from Dataset 1-3 (cf. 6.4.2), respectively.

tegies, the **Correction 3** brings the highest precision gain and relates to the highest temperature measurement precision, as explained in Section 6.4.2. All in all, with the adopted methodology and for similar acquisitions, an accuracy improvement of a factor of 1.5 can be anticipated.

6.5.1.2 Results without closed loop

The same set of images is used in this experiment but the dataset is processed as an open loop (cf. Figure. 6.15). That is, the first and the last pair of images within the acquisition observe the same scene but no tie points are calculated to relate them. Topologically speaking, it is a linear acquisition. Such image configuration is unfavourable and causes the so-called *bowl effect* (James and Robson [2014]; Nocerino et al. [2014]). In this experiment we investigate to what extent thermal correction can mitigate this phenomenon.

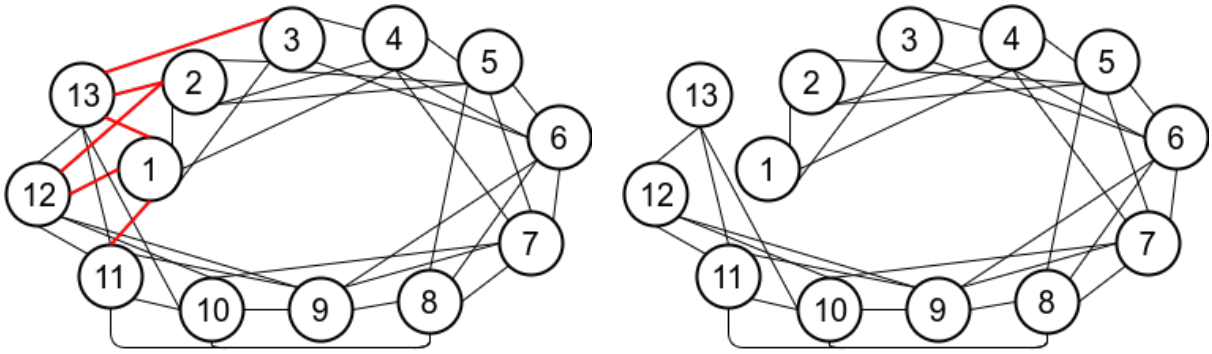

Figure. 6.15 – Image connectivity graph for standard configuration with closed loop (left). Red lines depict connectivities removed in configuration without closed loop ; Image connectivity graph for configuration without closed loop (right). The closing error is calculated on tie points of images 1-2-12-13.

Tie points extracted from the first and the last two images (4 images in total) are triangulated respectively to obtain two sets of 3D positions. The closing error corresponds to the distances between these two sets of 3D points. Without the presence of *bowl effect*, the distances should be close to zeros. See Table. 6.15 for the statistics of the closing error across the tie points commonly seen by the four images. The closing error declines by a factor of ≈ 3.5 when the thermal correction is applied. Consequently, the *bowl effect* is reduced and a better internal accuracy is obtained.

	min (mm)	max (mm)	mean (mm)	std (mm)
Original	1.4	19.8	6.2	2.1
Correction 3	0.0	13.9	1.7	1.6

Table. 6.10 – Statistics of the closing error.

6.5.2 Aerial acquisition

The dataset is composed of a 2-strip drone flight along a 500 m road. The objective of this experiment is to investigate the accuracy gain when performing the thermal effect correction in cartographic applications, where accuracy expectations are often very stringent. The acquired images, the imaging geometry and further flight characteristics are given in Figure. 6.16 and Table. 6.11, respectively.

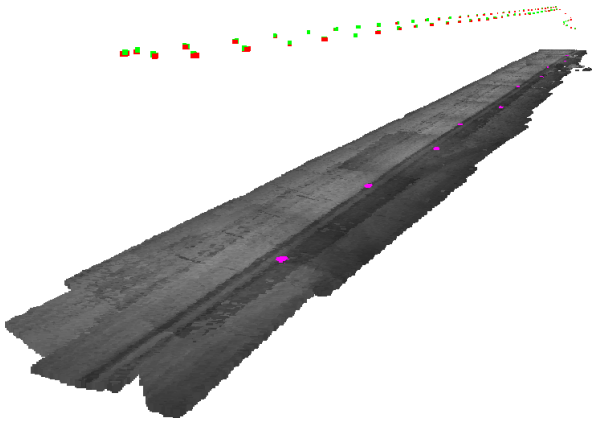

Figure. 6.16 – Geometry of aerial acquisition and distribution of GCPs (in purple) along the trajectory.

Temperature range (°C)	[22.7,28.8]
Flight time (min)	15
Number of images	77
Number of GCPs	10
Flight height (m)	70
GSD (cm)	1
GCP accuracy (cm)	1
Overlap	75%,75%

Table. 6.11 – Information of aerial acquisition.

As a linear acquisition geometry is unfavourable for self-calibrating purposes, we pre-calibrate the camera by performing a terrestrial acquisition. Two camera models are estimated with original observations and the thermal effect corrected observations, respectively.

During a drone survey, the temperature changes can stem from various factors, e.g., the sun, the wind, the internal heating of the camera. In this experiment, however, we interest in the camera temperature change itself regardless of the source.

6.5.2.1 Camera pre-calibration

The terrestrial calibration field contains a number of GCPs and represents a 3-dimensional scene. The camera internal and external parameters are estimated in a self-calibrating bundle block adjustment with tie points and GCPs. See Fig 6.17 and Table. 6.12 for more information on the calibration field and the acquisition itself.

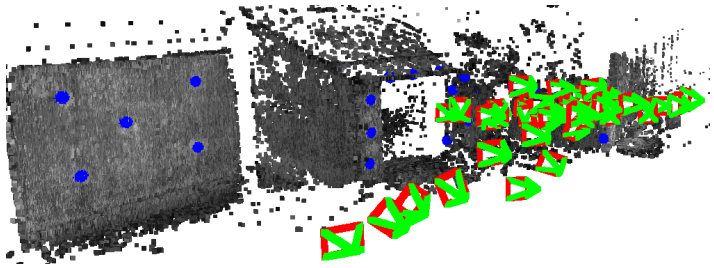

Figure. 6.17 – The terrestrial calibration field used for pre-calibrating the camera.

Number of images	43
Temperature range (°C)	[34.2,36]
Number of GCPs	28
GSD range (mm)	[0.5,1.5]
Mean GCP accuracy (mm)	0.5

Table. 6.12 – Pre-calibration acquisition data and accuracy measures.

Two calibration models are established – with and without the thermal effect being corrected. The temperature change, despite being small, has an impact on the camera calibration, and subsequently on the geometric accuracy of the drone survey. Both calibration estimated models can be compared as follows :

$$d(\zeta, \zeta^{'}) = \min_{\mathcal{R}} \iint ||\zeta - \mathcal{R} \cdot \zeta^{'}||^2 dxdy \tag{6.4}$$

where : ζ estimated internal model with original observations ;
$\zeta^{'}$ estimated internal model with corrected observations ;
$\mathcal{R}$ estimated rotation

Results The processing strategy follows the scheme as given in Section 6.5.1. See Figure. 6.18 for the image residuals of GCPs.

We note that for an identical processing, taking into account the temperature effect gives a slightly better GCP reprojection error statistics, even if the impact is almost negligible. This is explained by the fact that, the variation of temperature is almost insignificant (1.6°C) and the GCP reprojection errors is rather dominated by GCP image measurements. Comparison between the the two camera models estimated with and without thermal effect correction on observations is shown in Fig 6.19.

With Figure. 6.19 one can read that the temperature introduces a bias of 0.05 px, displacements of up to 0.33 px are observed at the image borders. The mean deviation

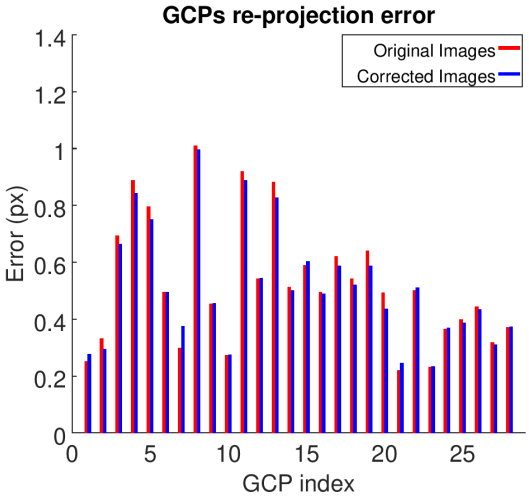

Figure. 6.18 – GCPs reprojection error for camera pre-calibration dataset.

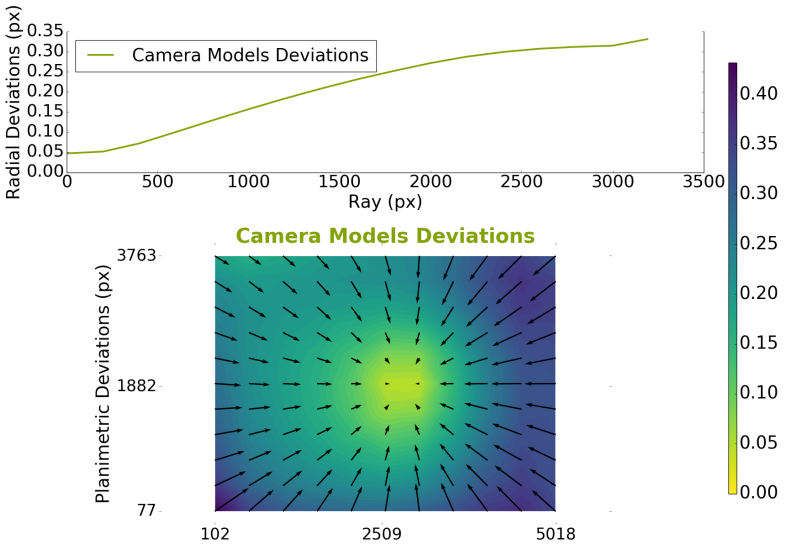

Figure. 6.19 – Comparison of the two estimated internal camera models

on the whole image sensor is 0.23 px. Despite the small change of camera temperature (1.6°C), the impact on the estimated camera model is measurable. Nevertheless, the interpretation of these changes in terms of 3D photogrammetric accuracy can be tricky. In this case, an independent aerial acquisition is carried out with the two estimated camera models being served for camera pre-calibration (cf. 6.5.2.2).

6.5.2.2 UAV acquisition

No measurements of the external temperature during the flight are available. Nonetheless, the variations are minimized by low-altitude flight (70m), short flight duration (15mins) and low speed (2m/s). The GCPs are measured using GNSS RTK surveying, and the evaluation is carried out on GCPs, after having transformed the relative result to the coordinate system of GCPs. Concerning the camera model, the two pre-calibrated

camera models discussed above were used in the processing.

Results Table. 6.13 report on statistics of GCP residuals for both original and corrected images. There is a clear residual decreasing tendency for most of the GCPs. The results prove that an accuracy improvement of a factor of ~ 1.4 can be anticipated for similar imaging conditions.

	min (mm)	max (mm)	mean (mm)	std (mm)
Original images	5.9	39.6	21.4	11.0
Corrected images	5.9	24.9	15.5	6.6

Table. 6.13 – Residuals on GCPs fo the UAV experiment.

6.6 Conclusion

In this chapter, we presented different strategies for the study of thermal deformation on images introduced by the variation of image sensor temperature. To our best knowledge, this is the first time the issue of thermal deformation is studied in the context of light weight metric camera devoted to UAV photogrammetric acquisitions.

Two modeling techniques were investigated – one with the image correlation technique, and the other using the bundle adjustment routine. In either scenario the sensor response to temperature was interpreted with a 2D similarity transformation.

The image matching experiment proved that the thermal deformation had an impact on internal camera parameters (e.g., focal length, principal point) and that the image sensor temperature change was the main cause. This method for quantifying the deformation is complete and exhaustive since it allows to study the deformation for every pixel of the image sensor. A good repeatability over time of the focal length variation (0.4-0.5 µm/°C) was observed and the variation corresponds to results presented in Merchant [2006, 2012]. The impact of the thermal deformation on translation and rotation differ over time, but the variation of rotation remains insignificant (less than 0.02 px/°C during acquisition). The thermal deformation is therefore reproducible and can be modeled and corrected. Further investigations are required to study the long term stability.

The experiment with the bundle block adjustment and spatial resection confirmed the repeatability of the thermal impact on focal length, with a different technique than image matching and independent dataset. The same tendency for focal length expansion was observed (0.5 µm/°C) when the image sensor underwent a temperature increase.

With terrestrial and aerial dataset, a better photogrammetric accuracy was achieved when taking the image sensor thermal effect into account. For the terrestrial dataset, the photogrammetric accuracy was improved by 1.5 times in standard acquisition configuration. To quantify the *bowl effect*, a loop closing error was examined. This approach showed that by taking into account the thermal deformation, the *bowl effect* was de-

creased by a factor of 3.6. For the aerial dataset in a linear configuration, an accuracy gain by a factor of 1.4 was observed.

6.7 Further Work

The long term stability of the thermal effect should be further studied. Although the reproducibility on the focal parameter has been verified thanks to Dataset 3 of section 6.4.2, which is acquired 4 months after the first ones, we cannot yet be conclusive about the stability of the thermal deformation over time.

Nevertheless, even if a calibration is required on a regular basis, our calibration method based on 2D matching is simple to implement and fully automated. A possible limiting factor of the calibration strategy is the determination of interior parameters in a close range configuration and its use in aerial configurations (Lichti et al. [2008]).

In the meanwhile, we observed an improvement of accuracy for an aerial dataset (Section 6.5.2) and the thermal effect seems, at the first order, independent of the variation of interior parameters. We can summarize our suggestion as follows :

$$\begin{aligned} \mathcal{C}(T,d) =& \mathcal{C}(T_0,d) + \frac{\partial \mathcal{C}_{(T_0,d)}}{\partial T}\delta T \\ =& \mathcal{C}(T_0,d) + \frac{\partial \mathcal{C}_{(T_0,d_0)}}{\partial T}\delta T + \frac{\partial^2 \mathcal{C}_{(T_0,d_0)}}{\partial T \partial d}\delta T \delta d \end{aligned} \tag{6.5}$$

where : $\mathcal{C}(T,d)$ is a correction function depending on temperature T and field depth d ;
T_0 is the reference temperature ;
d_0 is the field depth for calibration

The 2nd order term $\frac{\partial^2 \mathcal{C}_{(T_0,d_0)}}{\partial T \partial d}\delta T \delta d$ can be considered negligible and the correction function can be expressed as :

$$\mathcal{C}(T,d) = \mathcal{C}(T_0,d) + \frac{\partial \mathcal{C}_{(T_0,d_0)}}{\partial T}\delta T \tag{6.6}$$

Under this assumption, the in-lab close-range calibration procedure is still valid even at considerable aerial operating distances.

Finally, experiences should be carried out with different image sensors to better study this phenomena.

Chapter 7

Study of rolling shutter effect

Contents

This chapter corresponds to the following publication :

- **Zhou, Y.**, Daakir, M., Rupnik, E., Pierrot-Deseilligny, M. (2020). A two-step approach for the correction of rolling shutter distortion in UAV photogrammetry. *ISPRS journal of photogrammetry and remote sensing, 160*, 51-66.

In this chapter, a method of improving consumer grade cameras with rolling shutter is proposed. It consists of correcting the image deformation introduced by the rolling shutter mechanism. Two calibration methods of the rolling shutter readout time and one two-step method of rolling shutter correction are presented.

7.1 Introduction

The use of consumer grade unmanned aerial vehicles (UAV) for photogrammetric applications is becoming increasingly ubiquitous thanks to its low cost, good portability, ease of use and high flexibility (Nex and Remondino [2014]; Vautherin et al. [2016]).

A great variety of consumer and professional cameras can be found on the market nowadays. Digital single-lens reflex cameras (DSLRs) have replaced film-based SLRs and remain the most popular type of interchangeable lens camera. There are two main categories of image sensor, complementary metal-oxide semiconductor (CMOS) sensor and charge-couple device (CCD) sensor. CMOS sensors' lower cost and lower power consumption compared to CCD sensors make them a common choice for consumer and pro-sumer cameras. The vast majority of CCD sensors are equipped with global shutter whereas CMOS sensors often employ rolling shutters.

Despite the fact that certain UAV manufacturers propose UAVs equipped with global shutter cameras, a large proportion is still equipped with rolling shutter complementary metal oxide semiconductor (CMOS) sensors. In a rolling shutter readout, not every portion of the image sensor is exposed at the same time but in a progressive motion as in traditionnal dual curtain focal-plane shutters. Additional distortion in image space can be found when the object or the image sensor is moving during the exposure, which is normally the case for aerial photogrammetric acquisitions. Without proper modeling and processing, the rolling shutter effect can degrade the accuracy of photogrammetric reconstruction by a wide margin.

In this chapter, a two-step rolling shutter correction method is presented : we assume that the rotational velocity is negligible compared to the translational velocity. This assumption is adopted for the following reasons : (1) the simulation results in Section 4.3.3 confirm this assumption ; (2) the camera rotation is often diminished by for instance, a stabilized mount, as in our experiment ; (3) we don't really have access to angular information in our experiment. The camera translational velocity is estimated with time information in image metadata and camera positions issued from an initial bundle block adjustment ; the camera positions can also be extracted when GNSS data are available. Afterwards, the camera position at exposure of each line is recovered and the observations in image space are rectified accordingly. This method is implemented in *MicMac*, a free, open-source photogrammetric software (Rupnik et al. [2017]). To evaluate the performance of the proposed method, four datasets of block and corridor configurations are processed without and with the rolling shutter correction. Comparisons with two mainstream photogrammetric software : *AgiSoft MetaShape* and *Pix4D* are carried out with the same datasets and the same configurations.

7.2 State of the art

A great deal of studies have been conducted on the rolling shutter effect by the photogrammetry and computer vision communities. In Ait-Aider et al. [2006], the image deformation introduced by rolling shutter is leveraged for the estimation of instantaneous 3D pose and 3D velocity. The proposed method assumes the object motion to be uniform during the image exposure. It gives good 3D pose estimation in non-planar cases whereas for planar cases the accuracy is less satisfying. A generic camera model is given in Magerand and Bartoli [2010] for handling both uniform and non-uniform camera motions. A concept of dynamic pose is proposed, similarly to a push-broom camera, the pose is written as a function of the scan-line being considered. A projective geometry of the rolling shutter camera and how it is affected by different types of camera motion are presented in Meingast et al. [2005]. In the case of fronto-parallel motion, the camera is shown to be modeled as an X-slit-camera.

Substantial researches are carried out to compensate the rolling shutter effect in image space. In Liang et al. [2008], an image space analysis of the rolling shutter effect is described, the compensation of the distortion is performed with global planar motion estimation, parametric curve fitting and scanline realignment. By assuming the motion to be smooth and performing curve interpolation for each pixel, the rolling shutter distortion in videos is rectified in Sun and Liu [2012]. Klein and Murray [2009] estimate velocities for each image from adjacent images and compensate the tie points. Chun et al. [2008] described the rolling shutter distortion in terms of 2D velocity and implemented an affine transformation correction. Sun et al. [2016] computed a sequence of affine transformation represented by a multilayer neural network for the compensation of rolling shutter effect. A mixture of homographies is explored for a calibration-free rolling shutter removal in Grundmann et al. [2012]. The method proposed in Ito and Okatani [2017] assumes a linear-rotation-only camera motion, the problem is recast as camera self-calibration with a varying skew and aspect ratio for each image sequence.

Focuses are also given on rolling shutter bundle adjustments. Hedborg et al. [2011] demonstrated a structure and motion scheme for rolling shutter videos which works with general camera motions. Saurer et al. [2016] adopts a constant translational and rotational velocity parametrization for the camera pose and proposes a cost function for Bundle Adjustment (BA) that models the rolling shutter effect. *Pix4D* assumes as well a constant camera motion and describes the rolling shutter effect with a 6-parameter model (Vautherin et al. [2016]). As for *Agisoft MetaShape*, its rolling shutter correction method is not presented publicly.

7.3 Problem formulation

For modern camera equipped with a rolling shutter, the image sensor is activated and read out one row at a time. The exposure takes place between the time the first row is exposed and the time the last row is read out. The readout time for each frame is constant and does not vary with exposure parameters. In a word, an important delay due to the readout time can be found between exposures of the first and the last row, which introduces distortion when imaging a mobile object or the image sensor itself

moves during exposure. Figure 7.1 gives an illustration of the general rolling shutter scheme.

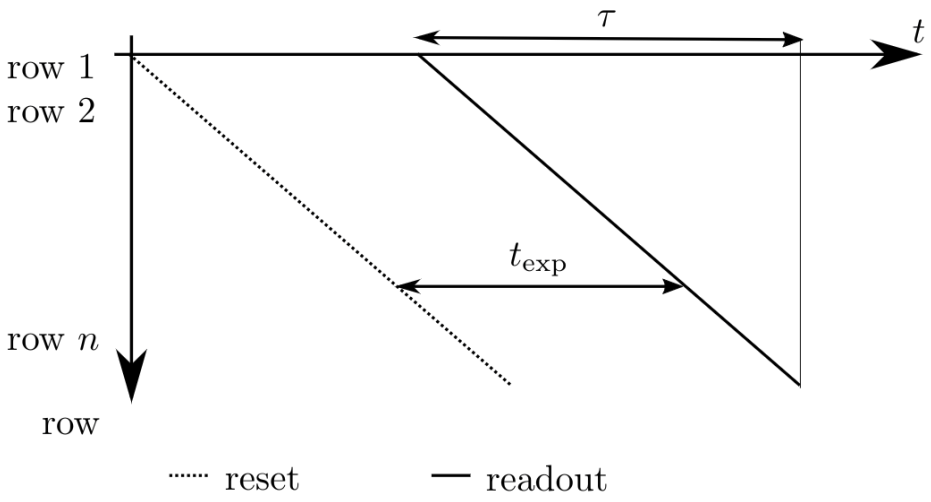

Figure. 7.1 – Rolling shutter readout scheme. The sensor is exposed row by row at a constant speed. After the exposure duration t_{exp} , the sensor starts the readout row by row. At time t= 0 the exposure of the first row takes place. It is then read out at time $t = t_{exp}$. Consecutive rows are exposed and read out one after the other. The sensor readout is finished after the rolling shutter readout time τ. Source : Vautherin et al. [2016]

In the case of aerial photogrammetric acquisition, the speed of an unmanned aerial vehicle (UAV) embarking with optical sensors can reach 10 m/s. Typically, the readout time of consumer grade cameras varies in the range of 30 ms to 80 ms, which results in a non-negligible camera position change between the beginning and the end of exposure.

7.4 System and calibration

7.4.1 Drone and camera

For the study of rolling shutter effect as well as the aerial data acquisition, the DJI Mavic 2 pro (Figure 7.2) and its original camera, a Hasselblad L1D-20c camera are employed. The camera is equiped a 3-axis gimbal to provide a stable, smooth footage for image acquisition. The camera specifications are given in Table 7.1 :

Sensor	1″ CMOS Effective Pixels : 20M
Lens	35 mm Format Equivalent : 28mm
Still image size	5472 × 3648

Table. 7.1 – Camera specifications (https://www.dji.com/uk/mavic-2)

Figure. 7.2 – DJI Mavic 2 Pro

7.4.2 Calibration of readout time

No specifications of the rolling shutter readout time are given on the website of DJI. It occurs sometimes that this information remains absent and is not given by camera manufacturers since it may be viewed as a camera defect. In one blog of Pix4D, the readout time of 6 DJI models are listed, however the model employed for our research, DJI Mavic 2 Pro, is not included [1]. Therefore, we propose here two approaches to calibrate the rolling shutter readout time for the following reasons : (1) the readout time is often unprovided by the camera manufacturer ; (2) there are few methods proposed by the community to calibrate the readout time ; (3) it is more rigorous to have a control on the readout time even when it is given ; (4) from an educational point of view, it is a good exercise for students to understand the rolling shutter effect.

7.4.2.1 Approach 1 : Siemens star

System setup

The setup of the first readout time calibration system is shown in Figure 7.3 : the drone is placed in front of a Siemens star with the camera facing front. The Siemens star consists of a set of spokes radiating from a common center which become wider as they get further [2] ; it is connected to a motor and can rotate in a constant speed. A magnet is fixed on the back of the Siemens star. The time interval between its two passages is detected by a magnetic field sensor, the instantaneous angular frequency is then calculated and displayed on a screen at bottom left (see Figure 7.3a).

Two sets of photos are acquired with DJI Mavic 2 Pro ; the first set is acquired with the Siemens star being static, the second one with the Siemens star rotating in a certain angular speed. The photographic parameters are configured identically, the shutter speed is set to 1/4000 s so that the exposure time t_{exp} is negligible with respect to the readout time τ. One example photo of each set is given in figure 7.4.

1. https://www.pix4d.com/blog/rolling-shutter-correction
2. https://en.wikipedia.org/wiki/Siemens_star

(a) The readout time calibration system

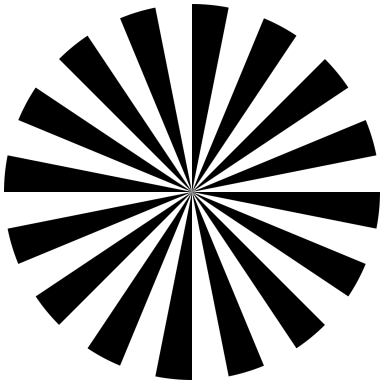

(b) The Siemens star

Figure. 7.3 – An illustration of the system setup for readout time calibration.

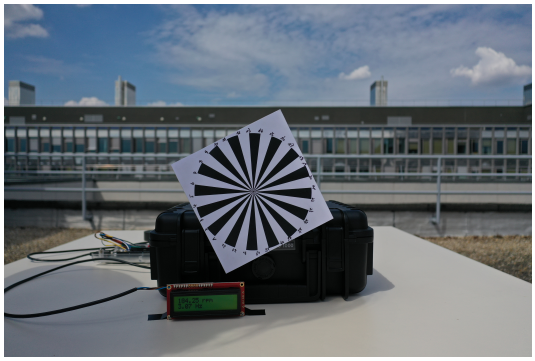

(a) Image taken with static object

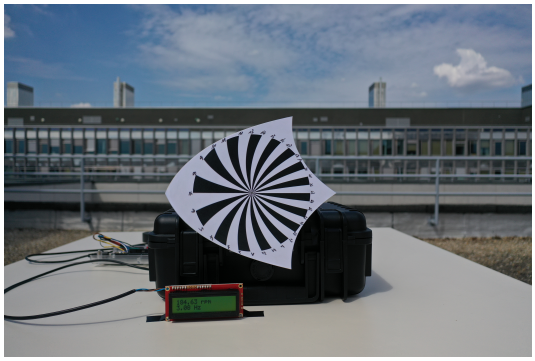

(b) Image taken with rotating object

Figure. 7.4 – An example of images taken with a rolling shutter camera.

Mathematical model

The mathematical model for the estimation of readout time τ is illustrated in Figure 7.5. For each spoke of the Siemens star, two points A_1, A_2 can be identified and share the same distance R to the center O. The image sensor of in total L rows is exposed and read out from top to bottom with a readout time τ. The Siemens star rotates counterclockwise with a constant angular velocity ω.

Assume that at $t = t_1$, the row y_{A_1} of the image sensor is exposed and read out ; the point A_2 has not been imaged yet. At $t = t_2$, the point A_2 moves to point A'_2 and the row $y_{A'_2}$ of the image sensor is exposed. The time interval between these two exposures can be expressed by :

$$t_2 - t_1 = \frac{y_{A'_2} - y_{A_1}}{L} \cdot \tau \tag{7.1}$$

Note the angles $\theta = \angle A_1 O A_2$ and $\theta' = \angle A_1 O A'_2$, the time interval $t_2 - t_1$ can also be expressed by :

$$t_2 - t_1 = (\theta' - \theta)/\omega \tag{7.2}$$

The two angles θ and θ' have the following relations :

$$\cos(\frac{\pi - \theta}{2}) = \frac{\overline{A_1 A_2}}{2R}, \quad \theta = \pi - 2 \cdot \arccos(\frac{\overline{A_1 A_2}}{2R}) \tag{7.3}$$

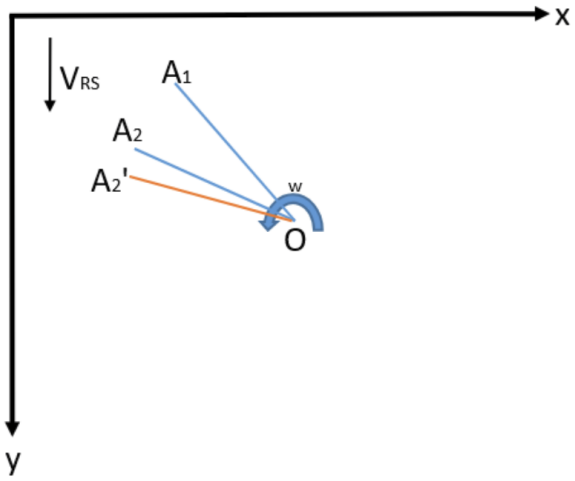

Figure. 7.5 – Illustration of the mathematical model for the estimation of readout time.

$$\cos(\frac{\pi-\theta'}{2}) = \frac{\overline{A_1A_2}}{2R}, \quad \theta' = \pi - 2\cdot\arccos(\frac{\overline{A_1A_2}}{2R}) \tag{7.4}$$

Given (7.1) and (7.2), one can obtain :

$$\tau = \frac{L\cdot(\theta'-\theta)}{\omega\cdot(y_{A_2'}-y_{A_1})} \tag{7.5}$$

By replacing θ and θ' with (7.3) and (7.4), the readout time :

$$\tau = \frac{2L\cdot[\arccos(\frac{\overline{A_1A_2}}{2R}) - \arccos(\frac{\overline{A_1A_2'}}{2R})]}{\omega\cdot(y_{A_2'}-y_{A_1})} \tag{7.6}$$

To generalize,

$$\tau = \frac{L\cdot|\theta'-\theta|}{\omega\cdot|y_{A_2'}-y_{A_1}|} \tag{7.7}$$

Calibration results

For each spoke of the Siemens star, two points are identified and manually measured, which adds up to 32 points in one image. Figure 7.6 shows the positions of these 32 points in the above-mentioned two cases : the Siemens star remains static (left) and the Siemens star rotates (right), respectively. One can observe that, in the static case, the 32 points are equally separated as in object space. As for the case in which the Siemens star rotates counterclockwise and the image sensor is exposed from top to bottom, the distances between points on the left side are bigger than the ones on the right side. For points on the right side which ascend during the exposure, by the time the exposure moves to the next rows, points which were at a lower part of the image catch up and get to be exposed, hence a shorter distance between points.

A total of 154 point couples are extracted from the static/rotating image pair. Selections are made so that the two points involved for estimation are on the same side of the circle (e.g., only descend or ascend during imaging). A linear least squares fitting is performed with the *Curve Fitting Toolbox* in *Matlab*. Figure 7.7 demonstrates the fitting results. The estimated readout time $\tau = 56.4$ms with the R-squared (coefficient of determination) equals to 0.9997.

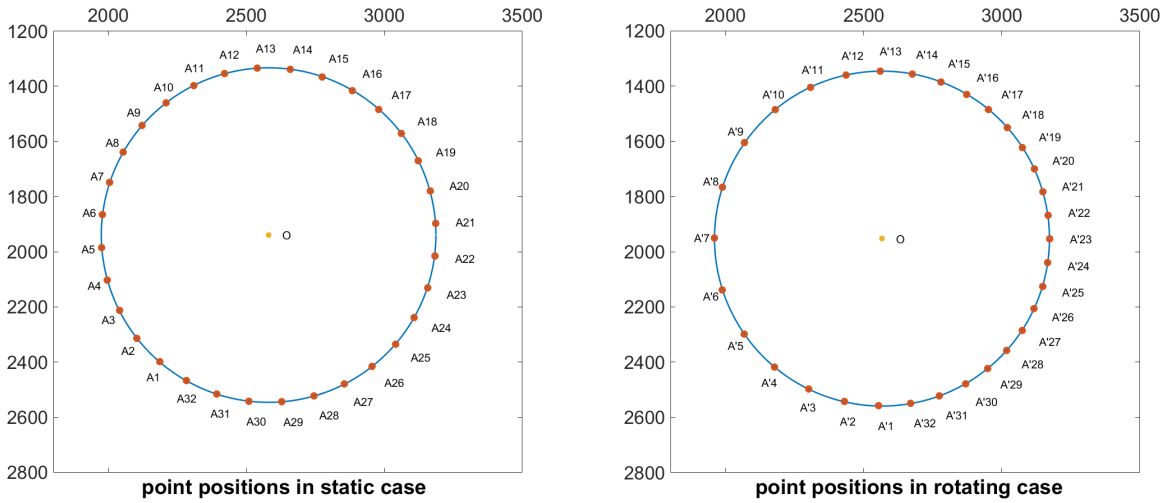

Figure. 7.6 – Point positions in images, image sensor is exposed from top to bottom in image space. **Left** : static case. **Right** : rotating case.

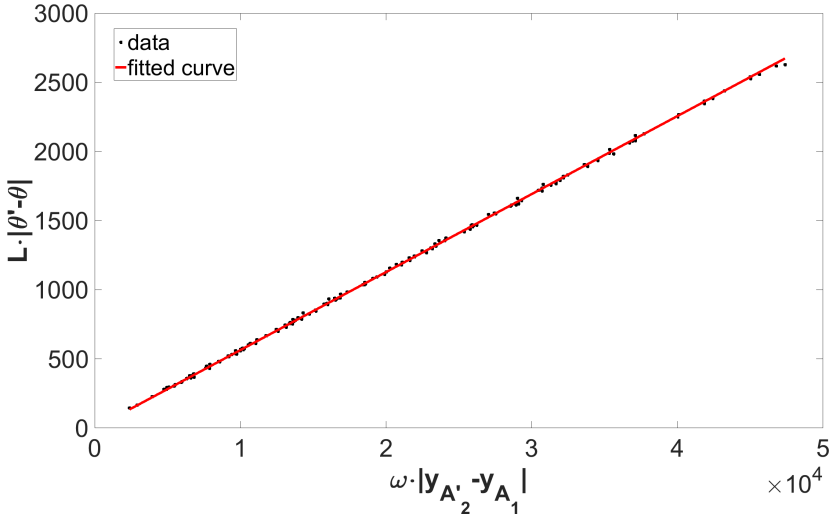

Figure. 7.7 – Linear fitting results for readout time estimation.

7.4.2.2 Approach 2 : bike wheel

The second approach for camera readout time calibration is less rigorous but easier to perform. The reason why we propose a second approach is, the first approach requires specific equipment that is not available for everyone. This second approach is an alternative for calibrating approximately the camera readout time with easy to get equipment. The fact that the calibration can be performed with common equipment makes it a good teaching material for students and the public. In fact, this approach is presented in the *Science Festival 2019* in Paris to illustrate the rolling shutter effect.

System setup

The calibration is carried out with a bike wheel, the drone is placed in front of the bike wheel with the camera facing front. The bike wheel consists of a hub shell and a set of spokes that are attached to the hub.

Two sets of photos are acquired with the drone camera as in *Approach 1* ; the first set is acquired with the bike wheel being static, the second one with the bike wheel rotating clockwise. While the wheel rotates, a video is taken as well with another camera. The video is leveraged to calculate *a posteriori* the angular velocity of the rotation. The photographic parameters are configured identically for the two acquisitions, the shutter speed is set to 1/320 s. See Figure. 7.8 for example photos.

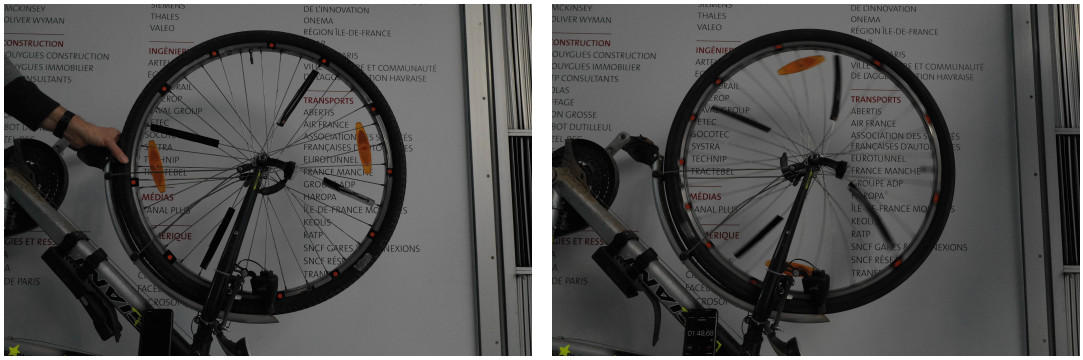

(a) Image taken with static object (b) Image taken with rotating object

Figure. 7.8 – An example of images taken with a rolling shutter camera.

Mathematical model

The mathematical model for the estimation of readout time τ is illustrated in Figure. 7.9. We simplify the model of bike wheel and assume that all spokes intersect at point O. The image sensor of L rows is exposed and read out from top to bottom. The wheel rotates clockwise with a constant angular velocity ω.

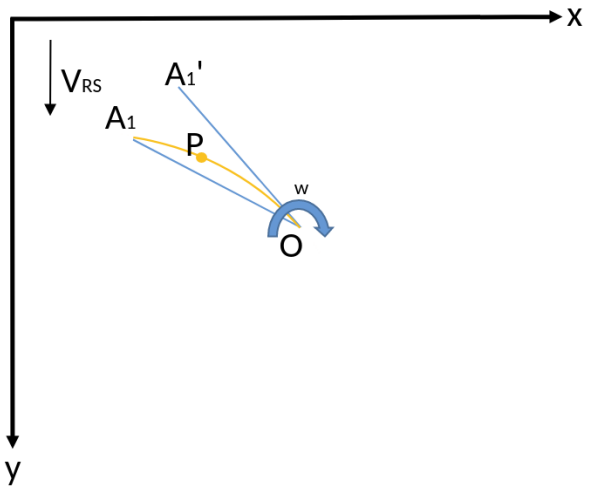

Figure. 7.9 – Illustration of the mathematical model for the estimation of readout time.

We study the imaging process of the spoke OA_1. At $t = t1$, the row y_{A_1} of the image sensor is exposed and read out. While the exposure continues, the spoke OA_1 rotates around point O clockwise ; by the time $t = t_2$ the row y_O is exposed, the spoke moves to OA_1'. Therefore, instead of being imaged as a straight line (in blue), OA_1 is imaged as a curve (in yellow). P is a point on the curve, the coordinates of point A_1, point O and point P are noted as (x_1, y_1), $(x_0, y_0$ and (x, y), respectively.

The time interval Δt between the exposure of A_1 and P can be expressed by :

$$\Delta t = \tau \cdot \frac{\Delta y}{L} = \tau \cdot \frac{y - y_1}{L} \tag{7.8}$$

Note the angle $\Delta\theta = \angle POA_1$, the time interval Δt can also be expressed by :

$$\Delta t = \frac{\Delta\theta}{\omega} \tag{7.9}$$

By combining (7.8) and (7.9), the readout time τ can be expressed by :

$$\tau = \frac{L \cdot \Delta\theta}{\omega \cdot \Delta y} \tag{7.10}$$

It is actually the same idea than *approach 1*.

Calibration results

For a chosen spoke, 30 points are extracted manually. For each point set $[A_1, P, O]$, an estimation of the readout time is obtained. A linear least squares fitting is performed with the *Curve Fitting Toolbox* in *Matlab*. Figure 7.10 demonstrates the fitting results. The estimated readout time $\tau = 50.2$ms with the R-squared (coefficient of determination) equals to 0.9544.

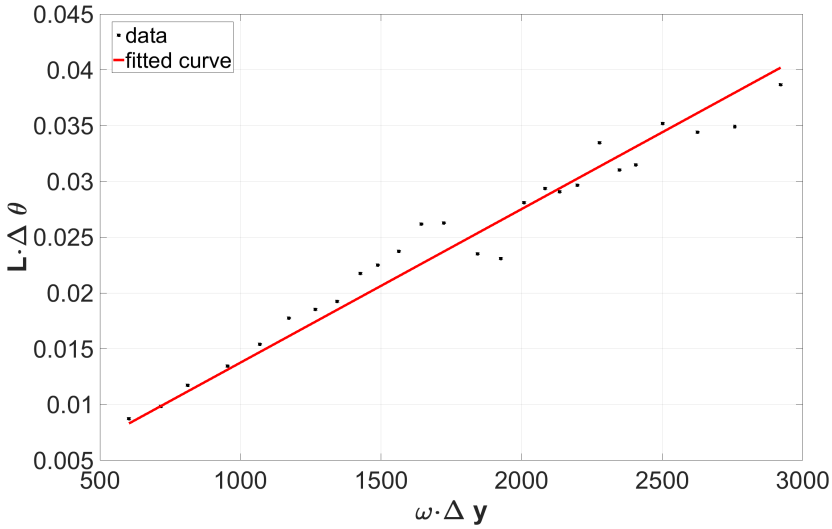

Figure. 7.10 – Linear fitting results for readout time estimation.

The estimation results of the two approaches are coherent. For the following experiments, the estimation result of *Approach 1*, the readout time $\tau = 56.4$ms is used.

7.5 Research design

To improve the accuracy of photogrammetric results, the following pipeline is proposed to correct the rolling shutter effect on images. Note that the assumption is made

that there is no variation of camera orientation during exposure. Firstly, the simulation results in Section 4.3.3 showed that the impact of angular motion is negligible compared to that of translational motion. Moreover, the camera employed here is equipped with a 3-axis gimbal for a stable imaging. Also, we do not have access to the angular information of the experiment. The proposed method is a two-step solution which in the first instance estimates the camera translational velocity from an initial bundle block adjustment result, then recovers the camera position for each line at exposure to rectify image measurements. The implementation is carried out as follows :

Step 1 : obtain an initial solution

A standard photogrammetric pipeline is performed to obtain an initial solution. It consists of identifying common feature points between overlapping images and recovering their poses firstly in a relative coordinate system. The geo-referencing and a second bundle block adjustment in absolute scale are carried out with the help of ground control points (GCPs).

Step 2 : calculate image sensor velocity

In our case with DJI Mavic 2 Pro, the time related information of the exposure is recorded in the metadata of each image. An initial solution of the camera position and orientation is issued after *step 1*. The velocity of one image is considered as the ratio between the displacement and the time interval of its two adjacent images. Note that the time related information in the metadata of one image is often rounded in second. Therefore, there is no much interest in applying a more sophisticated approach for the estimation of image sensor velocity.

We observed that the DJI Mavic 2 Pro gives erroneous GNSS measurements and the issue has not been fixed until after the acquisitions are conducted[3]. Therefore, the GNSS data are not explored. In the case where correct GNSS measurements are available, the camera velocity can be estimated more rigorously with the help of time information in image metadata and camera positions extracted from GNSS data ; the *Step 1* can then be skipped.

Step 3 : recover camera position at exposure

For image i, its camera position C_i is acknowledged with *Step 1*. In the case where the moving direction of the drone and the that of the rolling shutter are opposite (as in Figure 7.4), the acquired images are dilated compared to the ones obtained with global shutter. For an image sensor with L rows, the camera position C_i obtained with *Step 1* is closer to the instant camera position when the middle row $\frac{L}{2}$ of the image sensor is exposed. For row l, the time elapsed between when it is exposed and when the middle row is exposed can be calculated once the rolling shutter readout time τ is known. The readout time being small enough (less than 100 ms), the image sensor velocity V_{uav} is assumed to be constant during the readout phase and is calculated with *Step 2*. The

3. https://forum.dji.com/thread-186813-1-1.html

camera position C_i^l when the row l is exposed can be expressed then by :

$$C_i^l = C_i + V_{uav} \cdot \tau \cdot \frac{l - \frac{L}{2}}{L} \tag{7.11}$$

In a nutshell, from one camera position C_i, a set of camera positions $\left[C_i^0, \cdots, C_i^L\right]$ corresponding to row $[0, \cdots, L]$ are recovered.

Step 4 : correct image measurements

A set of images see a 3D point at $\mathbf{p} = [p_1, \cdots, p_n]^T$. The 2D observations $\mathbf{p}$ are extracted with feature detection algorithm (e.g. SIFT), the corresponding camera poses $\mathbf{\Omega} = [\Omega_1, \cdots, \Omega_n]^T$ are issued from *Step 1*.

Firstly, the 3D coordinates p of the point are recovered by performing a pseudo-intersection $\psi(.) : \mathbb{P}^2 \to \mathbb{P}^3$:

$$P = \psi(\mathbf{\Omega}, \mathbf{p}) \tag{7.12}$$

Then, the 3D point is reprojected on images with the projection function $\pi(.) : \mathbb{P}^3 \to \mathbb{P}^2$, which gives image measurements $\mathbf{p}' = [p'_1, \cdots, p'_n]$.

$$\mathbf{p}' = \pi(\mathbf{\Omega}, P) \tag{7.13}$$

The differences between these two sets of image measurements comes from random and systematic errors of feature detection and camera internal/external orientation calculation.

$$\delta\mathbf{p} = \mathbf{p}' - \mathbf{p} \tag{7.14}$$

A second reprojection is conducted with the corrected camera positions $\mathbf{\Omega}_c$ issued from *Step 3*,

$$\mathbf{p}'_c = \pi(\mathbf{\Omega}_c, P) \tag{7.15}$$

Then the obtained image measurements $\mathbf{p}'_c$ are rectified with image measurement residuals $\delta\mathbf{p}$,

$$\mathbf{p}_c = \pi(\mathbf{\Omega}_c, P) - \delta\mathbf{p} \tag{7.16}$$

The final image measurements $\mathbf{p}_c$ are considered the corrected observations. Figure 7.11 presents the relation between different image measurements mentioned above.

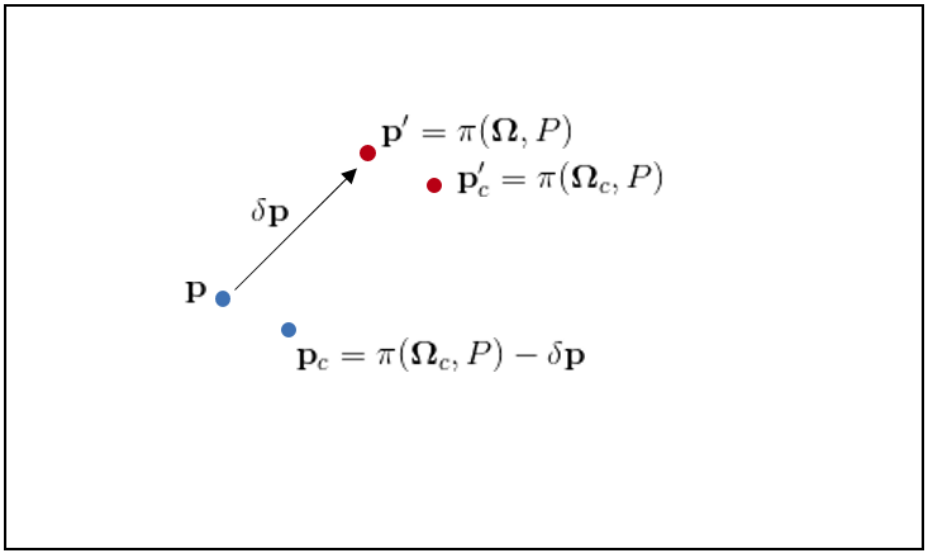

Figure. 7.11 – Illustration of image measurements.

7.6 Experiments and results

7.6.1 Introduction of datasets

The aerial acquisition is conducted on an aerodrome at Viabon, France. Figure 7.12 shows two zones that have been surveyed with the DJI Mavic 2 Pro. One zone in block configuration and one in corridor configuration, respectively.

Figure. 7.12 – Illustration of the two surveyed zones in block and corridor configurations.

The block configuration zone is about 150m × 200m and 3 flights are carried out in this area : two flights at 30m and 90m with nadir-looking camera and one flight at 60m with oblique-looking camera. The corridor area extends for 400m's long and is

surveyed with one nadir-looking flight at 40m. Figure 7.13 and Table 7.2 gives more information about the conducted flights.

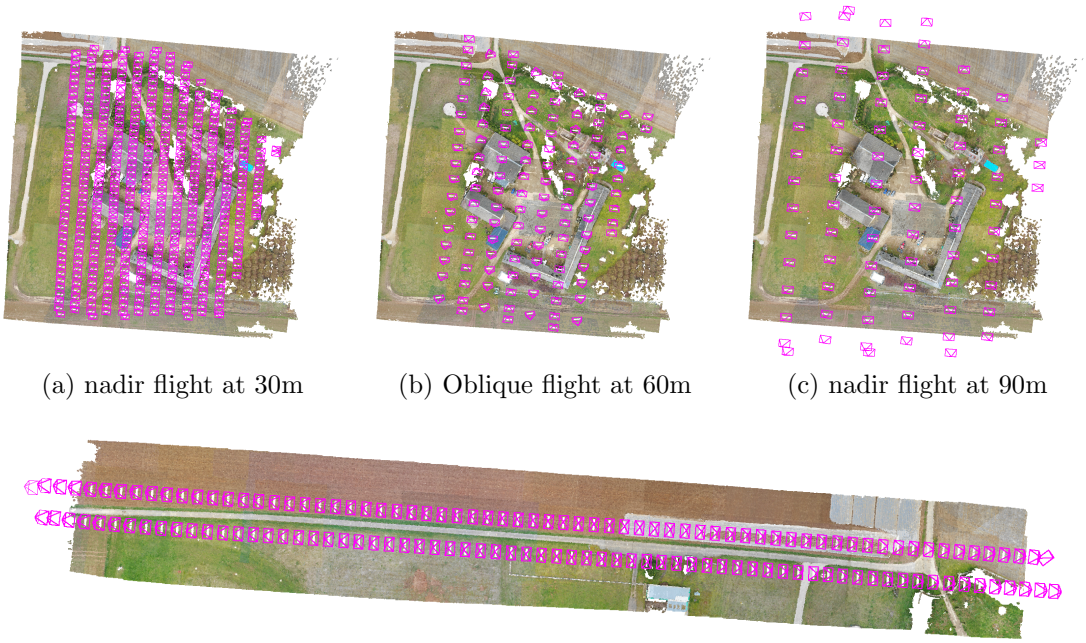

(a) nadir flight at 30m (b) Oblique flight at 60m (c) nadir flight at 90m

(d) nadir flight at 40m

Figure. 7.13 – An illustration of the conducted flights.

Flight	naidr-30m	oblique-60m	nadir-90m	nadir-40m
Nb of images	443	125	80	136
Overlap (%)		80/80		
GSD(cm)	0.74	∼1.48	2.10	0.96

Table. 7.2 – Details of conducted flights

A total of 23 ground points are surveyed with Leica 2000 receivers in D-RTK mode, 15 of which are visible in the block configuration datasets, and 11 in the corridor configuration dataset (3 points are seen by both configurations). For each configuration, the seen ground points are divided into two sets, one serves as ground control points (GCP) and the other as check points (CP). Figure 7.14 shows the distribution of GCPs and how they are divided into two sets.

7.6.2 Camera calibration model

Two camera calibration models are employed for the photogrammetric processing, each estimates 8 and 10 parameters respectively. The 8-parameter calibration model consists of

— f : the camera focal length

— PP_x, PP_y : the principal point, which is also the distortion center

— K_1, K_2, K_3 : 3 degrees of radial distortion coefficients

— P_1, P_2 : decentring distortion coefficients

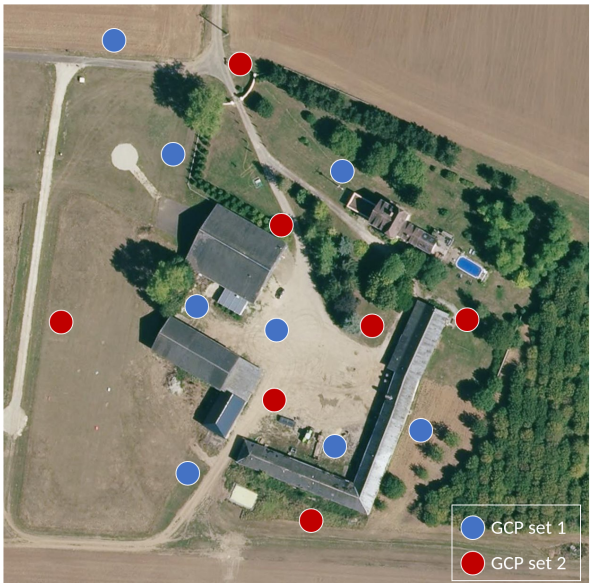

(a) block configuration

(b) corridor configuration

Figure. 7.14 – Distribution of GCPs

The 10-parameter calibration model includes in addition

— b_1, b_2 : the affine distortion coefficients

The 10-parameter camera model is actually the well-known *Fraser* camera model (Fraser [1997]). The intention of employing these 2 camera models and investigating the influence of the affine distortion coefficients b_1, b_2 is that, in the case of a flat scene as in aerial acquisitions, the rolling shutter effect may cause a similar effect to the affine distortion which is supposed to be corrected by b_1, b_2. Therefore, it is interesting to see until which point the affine distortion coefficients can correct the rolling shutter effect as well as if the proposed method can bring a further improvement.

7.6.3 Data processing

The same data processing pipeline is performed on the original and the corrected dataset. For the corrected dataset, the tie points and the image measurements are modified as explained in Section 7.5 while the rest remains unchanged with respect to the original dataset.

Firstly, a bundle block adjustment is performed with the tie points as input to recover the camera poses in a relative coordinate system. Afterwards, GCPs are used to geo-reference the 3D model and to perform a second bundle block adjustment in an absolute reference frame. It is worth noting that each time there is one set of points that participate in the bundle block adjustment as GCPs, the other set is used as CPs to evaluate the accuracy of the issued results. Then the same procedure is carried out

with GCPs and CPs being swapped. It allows to verify the consistency of the obtained results and to eliminate the occasionality of GCP distribution.

To summarize, for one dataset, the original and the corrected observations are explored ; two camera models are employed for processing ; two combinations of GCPs/CPs are used. Therefore, each dataset is processed in 8 configurations. The notation of the configurations is given in Table 7.3 :

		Original	Corrected
8-param	GCP set 1	o-8p-GCP1	c-8p-GCP1
	GCP set 2	o-8p-GCP2	c-8p-GCP2
10-param	GCP set 1	o-10p-GCP1	c-10p-GCP1
	GCP set 2	o-10p-GCP2	c-10p-GCP2

Table. 7.3 – Notation of configurations ; “o” and “c” for original and corrected observations ; “8p” and “10p” for 8-parameter and 10-parameter camera models ; “GCP1” and “GCP2” for point set 1 and 2 as GCPs.

We choose four datasets to be processed :

1. nadir-30m, block configuration
2. nadir-90m, block configuration
3. nadir-30m + nadir-90m + oblique-60m, block configuration
4. nadir-40m, corridor configuration

The comparison between (1) and (2) gives a hint on how the flight height impacts the accuracy. By comparing (1) (2) with (3), the influence of flight configuration (i.e. inclusion of oblique images and nadir images taken from different flight heights) can be investigated. The (4) allows to verify if the rolling shutter correction works as well in corridor configurations.

7.6.4 Results

The proposed method for rolling shutter effect correction is implemented in MicMac [28], a free, open-source photogrammetric software developed at IGN (French Mapping Agency) and ENSG (Ecole Nationale des Sciences Géographiques) since 2003 (Rupnik et al. [2017]). Two well-known commercial photogrammetric software, *AgiSoft MetaShape* and *Pix4D*, also have the functionality of rolling shutter correction. Therefore, the same datasets are processed with all these three software in the same configuration and the performance of the rolling shutter correction are compared and analyzed.

7.6.4.1 MicMac

It is worth bearing in mind that, a tie point reduction is performed on SIFT-extracted tie points in *MicMac* to reduce memory requirements and processing time while maintaining the tie point manifold (Martinez-Rubi [2016]). Figure 7.15 gives histograms on the multiplicity for SIFT-extracted tie points with *MicMac* before and

after the tie point reduction. One can see that the reduction procedure lowers the number of tie points as well as the percentage of tie points with poor multiplicities. Hence, the data processing requires less compute capacity and time while still offering a guaranteed performance.

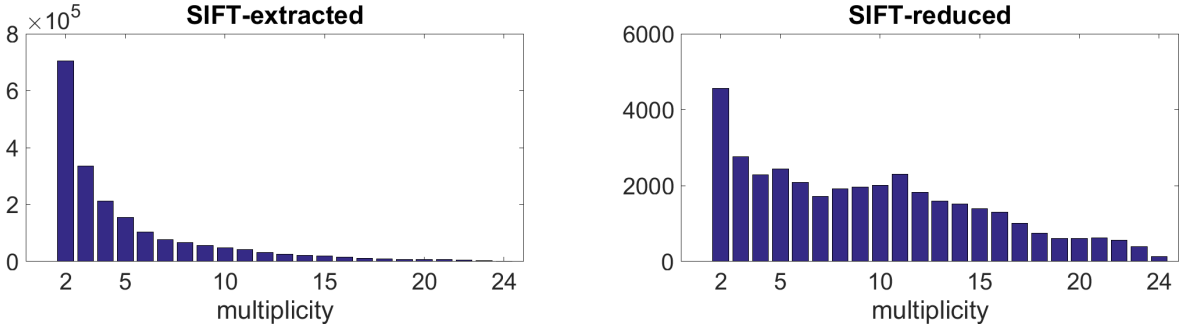

Figure. 7.15 – Histogram of tie point multiplicity before and after the tie point reduction.

The following Tables 7.4-7.7 give data processing results of the proposed approach. The results are presented with the root mean square (RMS), the mean and the unbiased standard deviation (STD) in planimetry, altimetry and 3D, respectively. The improvement after applying the rolling shutter correction is calculated based on the variation of 3D RMS. The best configuration for each dataset is highlighted in red.

Table 7.4, 7.5 : For dataset 30m-nadir and 90m-nadir in block configuration, the addition of affine distortion coefficients improves the accuracy in planimetry, especially with the original datasets. The planimetric accuracy is further improved after the rolling shutter effect correction. The best results are obtained after the correction of rolling shutter effect, both camera calibration models give comparable result with the 10-parameter model outperforming slightly the 8-parameter one. The dataset 2 (90m-nadir) gives better results compared to the dataset 1 (30m-nadir) when the rolling shutter effect is corrected, which is probably due to the fact that the results are less sensitive to the estimation error of camera velocity (due to rounded time information) with a higher surveying speed.

Table 7.6 : the dataset 3 shows similar results to dataset 1 and 2 in the cases of original datasets. In the cases where the rolling shutter effect is corrected, the inclusion of affine distortion parameters degrades the planimetric accuracy. This is probably due to the fact that, with a proper flight configuration (oblique images and nadir images taken from different flight heights) being present, the rolling shutter effect has been corrected almost entirely by the proposed method and the dataset is over-parameterized with the 10-parameter model.

Table 7.7 : the dataset 4 shows similar results to the dataset 3. However, the improvements are less significant in corridor configuration (15% - 25%) compared to in block configurations (30% - 60%). With the corridor configuration being an unfavorable flight configuration, a bowl effect is often observed and aggravates the obtained accuracy, even for cases in which no rolling shutter effect is present. Therefore, the improvement in this configuration is less significant compared to block configurations.

	Planimetry (cm)			Altimetry (cm)			3D (cm)				Planimetry (cm)			Altimetry (cm)			3D (cm)			Improvement
	RMS	Mean	STD	RMS	Mean	STD	RMS	Mean	STD		RMS	Mean	STD	RMS	Mean	STD	RMS	Mean	STD	on 3D (%)
o-8p-GCP1	10.6	9.4	5.3	6.9	-1.7	7.3	12.6	11.6	5.4	c-8p-GCP1	3.3	2.9	1.6	6.9	-1.6	7.4	7.7	6.9	3.8	38
o-8p-GCP2	14.7	12.6	8.1	10.3	-2.8	10.6	18.0	15.1	10.3	c-8p-GCP2	4.7	2.8	4.0	6.4	4.0	5.3	7.9	6.3	5.2	56
o-10p-GCP1	3.7	3.3	1.8	6.2	-1.6	6.6	7.3	6.8	2.8	c-10p-GCP1	2.5	2.2	1.3	6.9	-1.5	7.4	7.4	6.5	3.8	-1
o-10p-GCP2	6.6	5.7	3.6	10.0	-2.7	10.3	12.0	9.4	7.9	c-10p-GCP2	4.1	2.7	3.3	6.3	4.0	5.2	7.6	6.1	4.8	36

Table. 7.4 – *MicMac* - Results for dataset 1 : 30m-nadir.

	Planimetry (cm)			Altimetry (cm)			3D (cm)				Planimetry (cm)			Altimetry (cm)			3D (cm)			Improvement
	RMS	Mean	STD	RMS	Mean	STD	RMS	Mean	STD		RMS	Mean	STD	RMS	Mean	STD	RMS	Mean	STD	on 3D (%)
o-8p-GCP1	14.1	12.8	6.4	4.0	-1.6	4.0	14.6	13.5	6.1	c-8p-GCP1	3.1	2.5	1.9	4.9	0.4	5.3	5.8	4.9	3.4	60
o-8p-GCP2	13.9	12.5	6.4	5.2	-0.3	5.6	14.8	13.5	6.6	c-8p-GCP2	2.8	1.8	2.2	4.8	-1.0	5.0	5.6	3.9	4.3	62
o-10p-GCP1	6.3	5.9	2.5	4.0	-1.2	4.1	7.5	7.1	2.5	c-10p-GCP1	1.9	1.5	1.1	4.9	0.4	5.2	5.2	4.2	3.3	30
o-10p-GCP2	7.8	6.6	4.3	5.8	-0.1	6.2	9.7	8.3	5.3	c-10p-GCP2	2.0	1.5	1.5	4.7	-1.1	4.9	5.1	3.7	3.8	47

Table. 7.5 – *MicMac* - Results for dataset 2 : 90m-naidr.

	Planimetry (cm)			Altimetry (cm)			3D (cm)				Planimetry (cm)			Altimetry (cm)			3D (cm)			Improvement
	RMS	Mean	STD	RMS	Mean	STD	RMS	Mean	STD		RMS	Mean	STD	RMS	Mean	STD	RMS	Mean	STD	on 3D (%)
o-8p-GCP1	14.0	12.8	6.1	3.2	0.0	3.5	14.4	13.3	5.9	c-8p-GCP1	4.1	3.7	1.9	2.4	1.6	1.9	4.8	4.4	1.9	66
o-8p-GCP2	13.3	11.9	6.1	3.0	-0.3	3.2	13.6	12.6	5.6	c-8p-GCP2	4.4	3.1	3.4	2.2	-1.9	1.1	5.0	4.1	3.0	63
o-10p-GCP1	9.0	8.1	4.2	3.4	0.0	3.6	9.6	8.9	3.9	c-10p-GCP1	5.8	5.0	3.2	2.3	1.5	1.9	6.3	5.7	2.8	34
o-10p-GCP2	8.7	7.5	4.6	3.1	-0.2	3.3	9.3	8.4	4.1	c-10p-GCP2	5.9	4.1	4.5	2.1	-1.9	1.1	6.3	4.9	4.2	32

Table. 7.6 – *MicMac* - Results for dataset 3 : 30m-nadir + 60m-oblique + 90m-nadir.

	Planimetry (cm)			Altimetry (cm)			3D (cm)				Planimetry (cm)			Altimetry (cm)			3D (cm)			Improvement
	RMS	Mean	STD	RMS	Mean	STD	RMS	Mean	STD		RMS	Mean	STD	RMS	Mean	STD	RMS	Mean	STD	on 3D (%)
o-8p-GCP1	6.4	5.2	4.2	8.1	-2.9	8.3	10.4	8.7	6.2	c-8p-GCP1	5.3	4.0	3.8	5.9	-1.8	6.2	8.0	6.6	4.9	23
o-8p-GCP2	6.4	4.7	4.9	11.7	6.0	11.3	13.4	8.4	11.7	c-8p-GCP2	1.6	1.5	0.8	9.9	4.4	9.8	10.0	6.0	8.9	25
o-10p-GCP1	5.3	4.3	3.3	7.7	-2.8	7.8	9.4	7.8	5.6	c-10p-GCP1	5.1	4.1	3.4	6.3	-1.9	6.6	8.1	6.9	4.6	14
o-10p-GCP2	5.0	3.7	3.8	11.5	5.8	11.1	12.6	7.6	11.2	c-10p-GCP2	3.2	2.8	1.7	10.0	4.6	9.9	10.5	6.5	9.2	17

Table. 7.7 – *MicMac* - Results for dataset 4 : 40m-nadir.

7.6.4.2 AgiSoft MetaShape

There is not much information on how the rolling shutter correction is implemented in *AgiSoft MetaShape*. What is known is that the software gives information on rotational and translational velocity for every image. However, it is not clear if the parameters are estimated during the bundle block adjustment or calculated *a posteriori*.

Table 7.8, 7.9 : in the case where no rolling shutter correction is performed, the inclusion of affine distortion coefficients improves substantially the planimetric accuracy. The correction of rolling shutter effect does improve the results when processed with the 8-parameter camera model ; the error on planimetry is reduced considerably whereas on altimetry the error increases slightly. The best results are obtained in the cases where the original datasets are processed with the 10-parameter camera model, whereas the correction of rolling shutter effect degrades the accuracy.

Table 7.10 : With a proper flight configuration, the correction of rolling shutter effect improves significantly the obtained accuracy for both camera models. The 10-parameter camera model achieves an accuracy slightly better then that of the 8-parameter camera model.

Table 7.11 : When processing the datasets without the rolling shutter correction, the obtained accuracy is satisfying. However, the rolling shutter correction encounters difficulties when it comes to corridor configuration ; the accuracy degrades drastically, mostly in altimetry.

7.6.4.3 Pix4D

In Vautherin et al. [2016] it is shown that a linear motion assumption is made. The motion velocity is described with a 6-parameter model $[\Delta R_x, \Delta R_y, \Delta R_z, \Delta T_x, \Delta T_y, \Delta T_z]$. There is one thing to point out : in *Pix4D* solely the 8-parameter camera calibration model is supported. Therefore, only 4 configurations concerning the 8-parameter camera model are conducted.

Table 7.12, 7.13, 7.14 : all three datasets show significant increases on accuracy after applying the rolling shutter correction. With no rolling shutter correction, the dataset 90m-nadir gives the lowest accuracy among the three block configuration datasets. By applying the correction, the dataset 30-nadir sees the least improvement and gives the lowest accuracy.

Table 7.15 : similar to *AgiSoft MetaShape*, the rolling shutter correction does not work as expected for corridor configuration dataset. The unfavorable flight configuration makes it difficult to estimate 14 camera calibration parameters per image.

	Planimetry (cm)			Altimetry (cm)			3D (cm)				Planimetry (cm)			Altimetry (cm)			3D (cm)			Improvement
	RMS	Mean	STD	RMS	Mean	STD	RMS	Mean	STD		RMS	Mean	STD	RMS	Mean	STD	RMS	Mean	STD	on 3D (%)
o-8p-GCP1	10.5	9.7	4.5	3.2	0.4	3.4	11.5	10.4	5.5	c-8p-GCP1	0.5	0.4	0.2	7.4	-3.4	7.2	7.6	4.6	6.7	33
o-8p-GCP2	8.3	8.2	4.7	15.4	-0.4	16.4	19.8	17.2	7.2	c-8p-GCP2	0.2	0.2	0.1	8.1	3.7	7.7	8.4	6.3	6.3	57
o-10p-GCP1	1.2	1.2	0.4	2.5	0.4	2.7	2.8	2.4	1.6	c-10p-GCP1	1.8	1.4	1.2	6.9	-3.1	6.8	7.2	4.2	6.4	-157
o-10p-GCP2	3.5	3.0	1.8	3.2	0.8	3.3	4.8	4.1	2.5	c-10p-GCP2	2.2	2.1	1.2	8.2	3.8	7.9	8.5	6.5	6.4	-77

Table. 7.8 – *MetaShape* - Results for dataset 1 : 30m-nadir.

	Planimetry (cm)			Altimetry (cm)			3D (cm)				Planimetry (cm)			Altimetry (cm)			3D (cm)			Improvement
	RMS	Mean	STD	RMS	Mean	STD	RMS	Mean	STD		RMS	Mean	STD	RMS	Mean	STD	RMS	Mean	STD	on 3D (%)
o-8p-GCP1	15.3	13.3	8.1	3.5	1.0	3.6	15.7	13.9	7.9	c-8p-GCP1	2.6	2.1	1.6	4.9	-0.2	5.3	5.6	4.2	3.9	64
o-8p-GCP2	14.8	11.2	7.4	8.0	0.4	7.9	16.9	11.5	9.5	c-8p-GCP2	2.1	1.5	1.2	13.9	0.3	14.1	14.0	7.4	10.0	17
o-10p-GCP1	4.8	4.4	2.0	2.4	0.7	2.5	5.4	5.1	1.6	c-10p-GCP1	3.2	2.6	2.0	7.0	1.3	7.4	7.7	5.6	5.7	-42
o-10p-GCP2	6.0	4.1	3.3	5.4	-1.5	5.8	8.1	4.6	5.3	c-10p-GCP2	2.9	2.0	1.7	14.9	-0.3	15.5	15.2	9.0	10.2	-87

Table. 7.9 – *MetaShape* - Results for dataset 2 : 90m-naidr

	Planimetry (cm)			Altimetry (cm)			3D (cm)				Planimetry (cm)			Altimetry (cm)			3D (cm)			Improvement
	RMS	Mean	STD	RMS	Mean	STD	RMS	Mean	STD		RMS	Mean	STD	RMS	Mean	STD	RMS	Mean	STD	on 3D (%)
o-8p-GCP1	14.7	13.3	6.6	4.1	-1.5	4.2	15.2	13.9	6.6	c-8p-GCP1	2.2	1.9	1.1	1.5	-1.0	1.2	2.6	2.4	1.1	82
o-8p-GCP2	13.4	11.0	6.0	3.6	2.0	3.0	13.9	11.8	5.3	c-8p-GCP2	2.8	1.8	1.8	2.4	0.7	2.4	3.7	3.0	1.7	73
o-10p-GCP1	8.7	7.9	4.1	4.4	-1.2	4.6	9.8	9.0	4.1	c-10p-GCP1	2.0	1.8	0.9	1.5	-1.0	1.3	2.5	2.4	1.0	74
o-10p-GCP2	7.7	5.2	4.4	3.3	1.6	3.0	8.4	6.4	3.8	c-10p-GCP2	2.3	1.4	1.6	2.5	0.7	2.6	3.4	2.9	1.6	59

Table. 7.10 – *MetaShape* - Results for dataset 3 : 30m-nadir + 60m-oblique + 90m-nadir.

	Planimetry (cm)			Altimetry (cm)			3D (cm)				Planimetry (cm)			Altimetry (cm)			3D (cm)			Improvement
	RMS	Mean	STD	RMS	Mean	STD	RMS	Mean	STD		RMS	Mean	STD	RMS	Mean	STD	RMS	Mean	STD	on 3D (%)
o-8p-GCP1	5.7	4.1	4.4	4.7	1.4	4.9	7.4	5.6	5.4	c-8p-GCP1	10.6	7.5	8.2	14.2	7.5	13.2	17.7	14.8	10.7	-139
o-8p-GCP2	5.9	4.1	4.7	5.1	-1.8	5.4	7.8	5.2	6.5	c-8p-GCP2	8.3	7.7	3.3	45.0	-22.0	43.9	45.8	30.5	38.1	-487
o-10p-GCP1	4.5	3.1	3.6	4.4	1.1	4.6	6.3	4.7	4.6	c-10p-GCP1	17.1	10.9	14.4	56.8	6.7	61.8	59.3	47.0	39.7	-841
o-10p-GCP2	4.8	3.3	3.8	5.3	-1.8	5.6	7.1	4.7	6.0	c-10p-GCP2	31.9	29.7	13.2	91.2	-41.7	90.7	96.6	70.3	74.1	-1261

Table. 7.11 – *MetaShape* - Results for dataset 4 : 40m-nadir.

	Planimetry (cm)			Altimetry (cm)			3D (cm)				Planimetry (cm)			Altimetry (cm)			3D (cm)			Improvement
	RMS	Mean	STD	RMS	Mean	STD	RMS	Mean	STD		RMS	Mean	STD	RMS	Mean	STD	RMS	Mean	STD	on 3D (%)
o-8p-GCP1	11.1	10.1	4.6	1.9	-0.5	1.8	11.2	10.2	4.7	c-8p-GCP1	0.8	0.8	0.3	4.8	-0.4	4.7	4.8	3.7	3.1	57
o-8p-GCP2	15.7	13.7	7.7	2.3	0.9	2.1	15.8	13.9	7.6	c-8p-GCP2	2.1	1.8	1.0	5.6	2.7	4.9	6.0	5.0	3.2	62

Table. 7.12 – *Pix4D* - Results for dataset 1 : nadir-30m.

	Planimetry (cm)			Altimetry (cm)			3D (cm)				Planimetry (cm)			Altimetry (cm)			3D (cm)			Improvement
	RMS	Mean	STD	RMS	Mean	STD	RMS	Mean	STD		RMS	Mean	STD	RMS	Mean	STD	RMS	Mean	STD	on 3D (%)
o-8p-GCP1	16.0	13.0	9.4	7.0	-4.8	5.1	17.4	14.6	9.5	c-8p-GCP1	1.1	1.0	0.5	2.6	-0.1	2.6	2.8	2.5	1.3	83
o-8p-GCP2	16.3	13.8	8.6	7.4	3.2	6.7	17.9	15.6	8.8	c-8p-GCP2	1.1	1.1	0.4	1.4	0.3	1.3	1.8	1.6	0.8	89

Table. 7.13 – *Pix4D* - Results for dataset 2 : nadir-90m.

	Planimetry (cm)			Altimetry (cm)			3D (cm)				Planimetry (cm)			Altimetry (cm)			3D (cm)			Improvement
	RMS	Mean	STD	RMS	Mean	STD	RMS	Mean	STD		RMS	Mean	STD	RMS	Mean	STD	RMS	Mean	STD	on 3D (%)
o-8p-GCP1	14.6	13.1	6.5	2.4	0.9	2.3	14.8	13.3	6.4	c-8p-GCP1	1.5	1.3	0.7	1.2	0.5	1.1	1.9	1.7	0.8	87
o-8p-GCP2	13.4	12.1	5.9	3.3	-2.1	2.6	13.8	12.6	5.6	c-8p-GCP2	1.5	1.4	0.7	1.7	-0.8	1.5	2.3	1.8	1.4	83

Table. 7.14 – *Pix4D* - Results for dataset 3 : 30m-nadir + 60m-oblique + 90m-nadir.

	Planimetry (cm)			Altimetry (cm)			3D (cm)				Planimetry (cm)			Altimetry (cm)			3D (cm)			Improvement
	RMS	Mean	STD	RMS	Mean	STD	RMS	Mean	STD		RMS	Mean	STD	RMS	Mean	STD	RMS	Mean	STD	on 3D (%)
o-8p-GCP1	5.9	3.7	4.6	22.2	11.1	19.2	22.9	14.3	18.0	c-8p-GCP1	62.6	37.7	50.0	38.1	10.8	36.5	73.3	52.0	51.6	-220
o-8p-GCP2	5.9	4.1	4.3	2.7	1.7	2.1	6.5	3.2	5.7	c-8p-GCP2	11.9	9.7	7.0	33.4	7.5	32.5	35.4	8.3	34.4	-444

Table. 7.15 – *Pix4D* - Results for dataset 4 : 40m-nadir.

7.6.4.4 Comparison of results

For each dataset, the results issued from the three software are assembled for comparison purpose and are presented in Figure 7.16 - 7.19.

Figure 7.16 : For all three software, the rolling shutter correction is able to improve the obtained accuracy when processed with the 8-parameter camera calibration model. The three software give comparable results with *Pix4D* being slightly on top. When employing the 10-parameter camera model, the rolling shutter correction of *MetaShape* worsens the results, which is probably due to over-parameterization. On the contrary, the proposed method implemented in *MicMac* still works in this case and gives similar results to cases with the 8-parameter model.

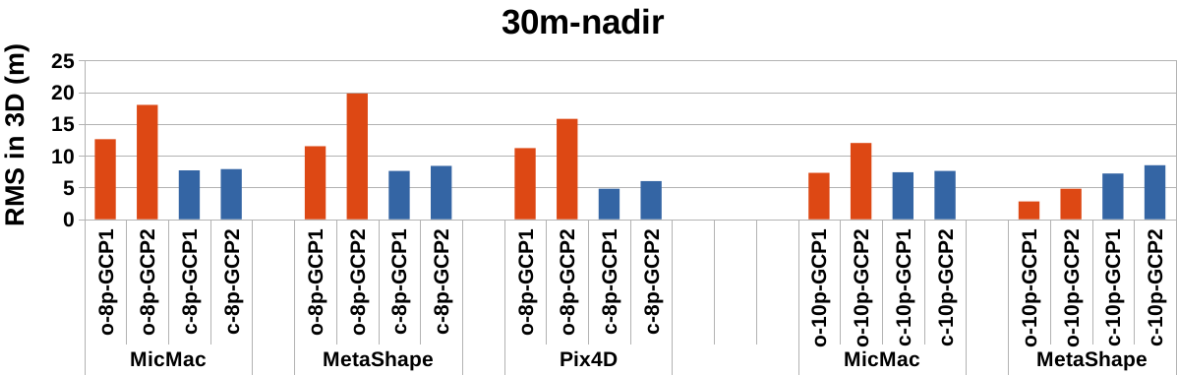

Figure. 7.16 – Result comparison of dataset 1 : 30m-nadir

Figure 7.17 : A similar trend to Figure 7.16 is observed. What is worth noting is that, unlike the dataset 30m-nadir, for 90m-nadir, *MetaShape* seems to encounter difficulties with the configuration c-8p-GCP2 and is not able to reach the same accuracy as other two software.

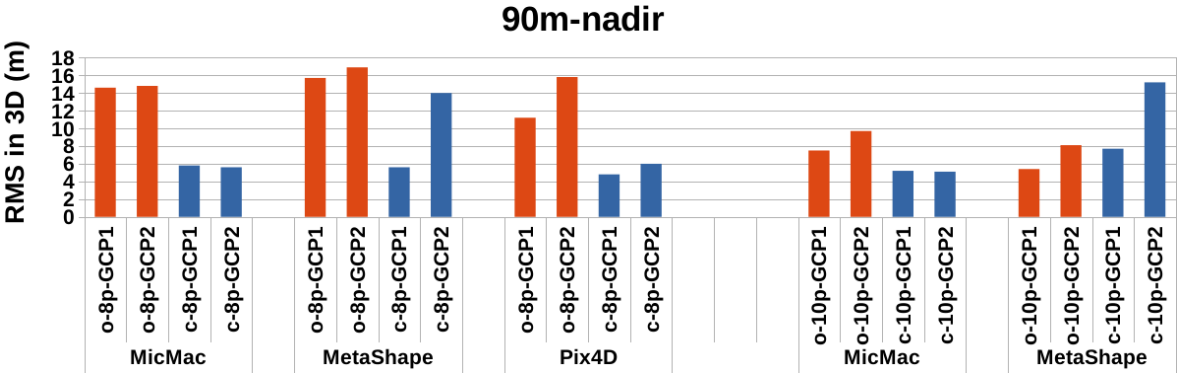

Figure. 7.17 – Result comparison of dataset 2 : 90m-nadir

Figure 7.18 : With a good flight configuration being presented, all three software are able to correct the rolling shutter effect as expected. Since the proposed is implemented based on a coarse velocity estimation (the time related information is rounded to second), it shows less satisfying results for corrected datasets compared to the other two software.

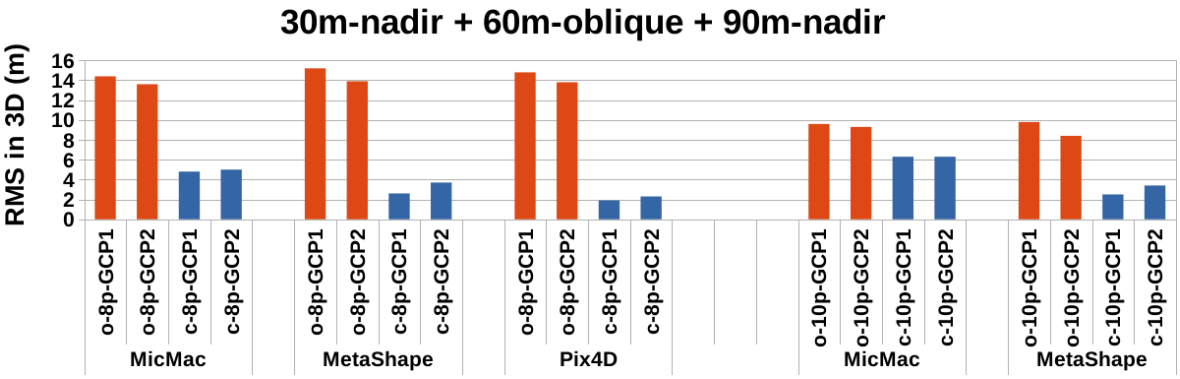

Figure. 7.18 – Result comparison of dataset 3 : 30m-nadir + 60m-oblique + 90m-nadir

Figure 7.19 : When it comes to the unfavorable corridor configuration, only the proposed method implemented in *MicMac* is able to correct the rolling shutter effect and to improve the accuracy. The other two software all give degraded accuracy after applying the correction. The poor flight configuration makes it more difficult to estimate extra parameters in bundle block adjustment.

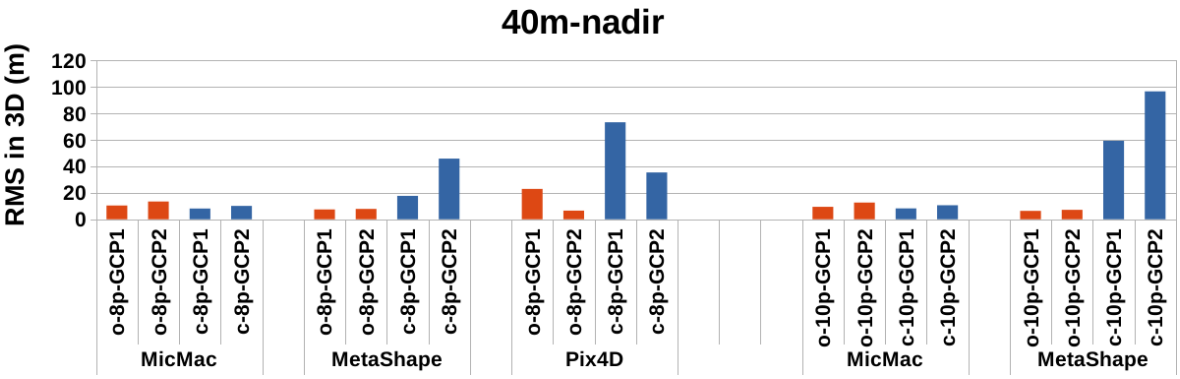

Figure. 7.19 – Result comparison of dataset 4 : 40m-nadir

7.7 Conclusion and perspective

In this paper, the rolling shutter effect in aerial photogrammetry is addressed. We proposed two approaches to calibrate the readout time of rolling shutter cameras as well as a two-step method for the rolling shutter effect correction. The approach of readout time calibration gives the possibility to have control on this information which is often not given by the camera manufacturer. It as well allows the correction of image deformation introduced by this effect. The rolling shutter effect correction is implemented in *MicMac*, a free, open-source photogrammetric software.

The proposed rolling shutter correction method performs under the assumption that the deformation due to camera orientation change is negligible compared to that of camera position change. In our case, the datasets are acquired with a camera which is alleged to provide a stable, smooth footage for image acquisition thanks to a 3-axis gimbal, which conforms this assumption. However, the time related information registered in the image metadata is rounded to second, which can limit the performance

of the presented method. Despite this, with a consumer-grade drone/camera and the provided information in metadata, the approach presented in this article is able to improve the accuracy of photogrammetric results with a robust performance.

Four datasets are processed, two nadir-looking block configuration datasets at a flight height of 30m and 90m, respectively ; one block configuration dataset consisting of the two first datasets and one oblique-looking dataset at 60m ; and one corridor configuration dataset conducted at 40m. Each dataset is processed with two camera calibration models : a 8-parameter model and a 10-parameter model which has two affine distortion coefficients in addition. The ground points are separated into two sets to serve as GCPs and CPs ; each dataset is processed twice with the 2 point sets as GCPs to eliminate the occasionality. The proposed method improves the accuracy by 30%-60% for block configuration and 15%-25% for corridor configuration. Comparison is conducted with other two commercial software, *AgiSoft MetaShape* and *Pix4D*.

Several conclusions can be drawn. To begin with, the inclusion of affine distortion coefficients improves the results when the rolling shutter effect is present. It is comprehensive since the deformation introduced by rolling shutter effect can be similar to an affine distortion on a flat scene. *Pix4D* only supports the 8-parameter camera calibration model, no further studies can be carried out. For *AgiSoft MetaShape*, when applying a rolling shutter effect correction, it is recommended not to include the affine distortion coefficients since there is a risk of over-parameterization. The proposed method works with both camera models without the risk of over-parameterization and gives comparable results to other two software.

Secondly, the flight configuration is an essential factor for rolling shutter correction in *AgiSoft MetaShape* and *Pix4D*. For each image, several parameters in addition are estimated during the bundle block adjustment to describe the change of camera pose during acquisition. When a favorable block configuration is presented, such as for instance, nadir images of different flight heights as well as oblique images, both software turn out to work fine. For a less favorable configuration where there is only nadir images with one single flight height, the performance of the rolling shutter correction degrades. In certain cases, *AgiSoft MetaShape* even shows reduced accuracy after applying the correction. For corridor configuration, none of these two software works as expected. On the contrary, the method proposed in this paper is robust to the flight configuration. To correct the deformation in image space, the estimation of the camera velocity during exposure is carried out after the bundle block adjustment, therefore does not have specific requirements on the flight configuration. It is the only method that works for both block and corridor configuration datasets.

Though the method proposed in this article gives satisfying results in all configurations, in the case where a good flight configuration is present (oblique and nadir images of different flight heights), the other two methods which estimate the camera pose variation show better performance. It is partly due to the compromised time related information explored for camera velocity estimation in this two-step method. A further improvement is expected if an accurate timestamp is provided in the metadata or if the camera positions are directly available with the aid of for example GNSS data. Moreover, the assumption of the camera orientation variation being negligible compared to the camera position change can slightly degrade the performance of the proposed method. Future studies should be carried out on the exploration of gimbal

data, and how it can be used to estimate the camera orientation change and to perform a complete correction of rolling shutter effect.

Chapter 8

Conclusion and Perspective

During the past decades, UAV platforms has been undergoing unprecedented evolutions thanks to the development of on-board sensors, embedded navigation systems and automatic data processing solutions. They have nowadays become a valuable source of data for inspection, surveillance, mapping and 3D modeling issues (Nex and Remondino [2014]). UAV photogrammetry turns out to be an interesting low-cost alternative to classical manned aerial photogrammetry (Colomina and de la Tecnologia [2008]; Eisenbeiß [2009]).

This thesis is a research project initiated by the CNR, a river concessionary, which is responsible for the maintenance and the surveillance of its hydraulic facilities, more precisely, the dikes. The conducted works tackled the problem of corridor mapping, one field of substantial importance in UAV photogrammetry. The objective of the CNR was to obtain a 3D dense reconstruction of the dike with UAV photogrammetry. To reach a good mapping accuracy, it is crucial to well estimate camera poses, which is what we seeked for in this thesis work. Previous thesis works showed that with consumer grade materials and refined camera calibration, a centimetric accuracy was achieved with one GCP per 100 m on a corridor configuration scene (Tournadre [2015]). Basing on previous research results, we look for a solution which, while maintaining a high accuracy for corridor mapping, requires a reduced field work, i.e. the number of ground control points (GCPs).

Firstly, simulations are carried out on three issues that interested us. The generated synthetic dataset of corridor configuration gave us the possibility to focus on the problem of interest without the perturbation coming from other issues. The first focus was given to the error on focal length when pre-calibrating the camera. The height of the camera tended to drift to compensate for the erroneous focal length, while the presence of oblique images limited this drift and led to more accurate camera pose estimations. The second problem that had been addressed was the variation of focal length due to camera temperature change. When only nadir images were present, a variation of 1 pixel on the focal length decreased the 3D accuracy by 1 cm. The inclusion of oblique images brought a significant improvement and was a easy, efficient solution to the problem. It is more recommanded to perform oblique flight before nadir ones. The last addressed issue was the rolling shutter effect. The simulations showed that the influence of camera rotational motion was negligible compared to camera translational

motion, and could be easily eliminated with the inclusion of more flight strips. No one flight configuration gave better results than the others. To eliminate the degradation introduced by the rolling shutter effect, corrections on image measurements could be one efficient solution.

After the simulation, three aspects had been investigated thoroughly with real-case UAV datasets. We firstly tackled the aerial acquisition geometry for a corridor dataset of 1200 m. The first half of 600 m was surveyed with oblique-looking flight and multi-height nadir-looking flights. Compared to a routine flight configuration of single-height nadir-looking flight, the proposed flight configuration lowered the correlation between camera focal length, camera height and lever-arm and led to satisfying results. With no GCP, an accuracy of 6-8 cm was achieved ; by adding 1 GCP in the middle of the scene, the accuracy was improved up to 1 cm. The in-flight camera calibration and lever-arm calibration were performed with the proposed flight configuration and 14 GCPs, then the calibration results were given to the second half of 600 m surveyed with routine flight configuration, i.e. single-height nadir-looking flight. Without the aid of GCPs, the application of pre-calibrations improved the accuracy from 15 cm to 4 cm. The addition of 1 GCP did not bring significant improvements when pre-calibrations were performed. The accuracy of the proposed acquisition geometry met the needs and expectations of the CNR. For regular surveillance of the dike, the combination of oblique and nadir images plus embedded GNSS and 1 GCP allowed for an accuracy of 1 cm. For exceptional events, an accuracy of 4 cm was achieved with a simple single-height nadir-looking flight and instrument pre-calibration, no GCP was required.

The focus was then given on high-end metric cameras and the image deformation introduced by camera temperature change. During aerial acquisitions the frame-rate of the camera can be quite high, which leads to an increase of camera temperature. This temperature change causes the internal parameters to change and degrades the accuracy of photogrammetric products if not being taken into account. Two independent techniques were exploited to study the camera's response to temperature change. The camera employed for investigation was the lightweight metric camera developed at IGN. The camera temperature change was proved to be the main cause of the variation of internal parameters and similar trends were observed with the two techniques. A good repeatability over time was observed for the focal length variation (0.4 - 0.5 µm/°C for a 35 mm). A polynomial correction of the thermal effect was then proposed and the performance was evaluated with both terrestrial and aerial datasets of corridor configuration. The terrestrial dataset showed that the *bowl effect* was reduced by a factor of 3.6 after applying the thermal effect correction. For the aerial dataset of corridor configuration, an accuracy gain of 1.4 times was observed. In a nutshell, high-end metric cameras offers a good stability of camera internal parameters over time, the correction of thermal deformation ensures its stability over temperature change and improves furthermore the mapping accuracy.

The last study tackled with consumer-grade cameras of rolling shutter. The fact that UAV is not static during image acquisition and the image is acquired line by line with rolling shutter camera, introduces a non negligible image deformation and degrades substantially the mapping accuracy. The UAV plateform employed for the study was the DJI Mavic 2 Pro, of which the embedded camera was equipped with a rolling shutter. Two methods were proposed to calibrate the readout time of the camera, offering a control on this information that is rarely given by camera manufacturers.

A two-step approach of rolling shutter correction was proposed and implemented in the free, open-source software *MicMac*. Its performance was evaluated on aerial datasets of block and corridor configurations, comparisons were carried out with other two commercial software, *Pix4D* and *AgiSoft MetaShape*. Several conclusions were drawn according to conducted experiments. First of all, when processing with *MicMac*, the inclusion of affine distortion coefficients improved the accuracy, which was comprehensive since the deformation introduced by rolling shutter effect is similar to an affine distortion on a flat scene. For *AgiSoft MetaShape*, since the rolling shutter correction was performed by adding parameters describing camera motion, the inclusion of affine distortion coefficients increased the risk of over-parameterization. Furthermore, the flight configuration appeared to be an essential factor for rolling shutter correction in *Pix4D* and *AgiSoft MetaShape*. Better results were obtained when multi-height nadir-looking flights or oblique-looking flights were present. In corridor configuration, both commercial software showed degraded results after applying the rolling shutter correction. One the contrary, the two-step approach we proposed was robust to flight configuration, and was the only approach that showed its effectiveness in corridor configuration. An accuracy improvement of 30%-60% and 15%-25% were observed for block and corridor configuration, respectively.

Further studies should be carried out on several aspects. For the modeling of camera's response to temperature variation, a good reproducibility was observed on the focal length. However, the long-term stability of camera's response should be further investigated. If a thermal calibration is required on a regular basis, the proposed calibration method is simple to implement and fully automated. In this experience, only the lightweight metric camera of `IGN` was studied. Experiences should be carried out with different image sensors for the study of a large scope.

After that, the performance of the proposed two-step rolling shutter correction was partly compromised. The timestamp was rounded to second and led to a rough camera pose estimation. Further experiments should be taken if an accurate timestamp is available or the camera velocity and position information is provided by embedded navigation system. Moreover, the two-step approach took the assumption that camera rotational motion introduced negligible influence compared to camera translational motion. Future studies should be carried out on the exploration of camera orientation information, a complete correction taking into account both translational and rotational motions can be expected.

To summarize, the conclusions of this thesis work were drawn based on limited datasets. The experiments were carried out in laboratory with adaptive hardware and software. Great efforts were given to the processing without taking into account the labor cost and the time cost. Prior to a complete industrial adoption of this thesis work, extensive experiments and further investigations should be carried out to meet respective requirements on cost, feasibility and repeatability.

Annexe A

GNSS processing with RTKLib

Convert GNSS observation

Sometimes, GNSS observation is stored in binary format and need to be converted for further processing. Normally, we choose to convert it to `Receiver Independent Exchange Format` (`RINEX`), a data interchange format for raw satellite navigation system. The AP `RTKConv` of `RTKLib` is one of the tools. Here the GUI version of the AP is introduced (cf. Figure. A.1).

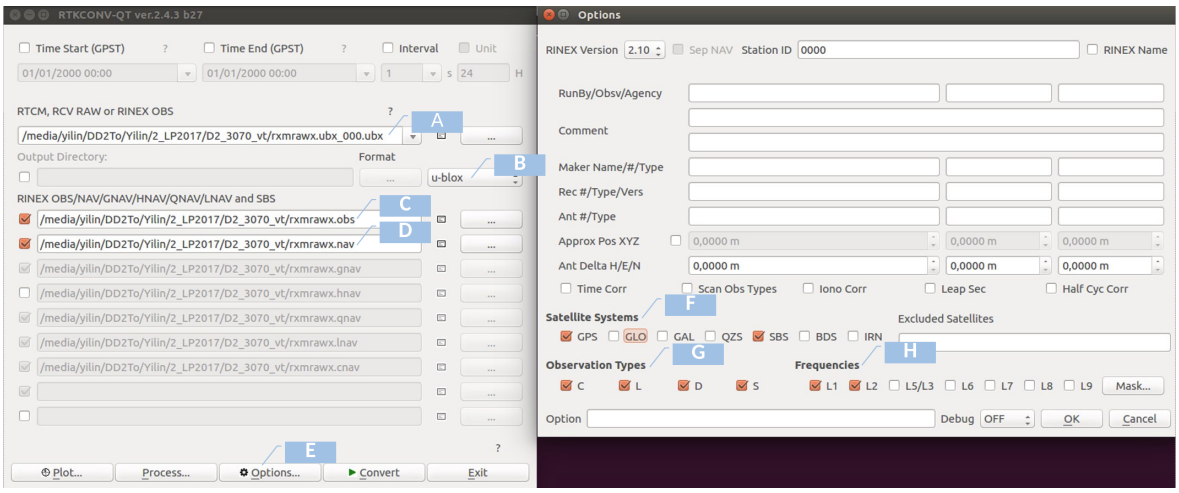

Figure. A.1 – GUI of `RTKConv`

- field A : file path of GNSS raw observation
- field B : format of GNSS raw observation
- feild C : target path of GNSS observation file in `RINEX`
- field D : target path of GNSS navigation file in `RINEX`
- field E : go to `Options` tab
- field F : Satellite System, depending on receiver antenna
- field G : Observation Type, C : code, L : phase, D : Doppler, S : SNR
- field H : Observation frequency

Visualize GNSS observation

Before processing the GNSS position solution, it is a good idea to look at the data first and make sure it is complete, of reasonable quality, and at the right sample rate. The AP `RTKPlot` of `RTKLib` is one of the tools. Here the GUI version of the AP is introduced (cf. Figure. A.2).

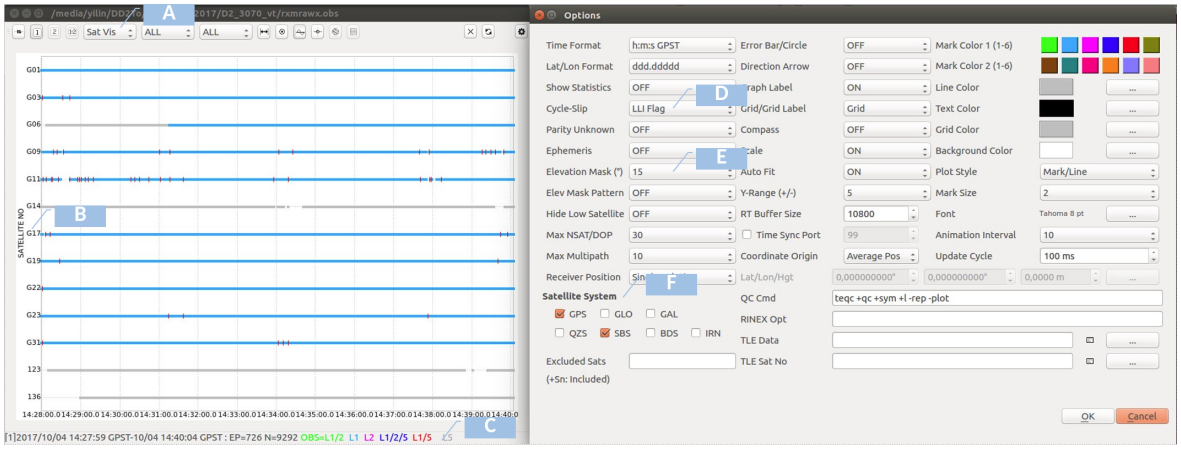

Figure. A.2 – GUI of `RTKPlot`

- field A : visualization mode
- field B : satellite identifier (PRN)
- feild C : general information of observation data
- field D : when in "LLI Flag" mode, red ticks on the signal indicate cycle slips. Too many of these will make it difficult to get a decent solution. Gaps in the data usually indicate the receiver lost lock and these are not good unless they are in the low elevation satellites.
- field E : elevation mask
- field F : Satellite System to visualize

Compute the position solution

To get more accurate solution, the computation is conducted in relative mode. It means, instead of calculating the absolute position of the GNSS antenna, the vector seperating the antenna of unknown position and one or more reference stations is estimated. If one station of permenant GNSS network is near the survey field, it can be used as the reference station. Files and information required for computation are accessible online. One can also install a GNSS station near the field temporarily and perform the calculation by himself.

To compute the GNSS position solution in static mode, the online service of `IGN` is a handy, automated tool. Details can be find on http://rgp.ign.fr/SERVICES/calcul_online.php.

To compute the GNSS position solution in kinematic mode (e.g. UAV trajectory), the AP `RTKPost` of `RTKLib` is one of the tools. Numerous parameters need to be configured, to better explain the processing procedure, the CUI version is presented.

```
$ rtkpost "rover_observation_file" "base_observation_file"
    "navigation_file" -o "output_file" -k "configuration_file"
```

An example of the default configuration file is given in Annexe B. An explanation is given for main parameters.

Visualize the position solution

Once the position solution is computed, one can visualize the result with `RTKPlot`. In Figure. A.3, two visual mode are presented. The one on the left shows the vertical view of the computed trajectory, the one on the right gives position information on three axis. On the bottom of the window, general informations are given, such as : acquisition time, number of observations, baseline length, percentage of *fix* and *float* solutions.

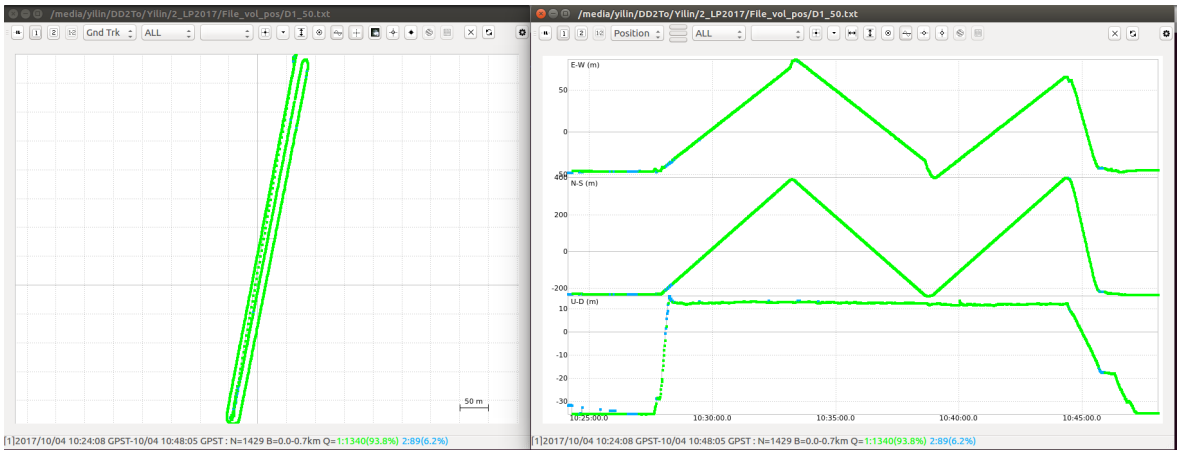

Figure. A.3 – Use `RTKPlot` to visualize final solutions.

Annexe B

An example of the RTKLib configuration file

```
pos1-posmode      =single    #
    (0:single,1:dgps,2:kinematic,3:static,4:movingbase,5:fixed,6:ppp-kine,
   7:ppp-static,8:ppp-fixed)
pos1-frequency    =l1+l2     # (1:l1,2:l1+l2,3:l1+l2+l5,4:l1+l5)
pos1-soltype      =forward   # (0:forward,1:backward,2:combined)
pos1-elmask       =15        # (deg)
pos1-snrmask_r    =off       # (0:off,1:on)
pos1-snrmask_b    =off       # (0:off,1:on)
pos1-snrmask_L1   =0,0,0,0,0,0,0,0,0
pos1-snrmask_L2   =0,0,0,0,0,0,0,0,0
pos1-snrmask_L5   =0,0,0,0,0,0,0,0,0
pos1-dynamics     =off       # (0:off,1:on)
pos1-tidecorr     =off       # (0:off,1:on,2:otl)
pos1-ionoopt      =brdc      #
    (0:off,1:brdc,2:sbas,3:dual-freq,4:est-stec,5:ionex-tec,6:qzs-brdc,7:qzs-lex,8:stec)
pos1-tropopt      =saas      #
    (0:off,1:saas,2:sbas,3:est-ztd,4:est-ztdgrad,5:ztd)
pos1-sateph       =brdc      #
    (0:brdc,1:precise,2:brdc+sbas,3:brdc+ssrapc,4:brdc+ssrcom)
pos1-posopt1      =off       # (0:off,1:on)
pos1-posopt2      =off       # (0:off,1:on)
pos1-posopt3      =off       # (0:off,1:on,2:precise)
pos1-posopt4      =off       # (0:off,1:on)
pos1-posopt5      =off       # (0:off,1:on)
pos1-posopt6      =off       # (0:off,1:on)
pos1-exclsats     =          # (prn ...)
pos1-navsys       =1         # (1:gps+2:sbas+4:glo+8:gal+16:qzs+32:comp)
pos2-armode       =continuous #
    (0:off,1:continuous,2:instantaneous,3:fix-and-hold)
pos2-gloarmode    =on        # (0:off,1:on,2:autocal)
pos2-bdsarmode    =on        # (0:off,1:on)
pos2-arthres      =3
pos2-arthres1     =0.9999
pos2-arthres2     =0.25
```

```
pos2-arthres3    =0.1
pos2-arthres4    =0.05
pos2-arlockcnt   =0
pos2-arelmask    =0         # (deg)
pos2-arminfix    =10
pos2-armaxiter   =1
pos2-elmaskhold  =0         # (deg)
pos2-aroutcnt    =5
pos2-maxage      =30        # (s)
pos2-syncsol     =off       # (0:off,1:on)
pos2-slipthres   =0.05      # (m)
pos2-rejionno    =30        # (m)
pos2-rejgdop     =30
pos2-niter       =1
pos2-baselen     =0         # (m)
pos2-basesig     =0         # (m)
out-solformat    =llh       # (0:llh,1:xyz,2:enu,3:nmea)
out-outhead      =on        # (0:off,1:on)
out-outopt       =on        # (0:off,1:on)
out-timesys      =gpst      # (0:gpst,1:utc,2:jst)
out-timeform     =hms       # (0:tow,1:hms)
out-timendec     =3
out-degform      =deg       # (0:deg,1:dms)
out-fieldsep     =
out-outsingle    =off       # (0:off,1:on)
out-maxsolstd    =0         # (m)
out-height       =ellipsoidal # (0:ellipsoidal,1:geodetic)
out-geoid        =internal  #
   (0:internal,1:egm96,2:egm08_2.5,3:egm08_1,4:gsi2000)
out-solstatic    =all       # (0:all,1:single)
out-nmeaintv1    =0         # (s)
out-nmeaintv2    =0         # (s)
out-outstat      =off       # (0:off,1:state,2:residual)
stats-eratio1    =100
stats-eratio2    =100
stats-errphase   =0.003     # (m)
stats-errphaseel =0.003     # (m)
stats-errphasebl =0         # (m/10km)
stats-errdoppler =10        # (Hz)
stats-stdbias    =30        # (m)
stats-stdiono    =0.03      # (m)
stats-stdtrop    =0.3       # (m)
stats-prnaccelh  =10        # (m/s^2)
stats-prnaccelv  =10        # (m/s^2)
stats-prnbias    =0.0001    # (m)
stats-prniono    =0.001     # (m)
stats-prntrop    =0.0001    # (m)
stats-prnpos     =0         # (m)
stats-clkstab    =5e-12     # (s/s)
ant1-postype     =llh       #
   (0:llh,1:xyz,2:single,3:posfile,4:rinexhead,5:rtcm,6:raw)
ant1-pos1        =90        # (deg|m)
```

```
ant1-pos2        =0         # (deg|m)
ant1-pos3        =-6335367.62849036 # (m|m)
ant1-anttype     =
ant1-antdele     =0         # (m)
ant1-antdeln     =0         # (m)
ant1-antdelu     =0         # (m)
ant2-postype     =llh       #
    (0:llh,1:xyz,2:single,3:posfile,4:rinexhead,5:rtcm,6:raw)
ant2-pos1        =90        # (deg|m)
ant2-pos2        =0         # (deg|m)
ant2-pos3        =-6335367.62849036 # (m|m)
ant2-anttype     =
ant2-antdele     =0         # (m)
ant2-antdeln     =0         # (m)
ant2-antdelu     =0         # (m)
ant2-maxaveep    =0
ant2-initrst     =off       # (0:off,1:on)
misc-timeinterp  =off       # (0:off,1:on)
misc-sbasatsel   =0         # (0:all)
misc-rnxopt1     =
misc-rnxopt2     =
misc-pppopt      =
file-satantfile  =
file-rcvantfile  =
file-staposfile  =
file-geoidfile   =
file-ionofile    =
file-dcbfile     =
file-eopfile     =
file-blqfile     =
file-tempdir     =
file-geexefile   =
file-solstatfile =
file-tracefile   =
```

pos1-posmode In the case of UAV trajectory computation, the *kinematic* mode is recommanded. The mode *static-start* usually works better if the rover is stationary long enough at the begining, because it take advantage of the knowledge that the rover is not moving initially.

pos1-frequency *l1* for single frequency receivers, *l1+l2* if the rover is dual frequency GPS/GLONASS/Beidou.

pos1-soltype This option sets the temporal direction for kalman filter. For real-time processing, *forward* is the only choice. When choosing *combined* for post-processing, the kalman filter runs forward then backward and results are combined. For one epoch, if both directions give a *fix* (Q=1), the final result is the average of two solutions unless the difference between two solutios is too large in which case the result status will be

float (Q=2). If only one direction gives *fix*, this result will be the final solution and solution status will be *fix*. If both directions give *float* results, the average will be the final solution and the solution status will be *float*. It does not mean that *combined* always gives better results, a false *fix* in either direction can cause the final result to be *float* and incorrect.

pos1-elmask This option sets the minimum satellite elevation. The more open the sky view, the lower this value can be set to. Normally it is set to 15° to reduce the perturbation of multipath.

pos1-snrmask_(r|b),pos1-snrmask_L(1|2|5) The first two options activate the satellite SNR mask for rover and base, respectively. It sometimes can be more effective than `pos1-elmask` to eliminate poor satellites since it is a more direct measurement of signal quality. The last three options set the threshold of SNR every five degres of elevation for frequency *L1*, *L2* and *L5*.

pos1-exclsats By giving the `PRN` of satellites, they will be exclude from the calculation. It is useful when certain satellites are observed to be bad.

navsys This option sets the GNSS systems to be included in the calculation. For example, if one wants to include `GPS`, `GLONASS` and `SBAS`, this option should be set to $1 + 2 + 4 = 7$.

pos2-armode This option sets the interger ambiguity resolution method. *fix-and-hold* mode uses feedback from *fix* solutions to help track ambiguities. *Continuous* mode does not take advantages of *fix* solution to adjust the phase bias states, which makes it the most immune to false *fix* solutions.

pos2-arthres This option sets the minimum ratio of squared residuals bewteen the best solution and the second-best solution to declare a solution as *fix*. Normally it is set to 3.

ant-postype, ant2-pos(1|2|3) These options together give the position information of the base. The position information is used for calculation in relative mode.

For more details of `RTKLib` processing, please refer to `RTKLib` manual. The blog site https://rtklibexplorer.wordpress.com/about/ for GNSS processing with `RTKLib` and low-cost GNSS receivers.

Annexe C

Photogrammetric processing with MicMac

MicMac is organised in a number of modules, accessible through a common command mm3d. Each command requires two types of arguments, mandatory ones and optional ones. Due to the large amount of optional arguments, when giving an example command, only a part of the optional arguments are presented. For complete documentation of MicMac, please refer to the *github* repository https://github.com/micmacIGN/.

C.1 Commands of classical workflow

Convert GNSS trajectory into MicMac format

The computed GNSS position solution gives information on antenne phase center, which will later be included as observation in the bundle block adjustment. It can also help selecting overlappig image couples before the computation of tie points, which reduces significantly the computation time than performing tie points extraction on every image couple. To convert the GNSS trajectory into MicMac format for further processing, one can use the command TestLib convRTK.

```
$ mm3d TestLib convRTK "input_file_directory" "input_file"
    ChSys=GeoC@Lambert93 OffSet=[910000,6500000,0] Median=1
*****************************
*  Help for Elise Arg main *
*****************************
Mandatory unnamed args :
  * string :: {Directory}
  * string :: {RTKlib Output (MyFile.txt) file}
Named args :
  * [Name=Out] string :: {Output file name ; Def=MyFile.xml}
  * [Name=ChSys] string :: {Change coordinate file}
  * [Name=OffSet] Pt3dr :: {Subtract an offset to all points}
  * [Name=Median] bool :: {Export the median of coordinates; Def = false}
```

The example command converts the coordinate system from *GeoCentric* to *Lambert93*, and puts the converted solution into `MicMac` format. The given offset $[910000, 6500000, 0]$ is extracted from the solution, and the median is calculated.

Compute GNSS solution corresponding to each image

In the case where the GNSS system is not synchronized with the image acquisition system, the GNSS trajectory needs to be interpolated to obtain solutions corresponding to each image. The command `TestLib InterpImTM` is possible to perform this calculation basing on image stamp time.

```
$ mm3d TestLib InterpImTM "input_file_directory" "GNSS_trajectory_file"
    "imgae_timestamp_file" Out="output_file" Modespline=0 WithAngle=1 Inc=1
    SpeedInc=1
*****************************
*  Help for Elise Arg main *
*****************************
Mandatory unnamed args :
  * string :: {Directory}
  * string :: {GPS .xml file trajectory}
  * string :: {Image TimeMark .xml file}
Named args :
  * [Name=Out] string :: {Name Output File ; Def =
      GPSFileName-TMFileName.txt}
  * [Name=ModeSpline] bool :: {Interpolation spline, def=true }
  * [Name=WithAngle] bool :: {Generate fake angle, def=true }
  * [Name=Inc] bool :: {Export uncertainty, def=true}
  * [Name=SpeedInc] bool :: {Use speed variation in uncertainty
      estimation,def=true }
  * [Name=ChSys] string :: {To chang coorrdinate system}
```

The example command takes GNSS solution (time + position) and image time information, then performs parabolic interpolation to compute GNSS solution corresponding to each image. It means every image gets a position with respect to its acquisition time. One can also perform the *Spline* interpolation by setting `ModeSpline=1`.

The `image_timestamp_file` should give time information of image in `Modified Julian Day`, as shown below.

```
<?xml version="1.0" ?>
<DicoImgsTime>
     <CpleImgTime>
          <NameIm>img_029_D1_50_00100.thm.tif</NameIm>
          <TimeIm>58030.4361291317255</TimeIm>
     </CpleImgTime>
     <CpleImgTime>
          <NameIm>img_029_D1_50_00101.thm.tif</NameIm>
          <TimeIm>58030.4361580670738</TimeIm>
     </CpleImgTime>
</DicoImgsTime>
```

The command `InterpImTM` gives a `.txt` file containing image name and corresponding camera position. For it to be used for further processing in `MicMac` in accordance with other commands, one should use command `OriConvert` to convert it into a certain structure. The argument `ChSys` allows to conversion between different coordinate systems. When argument `NameCple` is active, a coarse list of overlapping images will be calculated basing on camera positions. It can be given as *a priori* information for the extraction of tie points.

```
$ mm3d OriConvert "file_format" "camera_position_file" "output_folder"
****************************
*  Help for Elise Arg main *
****************************
Mandatory unnamed args :
  * string :: {Format specification}
  * string :: {Orientation file}
  * string :: {Targeted orientation}
Named args :
  * [Name=ChSys] string :: {Change coordinate file}
  * [Name=NameCple] string :: {Name of XML file to save couples}
```

Compute tie points

The extraction of tie points can be realized with the command `Tapioca`. The option `MulScale` (i.e. Multi-Scale) is recommanded for time-saving purposes. When this option is active, a first computation of tie points is made for all image couples at a low resolution to determine overlapping images. Then a second computation at the desired high resolution is done on these overlapping image couples, which leads to a significant reduction of computation time. It is also possible to give directly a list of overlapping images with the option `File`.

```
$ mm3d Tapioca MulScale "image_pattern" LowResolution Resolution
****************************
*  Help for Elise Arg main *
****************************
Mandatory unnamed args :
  * string :: {Full Name (Dir+Pat)}
  * INT :: {Size of Low Resolution Images}
  * INT :: {Size of High Resolution Images}
Named args :
  * [Name=ExpTxt] bool :: {Export files in text format (Def=false means
      binary)}
  * [Name=PostFix] string :: {Add postfix in directory}
  * [Name=NbMinPt] INT :: {Minimum number of points}
```

Reduction of tie points (optional)

`MicMac` offers different tie point filtering approaches. These approaches reduce the computation time and the need of computation power while maintaining the quality

of final results. `Ratafia`, `Schnaps` and `PHO_MI` are part of the commands that perform tie point reduction.

Relative sensor Orientation

The sensor orientation is composed in two parts, internal orientation and external orientation. With tie points as observation, a first bundle block adjustment is performed in relative scale with the command `Tapas`. The sensor internal orientation can be either determined during the process or given *a priori* with the argument `InCal`. It is also possible to give an external orientation as initial solution with the argument `InOri`. Multiple camera calibration models are available, such as for instance : `Fraser`, `Ebner`, `Brown`.

```
$ mm3d Tapas "camera_model" "image_pattern"
*****************************
*  Help for Elise Arg main *
*****************************
Mandatory unnamed args :
  * string :: {Calibration model}
  * string :: {Full Directory (Dir+Pattern)}
Named args :
  * [Name=Out] string :: {Directory of Output Orientation}
  * [Name=InCal] string :: {Directory of Input Internal Orientation
      (Calibration)}
  * [Name=InOri] string :: {Directory of Input External Orientation}
```

georeferencing

There are two ways to georeference the relative sensor orientation issued from last step : with GCPs or with GNSS solution. To georeference with GCPs, they should firstly be measured in images. The command `SaisieAppuisInit` and `SaisieAppuisPredic` are the tools to acquire image measurements manually. Afterwards, the command `GCPBascule` estimates a 3D similarity transformation and the relative sensor orientation is transformed into the absolute frame of GCPs.

```
$ mm3d GCPBascule "image_pattern" "relative_sensor_orientation"
    "output_folder" "GCP_3D_coordinate_file" "GCP_image_measurement_file"
*****************************
*  Help for Elise Arg main *
*****************************
Mandatory unnamed args :
  * string :: {Full name (Dir+Pat)}
  * string :: {Orientation in}
  * string :: {Orientation out}
  * string :: {Ground Control Points File}
  * string :: {Image Measurements File}
Named args :
  * [Name=CPI] bool :: {when Calib Per Image has to be used}
```

To georeference with GNSS solution, it is the command `CenterBascule` that should be used. A 3D similarity transformation is estimated based on the position of camera optical center comming from GNSS solution and the relative bundle block adjustment.

```
$ mm3d CenterBascule "image_pattern" "relative_sensor_orientation"
    "GNSS_solution" "output_folder"
*****************************
*  Help for Elise Arg main *
*****************************
Mandatory unnamed args :
  * string :: {Full name (Dir+Pat)}
  * string :: {Orientation in}
  * string :: {Localization of Information on Centers}
  * string :: {Orientation out}
Named args :
  * [Name=L1] bool :: {L1 minimization vs L2; (Def=false)}
  * [Name=CalcV] bool :: {Use speed to estimate time delay (Def=false)}
```

Compensation

The obtained absolute sensor orientation will be served as an initial solution for compensation (bundle block adjustment). Different types of observations are possible : tie points, GCPs, GNSS solution, etc. Here, the lever-arm will be estimated if GNSS solution is provided. It is also possible to estimate multiple lever-arms at once.

```
$ mm3d Campari "image_pattern" "input_sensor_orientation"
    "output_sensor_orientation"
    "GCP=[3D_coordinate_file,3D_uncertainty,2D_coordinate_file,2D_uncertainty]
    EmGPS=[GNSS_solution,uncertainty_xy,uncertainty_z]
    GpsLa=[initial_lever_arm]
*****************************
*  Help for Elise Arg main *
*****************************
Mandatory unnamed args :
  * string :: {Full Directory (Dir+Pattern)}
  * string :: {Input Orientation}
  * string :: {Output Orientation}
Named args :
  * [Name=GCP] vector<std::string> ::
      {[GrMes.xml,GrUncertainty,ImMes.xml,ImUnc]}
  * [Name=EmGPS] vector<std::string> :: {Embedded GPS [Gps-Dir,GpsUnc,
      ?GpsAlti?], GpsAlti if != Plani}
  * [Name=GpsLa] Pt3dr :: {Gps Lever Arm, in combination with EmGPS}
  * [Name=MultiLA] vector<std::string> :: {If multiple LA indicates the
      patterns of different subsets (first pattern being implicitely first
      mandatory parameter) }
  * [Name=IncLA] Pt3dr :: {Inc on initial value of LA (Def not used)}
  * [Name=PatGPS] string :: {When EmGPS, filter images where GPS is used}
  * [Name=CPI1] bool :: {Calib Per Im, Firt time}
  * [Name=CPI2] bool :: {Calib Per Im, After first time, reUsing Calib Per
      Im As input}
```

```
  * [Name=AllFree] bool :: {Refine all calibration parameters (Def=false)}
  * [Name=PoseFigee] bool :: {Does the external orientation of the cameras
      are frozen or free (Def=false, i.e. camera poses are free)}
  * [Name=SH] string :: {Set of Hom, Def="", give MasqFiltered for result of
      HomolFilterMasq, set NONE if unused}
  * [Name=FocFree] bool :: {Foc Free (Def=false)}
  * [Name=PPFree] bool :: {Principal Point Free (Def=false)}
  * [Name=AffineFree] bool :: {Affine Parameter (Def=false)}
  * [Name=DegAdd] INT :: {When specified, degree of additionnal parameter}
  * [Name=DegFree] INT :: {When specified degree of freedom of parameters
      generiqs}
  * [Name=DRMax] INT :: {When specified degree of freedom of radial
      parameters}
  * [Name=ExportSensib] bool :: {Export sensiblity (accuracy) estimator :
      correlation , variance, inverse matrix variance}
```

There are several arguments that can be useful in other cases.

- `MultiLA` gives multiple image patterns separated by their lever-arm, which makes it possible to estimate multiple lever-arm at once
- `IncLA` sets the uncertainty of lever-arm when given as initial solution, so as to modify how it is weighted in bundle block adjustment
- `PatGPS` specifies images that the GNSS solution will be taken into account. This enables the inclusion of images without position information provided by GNSS
- `CPI(1|2)` allows to estimate one camera calibration per image

Evaluate the accuracy

Once the compensation is done, the accuracy of the issued sensor orientation can be evaluated with the command `GCPCtrl`. The residuals on control points (CPs) as well as the statistic information are given.

```
$ mm3d GCPCtrl "image_pattern" "sensor_orientation" "CP_3D_coordinates"
    "CP_2D_coordinates"
*****************************
*  Help for Elise Arg main *
*****************************
Mandatory unnamed args :
  * string :: {Full name (Dir+Pat)}
  * string :: {Orientation in}
  * string :: {Ground Control Points File}
  * string :: {Image Measurements File}
Named args :
  * [Name=CPI] bool :: {when Calib Per Image has to be used}
  * [Name=ShowU] bool :: {Show unused point (def=true)}
  * [Name=OutTxt] string :: {Name TXT file for Ctrl result (def=false)}
  * [Name=OutJSON] string :: {Name .geojson file for Ctrl result (def=false)}
```

C.2 Commands for special purposes

The above-mentioned is the classical workflow employed in this thesis work. In the following, commands for special purposes are introduceds.

Generate simulated tie points

In **Chapter** 4, simulated tie points are generated basing on real sensor orientation and tie points with the command `TestLib GenerateTP`.

```
$ mm3d TestLib GenerateTP "image_pattern" "real_tie_points"
    "real_sensor_orientation"
*****************************
*  Help for Elise Arg main *
*****************************
Mandatory unnamed args :
  * string :: {Image Pattern}
  * string :: {PMul File}
  * string :: {Ori}
Named args :
  * [Name=Out] string :: {Output name of generated tie points, Def=simulated}
  * [Name=Seed] INT :: {Seed for generating random noise}
  * [Name=NoiseGaussian] vector<double> :: {[meanX,stdX,meanY,stdY]}
  * [Name=ImNX] string :: {image containing noise on X-axis}
  * [Name=ImNY] string :: {image containing noise on Y-axis}
  * [Name=TP3D] string :: {Output 3D positions of tie points without
      distortion.}
```

The pseudo-intersection is performed with given tie points and sensor orientation and 3D points corresponding to given tie points are computed. Then, these 3D points are re-projected onto images, simulated, error-free tie points are calculated. The argument `Seed` and `NoiseGaussian` generate random Gaussian noise with given parameters and add them to calculated tie points. Noise on tie points can also be specified and given in the form of images with arguments `ImNX` and `ImNY`.

Generate simulated image measurements of GCPs

Accordingly, simulated image measurements of GCPs can be generated with the command `TestLib GenerateMAF`.

```
$ mm3d TestLib GenerateMAF "image_pattern" "sensor_orientation"
    "GCP_3D_coordinate_file"
*****************************
*  Help for Elise Arg main *
*****************************
Mandatory unnamed args :
  * string :: {Image pattern}
  * string :: {Ori}
  * string :: {File containning GCP coordinates}
```

```
Named args :
  * [Name=Out] string :: {Output name of the generated MAF file,
      Def=Gen_MAF_Ori.xml}
  * [Name=ImNX] string :: {image containing noise on X-axis}
  * [Name=ImNY] string :: {image containing noise on Y-axis}
  * [Name=OriRS] string :: {If generate image measurement file for rolling
      shutter, give generated Ori name}
```

The arguments `ImNX` and `ImNY` work similarly as with the command `TestLib GenerateTP`. The argument `OriRS` generate image measurements that simulate the rolling shutter effect.

Generate synthetic dataset with rolling shutter effect

In **Chapter** 4, a synthetic dataset is generated to simulate the rolling shutter effect. The main idea is to generate two sets of sensor orientation, one corresponding to the beginning of camera exposure and the other one corresponding to the end. From these two sets of sensor orientation, intermediate sensor orientations corresponding to each line can be interpolated. Observations such as tie points and image measurements of GCPs are then generated accordingly.

The command `TestLib GenerateOrient` generates a file containing the variation of sensor orientation with respect to the original ones based on the sensor motion related information and the time interval between the beginning and the end of camera exposure. The position change of camera i is computed by linearly interpolating the position of camera i and camera $i+1$. The angular change is generated with a random rotation axis and a rotation angle of Gaussian distribution.

```
mm3d TestLib GenerateOrient "image_pattern" "orignal_sensor_orientation"
    [time_interval_between_two_images,rolling_shutter_readout_time]
    [mean_angular,std_angular]
*****************************
*  Help for Elise Arg main *
*****************************
Mandatory unnamed args :
  * string :: {Image Pattern, make sure images are listed in the right order}
  * string :: {Ori}
  * Pt2dr :: {Time Interval, interpolate to generate translation, [cadence
      (s), exposure time (ms)]}
  * Pt2dr :: {Gaussian distribution parameters of angular velocity for
      rotation generation (radian/s), [mean,std]}
Named args :
  * [Name=Out] string :: {Output file name for genarated orientation,
      def=Modif_orient.txt}
  * [Name=Seed] INT :: {Random engine, if not give, computer unix time is
      used.}
  * [Name=Turn] vector<std::string> :: {List of image names representing
      flight turns (set the translation T(i) as T(i-1))}
  * [Name=Trans] bool :: {Take into account translation, def=true}
```

The generation of tie points impacted by the rolling shutter effect is done with the command `SimuRolShut`. Firstly, a pseudo-intersection is performed with the original tie points and the original sensor orientations to obtain a set of 3D points. Then the 3D points are re-projected onto images with interpolated camera position and rotation to obtain modified tie points. The variation of sensor orientation should either be given for each image or given in a single line to the whole image block. It is also possible to add Gaussian noise on tie points with the argument `NoiseGaussian`.

```
mm3d TestLib SimuRolShut "image_pattern" "original_tie_points"
    "original_sensor_orientation"
    "output_sensor_orientation_corresponds_to_the_end_of_exposure"
    "file_containing_orientation_change"
*****************************
*  Help for Elise Arg main *
*****************************
Mandatory unnamed args :
  * string :: {Image Pattern}
  * string :: {PMul File}
  * string :: {Ori}
  * string :: {Ori for modified ori files}
  * string :: {File containing pose modification for each image, file size =
      1 or # of images}
Named args :
  * [Name=Out] string :: {Output name of generated tie points,
      default=simulated}
  * [Name=Line] INT :: {Read file containing pose modification from a
      certain line, def=3 (two lines for file header)}
  * [Name=Seed] INT :: {Seed for generating gaussian noise}
  * [Name=NoiseGaussian] vector<double> :: {[meanX,stdX,meanY,stdY]}
```

The generation of image measurements impacted by the rolling shutter effect can be done with the previously mentioned command `TestLib GenerateMAF`. It is similar to the generation of modified tie points, the camera orientation corresponding to the end of camera exposure is specified with the argument `OriRS`.

Calculate camera velocity

In **Chapter** 7, a two-step approach for the correction of rolling shutter effect is proposed. Since the camera velocity is not directly available, it is estimated with the command `XifDate2Txt`. The idea is to firstly extract time-related information of each image from the metadata. The camera velocity of camera i is estimated as the ratio of camera position change and time interval between camera $i-1$ and camera $i+1$.

```
mm3d XifDate2Txt "image_pattern" CalVOri="sensor_orientation"
*****************************
*  Help for Elise Arg main *
*****************************
Mandatory unnamed args :
  * string :: {Full Name}
Named args :
```

```
  * [Name=Out] string :: {Output file name, Def=XifDate.txt}
  * [Name=CalVOri] string :: {Calculate velocity when an Ori is available}
  * [Name=OutCalcV] string :: {Output file name for calculated velocity}
  * [Name=Header] bool :: {Include header file for velocity file, def=true}
```

Correct observations impacted by rolling shutter effect

The correction of rolling shutter effect presented in **Chapter** 7 is done with the command `TestLib ReechRolShut` on tie points and image measurements. Please refer to Section 7.5 for detailed illustration.

```
mm3d TestLib ReechRolShut "image_pattern" "sensor_orientation"
    "readout_time" "camera_velocity_file" SHIn="tie_points_to_be_corrected"
    MAFIn="image_measurements_to_be_corrected"
*****************************
*  Help for Elise Arg main *
*****************************
Mandatory unnamed args :
  * string :: {Image pattern}
  * string :: {Input orientation folder}
  * REAL :: {Rolling shutter speed (us/line)}
  * string :: {File containing camera velocity}
Named args :
  * [Name=SHIn] string :: {Input tie point file (new format)}
  * [Name=SHOut] string :: {Folder postfix for tie point output folder,
      def=_Reech}
  * [Name=MAFIn] string :: {Input image measurement file}
  * [Name=MAFOut] string :: {Output image measurement file,
      def=Mesure_Finale-Reech.xml}
```

Annexe D

Acquisition report *LP2017*

Date : 02/10/2017-05/10/2017
Site : *La Pallière* (PK133.4), Culoz, France
Camera operator : `IGN-LaSTIG`
UAV operator : `Ifsttar`
Topology operator : `IGN-TS`
Coordination `CNR` : Paul-Henri Faure

D.1 Context and objective

This is the first aerial acquisition carried out in the framework of this thesis. The site of interest is the dike *La Pallière* at Culoz, France. The survey field is indicated in Figure. D.1. It is a linear scene of 1200 m with a small turn on the north end.

(a) (b)

Figure. D.1 – Site of interest for acquisition *LP2017*

Three acquisitions have been performed on the same area in the previous thesis work of Tournadre [2015]. The objective for this acquisition is to benefit from the development of materials (metric camera and on-board GNSS system) and to optimize the acquisition strategy so that the same mapping accuracy can be reached with reduced field work. For this mission, a GNSS module is added to the survey system and integrated into the optical sensor.

D.2 UAV and embarked sensors

The UAV employed for aerial acquisition is the *SURVEY Copter 1B*. It has a wingspan of 1.82m and a length of 1.66m. Powered by a gasoline engine, the maximal payload capacity of the UAV is 4.1kg and the endurance is up to 60min. Given a pre-set flight plan registered in the command station, the flight can be performed automatically. Thus, a steady longitudinal/lateral overlap can be assured. An aluminium base mounted on the UAV is adopted for rigid camera installation and cable fixation. The camera embarked on the UAV is a panchromatic lightweight metric camera of `IGN`. The GNSS module developed in `IGN`, the `GeoCube`, is integrated in the camera to provide positioning information.

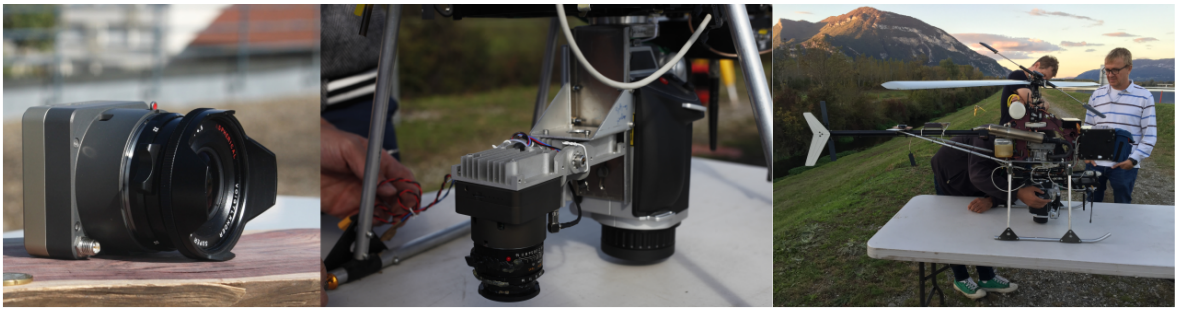

Figure. D.2 – **Left** : camera **Middle** : camera set-up on UAV (**Right**) : UAV

D.3 Topographical landmarks

The topological field work is performed by the team `IGN-TS` (cf. Figure. D.3). Three types of topological landmarks are employed : GNSS receiver + visual target, classical visual target and ground surface (cf. Figure. D.4).

- The GNSS receiver (`GeoCube`) is placed in the center of a visual target. The position issued from GNSS post-processing is actually the position of the antenna phase center. It is a virtual point with can not be physically located, which means it can not be measured in image space. Therefore, a visual target is fixed to the GNSS receiver. By exploiting the 2D and 3D coordinates of $P1 - P4$ on the visual target, we expect to be able to locate $P5$, the antenna phase center in image space. This type of landmark is placed every 100 m, alternatively on the left and right bank of the dike. A total of 10 sets of GNSS receiver + visual target are placed, the four points on the visual target are surveyed by topology.

- The classical visual targets are the same as the ones fixed to GNSS receiver. They are placed every 30 m, alternatively on the left and right bank of the dike as well. A total of 39 classical visual targets are placed and surveyed by topology.
- The ground surfaces are square surfaces marked with points on the corners and the center. They are placed every 100 m on the center of the dike. A total of 12 ground surfaces are placed and surveyed with topology.

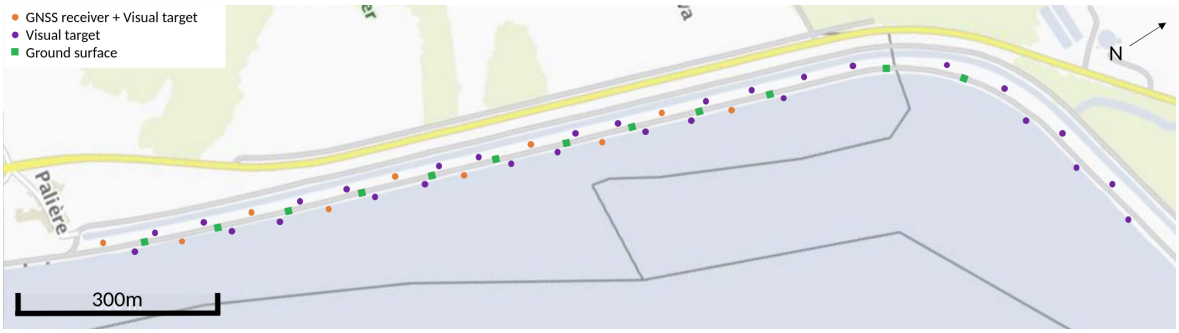

Figure. D.3 – An illustration of the landmark layout plan.

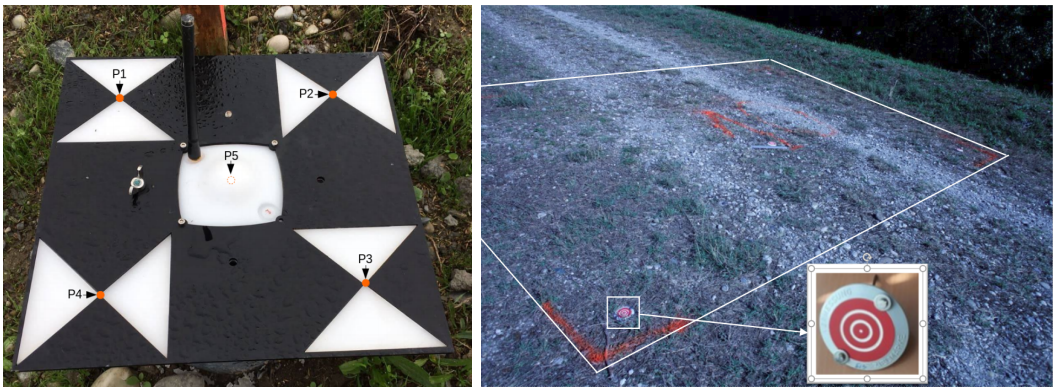

(a) GNSS receiver + Visual target (b) Ground surface

Figure. D.4 – An illustration of the topographical landmarks.

D.4 Acquisition plan

The acquisition field is divided into two segments of 600 m and surveyed separately. The first segment of 600 m consists of the south part of the dike, while the second segment consists of the rest of the dike including the turn at the north end.

The first segment is surveyed with the routine acquisition configuration, a nadir flight of 3 strips at 50 m (denoted as *s1-n50*). This configuration is simple and economic, whereas not preferable when high photogrammetric accuracy is demanded. The second segment consists of three flights, a nadir flight of 3 strips at 50 m (denoted as *s2-n50*), an oblique flight of 3 strips at 50 m (denoted as *s2-o50*) and a nadir flight of 2 strips with the first strip at 70 m and the second strip at 30 m (denoted as *s2-n3070*). This configuration of multiple acquisition angles and multiple flight heights is desirable though costly. The objective is to investigate, given a good camera model and a correct lever-arm, the achievable accuracy of a simple while not preferable network

configuration. The estimated camera model and lever-arm of the image block of segment 2 (*s2-n50 + s2-o50 + s2-n3070*) is considered of high accuracy and used for sensor pre-calibration of the image block of Segment 1 (*s1-n50*).

Figure D.5 depicts the conducted flights, the flight information is given in Table D.1.

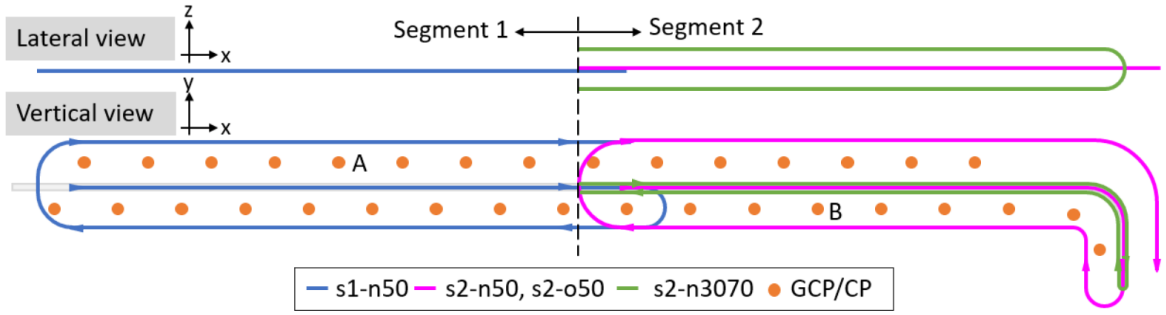

Figure. D.5 – An illustration of the conducted flights.

Flight		***s1-n50***	***s2-n50***	***s2-n3070***	***s2-o50***
Nb of images		395	315	200	323
Height (m)		50	50	30, 70	50
Orientation		nadir	nadir	nadir	oblique
Nb of strips		3	3	2	3
Overlap (%)	forward	80			
	side	70			
GCP accuracy (mm)	horizontal	1.3			
	vertical	1			
camera focal length (mm)		35			
GSD (mm)		10	10	6, 14	10

Table. D.1 – Details on conducted flights – *LP2017*.

D.5 Discussion

Main results are presented and discussed in **Chapter** 5. Here, supplementary discussions that are not covered in **Chapter** 5 are presented.

We investigated the position of $P1 - P4$ on the visual target as well as the antenna phase center computed with GNSS post-processing. It is difficult to draw conclusions on the relation between these points. Normally, geodetic GNSS antenna uses patented techniques for multipath mitigation, noise reduction and the antenna phase center is well calibrated. The antenna used by `GeoCube` may not have a stable antenna phase center with respect to the physical body of the receiver. Factors such as the environment multipath, the direction of incoming signal can influence the computed position. Therefore, when expecting a centimetric mapping accuracy, it is recommanded to survey physical points that can be precisely measured in image space. In the case where the requirement on mapping accuracy is less stringent, e.g. an decimetric accuracy is

expected, the `GeoCube` can be a low-cost, time-saving alternative to traditional ground points.

Annexe E

Acquisition report *Roche2018*

Date : 30/07/2018-02/08/2018
Site : *Roche de Glun* (PK99.2), Bourg-lès-Valence, France
Camera operator : `IGN-LaSTIG`
UAV operator : `AvionJaune`
Topology operator : `IGN-LaSTIG`
Coordination `CNR` : Paul-Henri Faure

E.1 Context and objective

This acquisition takes place at the dike *Roche de Glun* at Bourg-lès-Valence, France. The survey field is about 500 m's long with two parallel dikes (cf. Figure. E.1). The survey field is covered by trees and plants.

(a) (b)

Figure. E.1 – Site of interest for acquisition *Roche2018*

Firstly, we want to test the integration of embarked sensors onto UAV before the annual acquisition of the dike *La Pallière*, to verify the power supply, the rigidity of the mounting system and the global functioning. To avoid substantial field work and cost, ground points are surveyed with GNSS in relative RTK mode. The UAV trajectory is post-processed in relative mode with respect to a base station installed on the dike. The majority of dike being covered by trees, the GNSS communication is strongly pertubated. It is also the occasion to find out the mapping accuracy one can achieve under this unfavourable condition.

E.2 UAV and embarked sensors

The UAV employed for aerial acquisition is the *OnyxStar FOX-C8-HD*, an 8 coaxial motors drone. It can fly up to 34 min with a maximum payload of 3 kg. Its placement of the batteries makes the replacement operation as short as 60 s, which means it can work long periods with reduced breaks. The flights are performed by the company `AvionJaune`. The embarked sensors are :

- Two panchromatic lightweight cameras of `IGN`
- One thermal camera *Optris pi 640*
- Two sets of GNSS receiver + antenna integrated in the two lightweight cameras

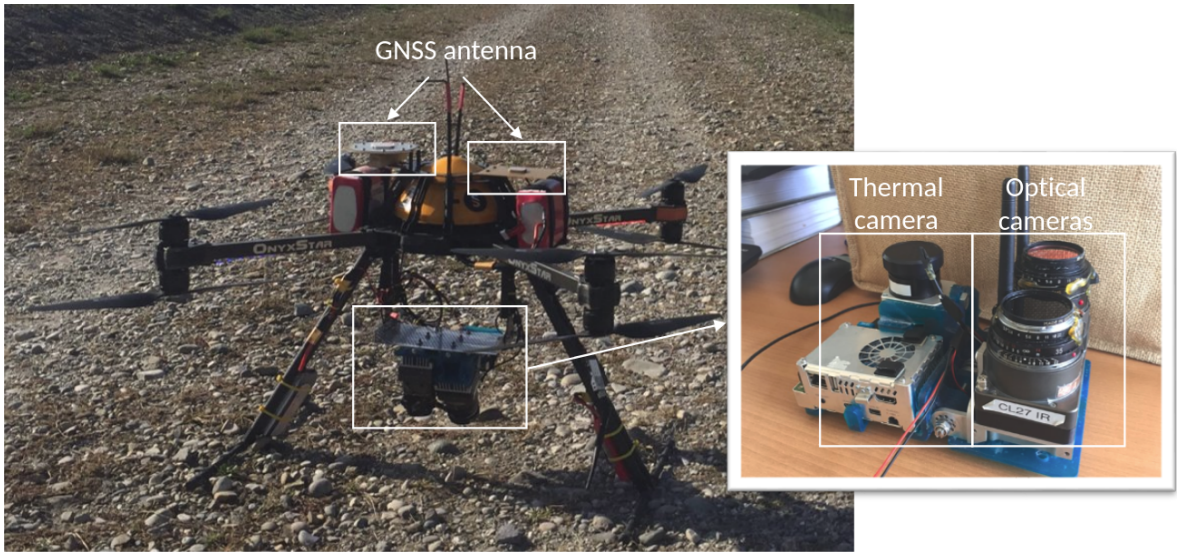

Figure. E.2 – The employed UAV and embarked sensors.

E.3 Topological landmarks

The same visual target as in acquisition *LP2017* is used and surveyed by GNSS in relative RTK mode (cf. Figure. E.4).

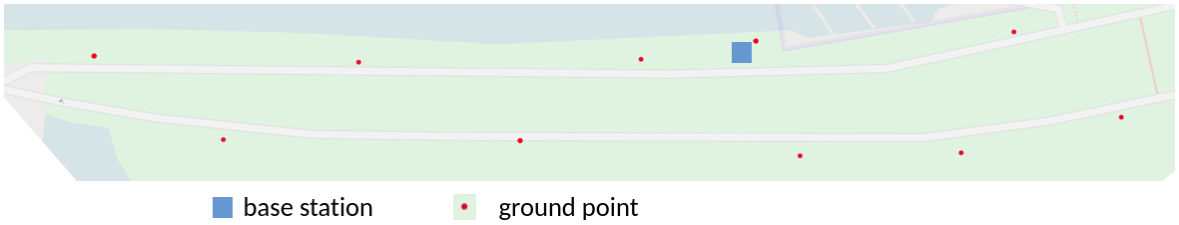

Figure. E.3 – An illustration of the landmark layout plan.

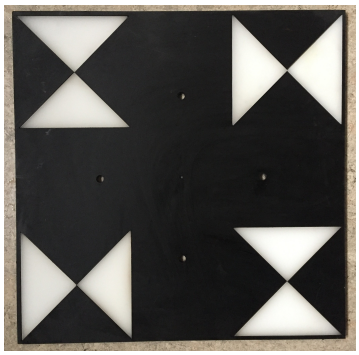

Figure. E.4 – An illustration of the topological landmarks.

E.4 Acquisition plan

Three flights are conducted on the site of interest. The first two flights are performed at 50 m with 3 strips. The two optical cameras are oriented such that one is nadir-looking and the other is oblique and their orientations are inversed for the two flights. The second flight consists of 2 strips at 30 m and 2 strips at 70 m, the two cameras are oriented as well one being nadir and the other being oblique. The thermal camera is always oriented nadir. Details of the conducted flights are given in Table. E.1, information regarding thermal images are omitted since they are not discussed in this thesis work. Note that *cam2* did not work as expected in *flight 2* and no images are acquired.

Flight	1		2		3	
	cam1	cam2	cam1	cam2	cam1	cam2
Height (m)	50		50		30, 70	
Nb of Strips	3		3		2 per height	
Orientation	na	ob	ob	na	na	ob
Nb of images	155	151	156	0	187	182

Table. E.1 – Details on conducted flights – *Roche2018*.

Annexe F

Acquisition report *LP2018*

Date : 10/09/2018-14/09/2018
Site : *La Pallière* (PK133.4), Culoz, France
Camera operator : `IGN-LaSTIG`
UAV operator : `AvionJaune`
Topology operator : `IGN-TS`
Coordination `CNR` : Paul-Henri Faure

F.1 Context and objective

A second aerial acquisition is conducted for the mapping of the dike *La Pallière*. This time, the survey field starts at the same point as for the acquisition *LP2017*. The end point is extended to the bridge, the total length of the scene reaches 2 km (cf. Figure. F.1).

(a) (b)

Figure. F.1 – Site of interest for acquisition *LP2018*

The objective of this acquisition is to verify the strategy proposed in **Chapter** 5 : applying an in-flight camera calibration to an unfavourable acquisition geometry. It is shown that this strategy gives satisfying results on a corridor scene of 600 m. In this acquisition, the survey scope is extended to see the feasibility of the proposed strategy on a longer corridor scene.

F.2 UAV and embarked sensors

The UAV employed for aerial acquisition is the *OnyxStar FOX-C8-HD*, an 8 coaxial motors drone. The integration of on-board sensors to the UAV is tested with the acquisition *Roche2018*. The flights are performed by the company `AvionJaune`. The embarked sensors are :

- Two panchromatic lightweight cameras of `IGN`
- One thermal camera *Optris pi 640*
- Two sets of GNSS receiver + antenna integrated in the two lightweight cameras

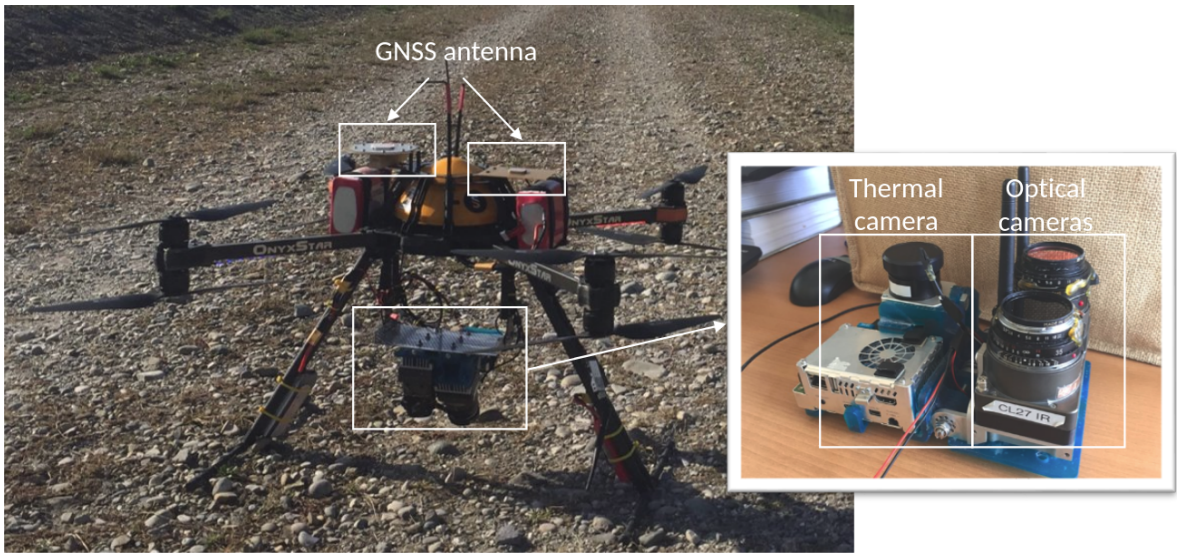

Figure. F.2 – The employed UAV and embarked sensors.

F.3 Topographical landmarks

The topograpical field work is performed by the team `IGN-TS` (cf. Figure. F.3). Two types of topographical landmarks are employed : ground points and ground surfaces (cf. Figure. F.4).

- The ground points are placed every 100 m along the site of interest, alternately on the left and right bank of the dike. A total of 21 points are placed and topologically surveyed.
- The ground surfaces are square surfaces marked with points on the corner and the center. They are placed every 200 m on the center of the dike. A total of 10 ground surfaces are placed and surveyed with LiDAR.

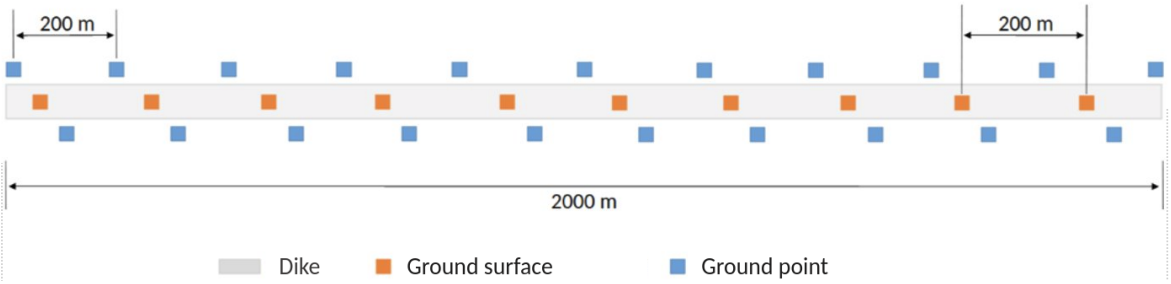

Figure. F.3 – An illustration of the landmark layout plan.

(a) Target serving as ground points (b) Target used for ground surfaces

Figure. F.4 – An illustration of the topographical landmarks.

F.4 Acquisition plan

A total of five flights are conducted. The first three flights surveyed the middle part of the site of interest (600 m). The last two flights covered the whole site of interest (2000 m) by surveying separately the south half (*flight 4*) and the north half (*flight 5*). For each flight, the two optical cameras are oriented so that one is nadir and the other is oblique. The thermal camera is always oriented nadir. Details of the conducted flights are given in Table. F.1, information regarding thermal images are omitted since they are not discussed in this thesis work. Note that the images acquired with *cam1* in *flight 4* are lost due to an accident.

Flight	1		2		3		4		5	
	cam1	cam2	cam1	cam2	cam1	cam2	cam1	cam2	cam1	cam2
Height (m)	50		50		30, 70		50		50	
Length (m)	600		600		600		1000		1000	
Nb of Strips	3		3		2		3		3	
Orientation	ob	na	na	ob	ob	na	ob	na	ob	na
Nb of images	289	289	278	281	251	242	0	375	428	388

Table. F.1 – Details on conducted flights – *LP2018*.

The main idea is to perform an in-flight camera calibration and lever-arm calibration with the *flight 1-3*, as proposed in **Chapter** 5. Then the calibrations are applied to a simple acquisition geometry (*flight 4-5)*).

Annexe G

Supplementary results

In this chapter, some supplementary results that are not included in the main body of the thesis are presented.

G.1 Simulation of Gaussian noise on tie points

In **Chapter 4**, three simulation cases that interested us were presented. Before performing these simulations, a test case was performed to verify the synthetic dataset. A Gaussian noise is added on simulated tie points of which the standard deviation varies from 1 pixel to 40 pixels (1px, 2px, 5px, 10px, 20px, 40px). For each value of the standard deviation, twenty draws are performed for statistical analysis. Once the Gaussian noise is added to tie points, a bundle block adjustment is performed with the modified tie points and all parameters are re-estimated.

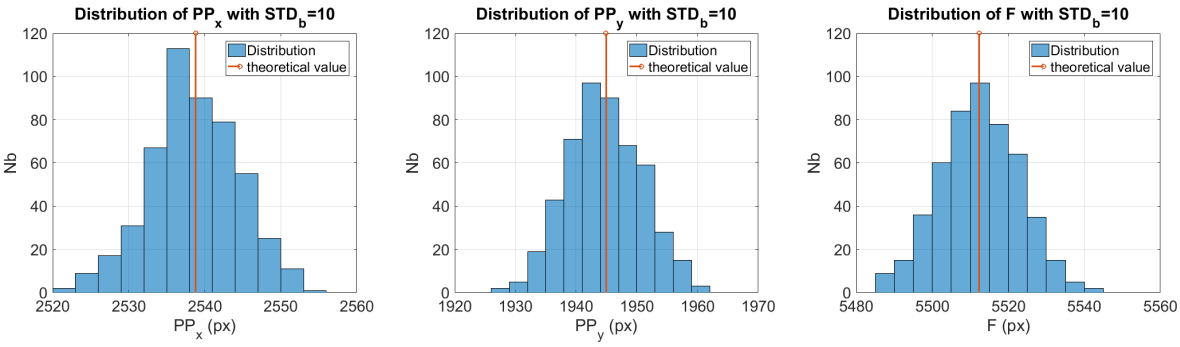

Figure. G.1 – Histogram of the estimation, the theoretical value (without noise) is shown in red line.

Figure. G.1 shows the histogram of estimated principal point and focal length with the STD of the added Gaussian noise equals to 10 pixels. The results of the estimation follow the Gaussian distribution, which validates the nature of the added noise and the generated synthetic dataset.

Figure. G.2 shows the RMS of residuals on CPs with respect to the added Gaussian noise. The RMS also increases almost linearly with the added Gaussian noise. The

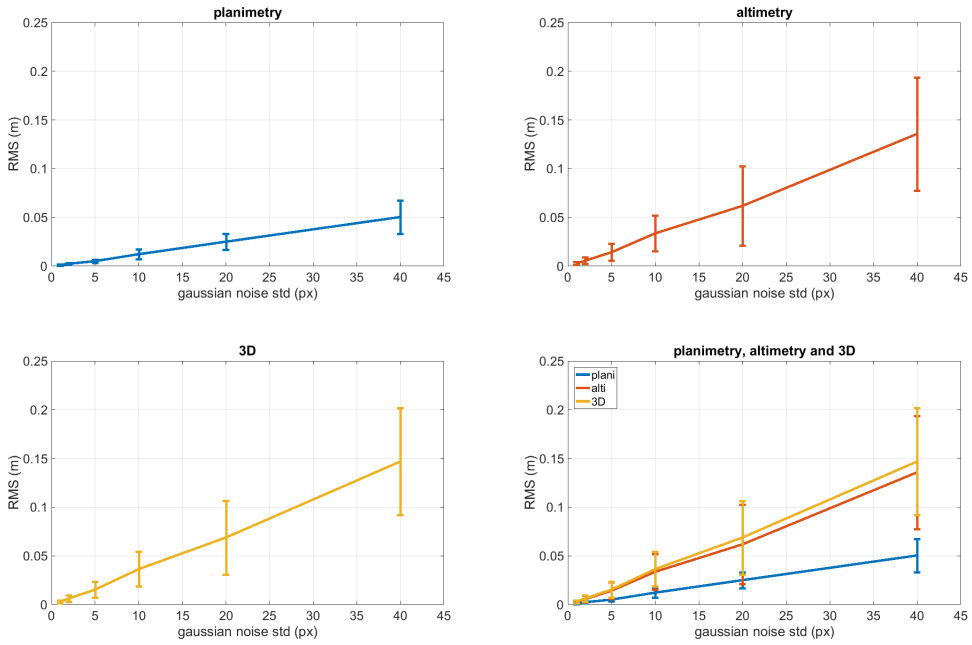

Figure. G.2 – Variation of camera calibration parameters.

addition of the Gaussian noise impacts more the altimetric accuracy.

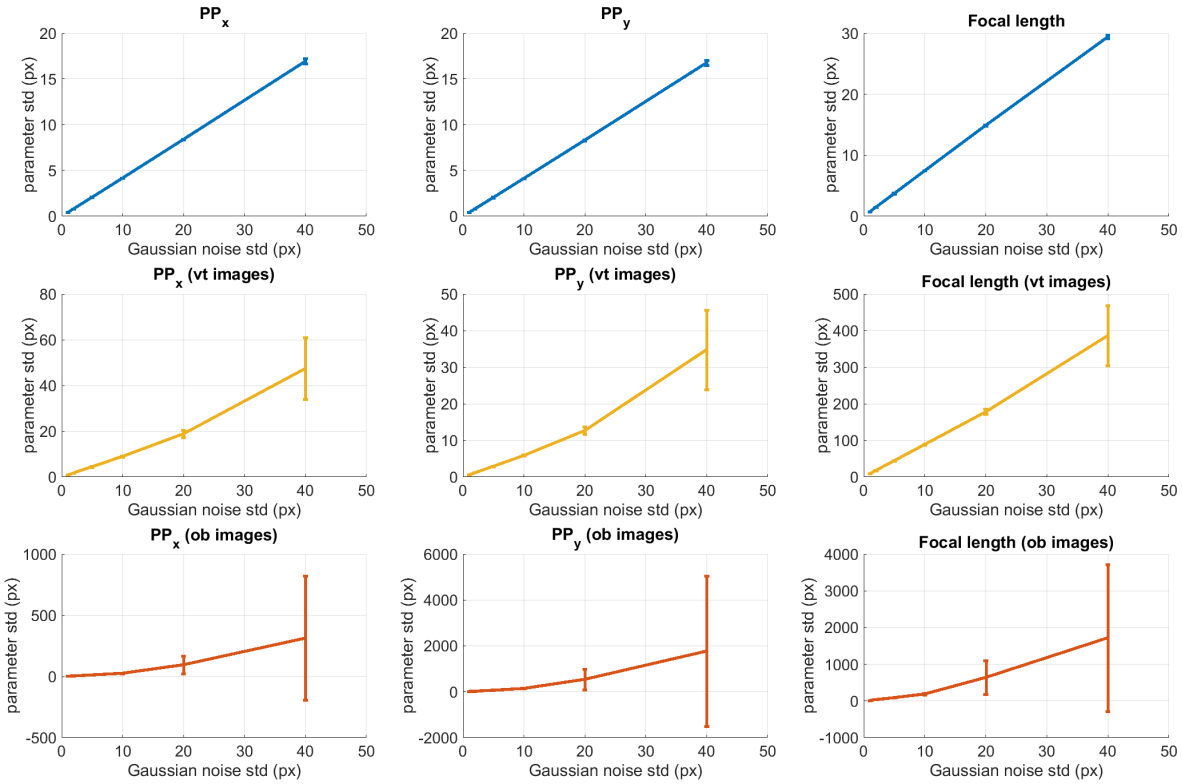

Figure. G.3 – Variation of camera calibration parameters.

Figure. G.3 depicts the standard deviation of the estimated focal length and principal point with respect to Gaussian noise added on tie points. The mean of the standard deviation is reprensented in line and its corresponding standard deviation is represented

in horizontal bar. It does not make much sense to calculate the mean and the standard deviation of the standard deviation, these values are given for indicative purposes. Three cases are presented, (1) with all images, (2) with only nadir images, (3) with only oblique images.

One can observe that standard deviation of the estimation increases with that of the added Gaussian noise. When all images are included, the standard deviation varies within a small range and increases linearly with that the added Gaussian noise. When only nadir images or oblique images are provided, the estimation results are less stable.

References

Ackermann, F. (1992). Operational rules and accuracy models for gps-aerotriangulation. *Arch. ISPRS*, 1 :691–700. 22, 44

Agarwal, S., Furukawa, Y., Snavely, N., Simon, I., Curless, B., Seitz, S. M., and Szeliski, R. (2011). Building rome in a day. *Communications of the ACM*, 54(10) :105–112. 24

Ait-Aider, O., Andreff, N., Lavest, J. M., and Martinet, P. (2006). Simultaneous object pose and velocity computation using a single view from a rolling shutter camera. In *European Conference on Computer Vision*, pages 56–68. Springer. 83

Audi, A., Pierrot-Deseilligny, M., Meynard, C., and Thom, C. (2017). Implementation of an IMU aided image stacking algorithm in a digital camera for unmanned aerial vehicles. *Sensors*, 17(7). 26, 62

Beguin, R. (2011). *Etude multi-échelle de l'érosion de contact au sein des ouvrages hydrauliques en terre*. PhD thesis, Université de Grenoble. 4, 5, 12, 13, XLV

Benoit, L., Briole, P., Martin, O., Thom, C., Malet, J.-P., and Ulrich, P. (2015). Monitoring landslide displacements with the Geocube wireless network of low-cost GPS. *Engineering geology*, 195 :111–121. 26

Blázquez, M. and Colomina, I. (2012a). On INS/GNSS-based time synchronization in photogrammetric and remote sensing multi-sensor systems. *Photogrammetrie-Fernerkundung-Geoinformation*, 2012(2) :91–104. 23

Blázquez, M. and Colomina, I. (2012b). Relative INS/GNSS aerial control in integrated sensor orientation : Models and performance. *ISPRS journal of photogrammetry and remote sensing*, 67 :120–133. 23, 46

Byröd, M. and Åström, K. (2009). Bundle adjustment using conjugate gradients with multiscale preconditioning. In *BMVC*, pages 1–10. 24

Chun, J.-B., Jung, H., and Kyung, C.-M. (2008). Suppressing rolling-shutter distortion of CMOS image sensors by motion vector detection. *IEEE Transactions on Consumer Electronics*, 54(4) :1479–1487. 83

CMOSIS (2013). *Application note for CMV - Temperature Sensor Calibration*, 2.1 edition. 62

CMOSIS (2015). *20 Megapixel global shutter CMOS image sensor - Datasheet*, 01 edition. 26, 62

Colomina, I. (1999). GPS, INS and aerial triangulation : What is the best way for the operational determination of photogrammetric image orientation ? *International Archives of Photogrammetry and Remote Sensing*, 32(3 ; SECT 2W5) :121–130. 22, 24

Colomina, I. and de la Tecnologia, P. M. (2008). Towards a new paradigm for high-resolution low-cost photogrammetryand remote sensing. In *The International Archives of the Photogrammetry, Remote Sensing and Spatial Information Sciences, ISPRS Congress, Beijing, China, XXXVII. Part B*, volume 1, pages 1201–1206. 1, 9, 20, 107

Cramer, M. and Stallmann, D. (2002). System calibration for direct georeferencing. *International Archives of Photogrammetry Remote Sensing and Spatial Information Sciences*, 34(3/A) :79–84. 45

Cramer, M., Stallmann, D., and Haala, N. (2000). Direct georeferencing using GPS/inertial exterior orientations for photogrammetric applications. *International Archives of Photogrammetry and Remote Sensing*, 33(B3/1 ; PART 3) :198–205. 21, 32

Cucci, D. A., Rehak, M., and Skaloud, J. (2017). Bundle adjustment with raw inertial observations in UAV applications. *ISPRS Journal of Photogrammetry and Remote Sensing*, 130 :1–12. 23, 24, 46

Daakir, M., Pierrot-Deseilligny, M., Bosser, P., Pichard, F., Thom, C., Rabot, Y., and Martin, O. (2017). Lightweight UAV with on-board photogrammetry and single-frequency GPS positioning for metrology applications. *ISPRS Journal of Photogrammetry and Remote Sensing*, 127 :115–126. 26, 45, 62

Daakir, M., Zhou, Y., Pierrot-Deseilligny, M., Thom, C., Martin, O., and Rupnik, E. (2019). Improvement of photogrammetric accuracy by modeling and correcting the thermal effect on camera calibration. *ISPRS Jounal for Photogrammetry and Remote Sensing*, 148 :142–155. 36

Duane, C. B. (1971). Close-range camera calibration. *Photogramm. Eng*, 37(8) :855–866. 21

Ebner, H. (1976). Self calibrating block adjustment. *Bildmessung und Luftbildwessen*, 44 :128–139. 21

Eisenbeiß, H. (2009). *UAV photogrammetry*. PhD thesis, ETH Zurich. 1, 9, 20, 107

Ellum, C. and El-Sheimy, N. (2002). Inexpensive kinematic attitude determination from MEMS-based accelerometers and GPS-derived accelerations. *Navigation*, 49(3) :117–126. 44

Fiedler, D. and Müller, H. (2012). Impact of thermal and environmental conditions on the kinect sensor. In *International Workshop on Depth Image Analysis and Applications*, pages 21–31. Springer. 61

Fonstad, M. A., Dietrich, J. T., Courville, B. C., Jensen, J. L., and Carbonneau, P. E. (2013). Topographic structure from motion : a new development in photogrammetric measurement. *Earth Surface Processes and Landforms*, 38(4) :421–430. 32

Francois, G. and Yannick, G. (2017). The senseFly S.O.D.A. genesis. In *Presented at UAV Metric Camera Special Sessions DGPF Annual Meeting 2017 - Würzburg, Germany*. 25, 61

Fraser, C. S. (1997). Digital camera self-calibration. *ISPRS Journal of Photogrammetry and Remote sensing*, 52(4) :149–159. 21, 33, 69, 71, 95

Gerke, M. and Przybilla, H.-J. (2016). Accuracy analysis of photogrammetric UAV image blocks : Influence of onboard RTK-GNSS and cross flight patterns. *Photogrammetrie-Fernerkundung-Geoinformation*, 2016(1) :17–30. 22

Gruen, A. (1978). Accuracy, reliability and statistics in close-range photogrammetry. In *Inter-Congress Symposium of ISP Commission V*. 21

Grundmann, M., Kwatra, V., Castro, D., and Essa, I. (2012). Calibration-free rolling shutter removal. In *2012 IEEE international conference on computational photography (ICCP)*, pages 1–8. IEEE. 83

Hauet, A., Muste, M., and Ho, H.-C. (2009). Digital mapping of riverine waterway hydrodynamic and geomorphic features. *Earth Surface Processes and Landforms*, 34(2) :242–252. 24

Hedborg, J., Ringaby, E., Forssén, P.-E., and Felsberg, M. (2011). Structure and motion estimation from rolling shutter video. In *2011 IEEE International Conference on Computer Vision Workshops (ICCV Workshops)*, pages 17–23. IEEE. 83

Heipke, C., Jacobsen, K., and Wegmann, H. (2001). The OEEPE test on integrated sensor orientation1. 24

Heipke, C., Jacobsen, K., and Wegmann, H. (2002a). Analysis of the results of the OEEPE test "integrated sensor orientation. In *OEEPE Integrated Sensor Orientation Test Report and Workshop Proceedings, Editors*. Citeseer. 32, 45

Heipke, C., Jacobsen, K., and Wegmann, H. (2002b). *Integrated sensor orientation : Test report and workshop proceedings*. Bundesamt für Kartographie und Geodäsie. 22, 24, 44

Hirschmuller, H. (2008). Stereo processing by semiglobal matching and mutual information. *IEEE Transactions on Pattern Analysis and Machine Intelligence*, 30(2) :328–341. 65

Hothmer, J. (1958). Possibilities and limitations for elimination of distortion in aerial photographs. *The Photogrammetric Record*, 2(12) :426–445. 61

Hutton, J. and Mostafa, M. M. (2005). 10 years of direct georeferencing for airborne photogrammetry. *GIS Business (GeoBit)*, 11(1) :33–41. 19

Ip, A., Mostafa, M., and El-Sheimy, N. (2004). Fast orthophoto production using the digital sensor system. In *Proceedings of the 7th Annual International Conference-Map India*, pages 28–30. 22

Ito, E. and Okatani, T. (2017). Self-calibration-based approach to critical motion sequences of rolling-shutter structure from motion. In *Proceedings of the IEEE Conference on Computer Vision and Pattern Recognition*, pages 801–809. 83

Jacobsen, K. (2004). Direct integrated sensor orientation-pros and cons. In *In : Proceedings of the XXth ISPRS Congress*. Citeseer. 24

James, M. R. and Robson, S. (2014). Mitigating systematic error in topographic models derived from UAV and ground-based image networks. *Earth Surface Processes and Landforms*, 39(10) :1413–1420. 32, 44, 47, 74

Jones, A. D. (1982). Manual of photogrammetry, eds cc slama, c. theurer and sw hendrikson, american society of photogrammetry, falls church, va., 1980, 180× 260mm, xvi and 1056 pages (with index), 72 tables, 866 figures. isbn 0 937294 01 2. *Cartography*, 12(4) :258–258. 20

Jozkow, G. and Toth, C. (2014). Georeferencing experiments with UAS imagery. *ISPRS Annals of the Photogrammetry, Remote Sensing and Spatial Information Sciences*, 2(1) :25. 23, 45

Klein, G. and Murray, D. (2009). Parallel tracking and mapping on a camera phone. In *2009 8th IEEE International Symposium on Mixed and Augmented Reality*, pages 83–86. IEEE. 83

Kölbl, O. R. (1976). Metric or non-metric cameras. *Photogrammetric Engineering and Remote Sensing*, 42(1) :103–113. 60

Kraft, T., Gessner, M., Meißner, H., Cramer, M., Przybilla, H.-J., Gerke, M., et al. (2016). Evaluation of a metric camera system tailored for high precision UAV applications. *International Archives of the Photogrammetry, Remote Sensing and Spatial Information Sciences-ISPRS Archives*. 26, 61

Kraft, T., Meißner, H., Berger, R., and Stebner, K. (2017). Preliminary results of developing a metric aerial camera for UAV applications. In *Presented at UAV Metric Camera Special Sessions DGPF Annual Meeting 2017 - Würzburg, Germany*. 25, 61

Kruck, E. (2001). Combined IMU and sensor calibration with BINGO-F. In *Integrated Sensor Orientation, Proc. of the OEEPE Workshop". Hannover : CD-ROM*. 45

Levenberg, K. (1944). A method for the solution of certain non-linear problems in least squares. *Quarterly of applied mathematics*, 2(2) :164–168. 24

Li, K., Stueckmann-Petring, J., and Commision III, I. (1993). Methods and results of combined adjustment utilizing kinematic GPS positioning and photogrammetric data. *INTERNATIONAL ARCHIVES OF PHOTOGRAMMETRY AND REMOTE SENSING*, 29 :213–213. 23

Liang, C.-K., Chang, L.-W., and Chen, H. H. (2008). Analysis and compensation of rolling shutter effect. *IEEE Transactions on Image Processing*, 17(8) :1323–1330. 83

Lichti, D., Skaloud, J., and Schaer, P. (2008). On the calibration strategy of medium format cameras for direct georeferencing. In *International Calibration and Orientation Workshop EuroCOW*. 21, 45, 79

Lin, D.-L., Wang, C.-C., and Wei, C.-L. (2010). Quantified temperature effect in a CMOS image sensor. *IEEE Transactions on Electron Devices*, 57(2) :422–428. 61

Lourakis, M. and Argyros, A. (2004). The design and implementation of a generic sparse bundle adjustment software package based on the levenberg-marquardt algorithm. Technical report, Technical Report 340, Institute of Computer Science-FORTH, Heraklion, Crete 23

Lourakis, M. and Argyros, A. A. (2005). Is levenberg-marquardt the most efficient optimization algorithm for implementing bundle adjustment ? In *Tenth IEEE International Conference on Computer Vision (ICCV'05) Volume 1*, volume 2, pages 1526–1531. IEEE. 24

Lowe, D. G. et al. (1999). Object recognition from local scale-invariant features. In *iccv*, volume 99, pages 1150–1157. 47

Luhmann, T. (2010). Close range photogrammetry for industrial applications. *ISPRS Journal of Photogrammetry and Remote Sensing*, 65(6) :558 – 569. ISPRS Centenary Celebration Issue. 60

Maas, H.-G. and Hampel, U. (2006). Photogrammetric techniques in civil engineering material testing and structure monitoring. *Photogrammetric Engineering & Remote Sensing*, 72(1) :39–45. 65

Magerand, L. and Bartoli, A. (2010). A generic rolling shutter camera model and its application to dynamic pose estimation. In *International symposium on 3D data processing, visualization and transmission*. 83

Martin, O., Meynard, C., Pierrot Deseilligny, M., Souchon, J.-P., and Thom, C. (2014). Réalisation d'une caméra photogrammétrique ultralégère et de haute résolution. In *Proceedings of the colloque drones et moyens légers aéroportés d'observation, Montpellier, France*, pages 24–26. 25, 47, 61

Martinez-Rubi, O. (2016). Improving open-source photogrammetric workflows for processing big datasets. *Netherlands eScience Center : Amsterdam, The Netherlands*. 52, 96

Meingast, M., Geyer, C., and Sastry, S. (2005). Geometric models of rolling-shutter cameras. *arXiv preprint cs/0503076*. 83

Merchant, D. C. (2006). Influence of temperature on focal length for the airborne camera. In *Proc. of MAPPS/ASPRS Fall Conference*. 61, 68, 78

Merchant, D. C. (2012). Aerial camera metric calibration - history and status. In *Proceedings of ASPRS 2012 Annual Conference, Sacramento, Calif.* 61, 68, 78

Mian, O., Lutes, J., Lipa, G., Hutton, J., Gavelle, E., and Borghini, S. (2015). Direct georeferencing on small unmanned aerial platforms for improved reliability and accuracy of mapping without the need for ground control points. *The International Archives of Photogrammetry, Remote Sensing and Spatial Information Sciences*, 40(1) :397. 19, 22, 45, XLV

Mostafa, M. (2002). Camera/IMU boresight calibration : New advances and performance analysis. In *Proceedings, ASPRS Annual Meeting, Washington, DC, April*, pages 21–26. 24, 45

Nex, F. and Remondino, F. (2014). UAV for 3D mapping applications : a review. *Applied geomatics*, 6(1) :1–15. 17, 20, 32, 82, 107

Ni, K., Steedly, D., and Dellaert, F. (2007). Out-of-core bundle adjustment for large-scale 3D reconstruction. In *2007 IEEE 11th International Conference on Computer Vision*, pages 1–8. IEEE. 24

Nocerino, E., Menna, F., and Remondino, F. (2014). Accuracy of typical photogrammetric networks in cultural heritage 3D modeling projects. *The International Archives of Photogrammetry, Remote Sensing and Spatial Information Sciences*, 40(5) :465. 74

Pan, B., Shi, W., and Lubineau, G. (2015). Effect of camera temperature variations on stereo-digital image correlation measurements. *Applied optics*, 54(34) :10089–10095. 63

Pauly, K., Aumont, J.-F., and Mancini, B. (2017). From off-the-shelf to off-the-charts : shifting the camera paradigm in commercial fixed wing UAS to increase accuracy. In *Presented at UAV Metric Camera Special Sessions DGPF Annual Meeting 2017 - Würzburg, Germany*. 25, 61

Pfeifer, N., Glira, P., and Briese, C. (2012). Direct georeferencing with on board navigation components of light weight UAV platforms. *International Archives of the Photogrammetry, Remote Sensing and Spatial Information Sciences*, 39 :487–492. 23

Pierrot-Deseilligny, M. and Paparoditis, N. (2006). A multiresolution and optimization-based image matching approach : An application to surface reconstruction from SPOT5-HRS stereo imagery. *Archives of Photogrammetry, Remote Sensing and Spatial Information Sciences*, 36(1/W41). 65

Rehak, M. and Skaloud, J. (2015). Fixed-wing micro aerial vehicle for accurate corridor mapping. *ISPRS Annals of the Photogrammetry, Remote Sensing and Spatial Information Sciences*, 2(1) :23. 24, 44, 46

Rehak, M. and Skaloud, J. (2016). Applicability of new approaches of sensor orientation to micro aerial vehicles. *ISPRS Annals of the Photogrammetry, Remote Sensing and Spatial Information Sciences*, 3 :441. 22, 23

Rehak, M. and Skaloud, J. (2017). Time synchronization of consumer cameras on micro aerial vehicles. *ISPRS Journal of Photogrammetry and Remote Sensing*, 123 :114–123. 23

Remondino, F., Barazzetti, L., Nex, F., Scaioni, M., and Sarazzi, D. (2011). UAV photogrammetry for mapping and 3D modeling–current status and future perspectives. *International Archives of the Photogrammetry, Remote Sensing and Spatial Information Sciences*, 38(1) :C22. 1, 9, 21, 44

Remondino, F. and Fraser, C. (2006). Digital camera calibration methods : considerations and comparisons. *International Archives of Photogrammetry, Remote Sensing and Spatial Information Sciences*, 36(5) :266–272. 21, 60

Rieke-Zapp, D. H. and Nearing, M. A. (2005). Digital close range photogrammetry for measurement of soil erosion. *The Photogrammetric Record*, 20(109) :69–87. 60

Rosu, A.-M., Pierrot-Deseilligny, M., Delorme, A., Binet, R., and Klinger, Y. (2015). Measurement of ground displacement from optical satellite image correlation using the free open-source software MicMac. *ISPRS Journal of Photogrammetry and Remote Sensing*, 100 :48 – 59. High-Resolution Earth Imaging for Geospatial Information. 65

Rupnik, E., Daakir, M., and Deseilligny, M. P. (2017). MicMac–a free, open-source solution for photogrammetry. *Open Geospatial Data, Software and Standards*, 2(1) :14. 20, 28, 34, 47, 52, 82, 96, XLV

Saks, N. (1980). A technique for suppressing dark current generated by interface states in buried channel CCD imagers. *IEEE Electron Device Letters*, 1(7) :131–133. 60

Sauer, D. J. (2001). CMOS image sensor with reduced fixed pattern noise. US Patent 6,320,616. 61

Saurer, O., Pollefeys, M., and Hee Lee, G. (2016). Sparse to dense 3D reconstruction from rolling shutter images. In *Proceedings of the IEEE Conference on Computer Vision and Pattern Recognition*, pages 3337–3345. 83

Schut, G. (1979). Selection of additional parameters for the bundle adjustment. *Photogrammetric Engineering and Remote Sensing*, 45(9) :1243–1252. 21

Schwartz, J. (2010). New CMOS image sensor is useful in extreme temperatures. 61

Skaloud, J., Cramer, M., and Schwarz, K. (1996). Exterior orientation by direct measurement of camera position and attitude. *International Archives of Photogrammetry and Remote Sensing*, 31(B3) :125–130. 24, 45

Skaloud, J., Rehak, M., and Lichti, D. (2014). Mapping with MAV : Experimental study on the contribution of absolute and relative aerial position control. *The International Archives of Photogrammetry, Remote Sensing and Spatial Information Sciences*, 40(3) :123. 22, 23, 44, 46

Skaloud, J. and Schaer, P. (2003). Towards a more rigorous boresight determination : Theory, technology and realities of inertial/gps sensor orientation. In *Proceedings of the ISPRS, WG 1/5 Platform and Sensor Integration Conference*. 45

Skaloud, J. and Schwarz, K.-P. (2000). Accurate orientation for airborne mapping systems. *Photogrammetric Engineering & Remote Sensing*, 66(4) :393–401. 24

Skaloud, J. and Vallet, J. (2002). High accuracy handheld mapping system for fast helicopter deployment. 34(4) :614–619. 45

Smith, M. and Cope, E. (2010). The effects of temperature variation on single-lens-reflex digital camera calibration parameters. *International Archives of Photogrammetry, Remote Sensing and Spatial Information Sciences*, 38(Part 5). 61

Sun, Y. and Liu, G. (2012). Rolling shutter distortion removal based on curve interpolation. *IEEE Transactions on Consumer Electronics*, 58(3) :1045–1050. 83

Sun, Y., Liu, G., and Sun, Y. (2016). An affine motion model for removing rolling shutter distortions. *IEEE Signal Processing Letters*, 23(9) :1250–1254. 83

Takasu, T. (2013). RTKLIB ver. 2.4. 2 manual. *RTKLIB : An Open Source Program Package for GNSS Positioning*, pages 29–49. 28, 29, XLV

Takasu, T. and Yasuda, A. (2009). Development of the low-cost RTK-GPS receiver with an open source program package RTKLIB. In *International symposium on GPS/GNSS*, pages 4–6. International Convention Center Jeju Korea. 28

Tournadre, V. (2015). *Métrologie par photogrammétrie aéroportée légère : application au suivi d'évolution de digues*. PhD thesis, Université Paris-Est. 5, 13, 47, 107, XX, XLV

Tournadre, V., Pierrot-Deseilligny, M., and Faure, P.-H. (2014). UAV photogrammetry to monitor dykes-calibration and comparison to terrestrial lidar. *The International Archives of Photogrammetry, Remote Sensing and Spatial Information Sciences*, 40(3) :143. 44

Triggs, B., McLauchlan, P. F., Hartley, R. I., and Fitzgibbon, A. W. (1999). Bundle adjustment - a modern synthesis. In *International workshop on vision algorithms*, pages 298–372. Springer. 23

Vallet, J. (2007). GPS/IMU and LiDAR integration to aerial photogrammetry : Development and practical experiences with Helimap system. *Vorträge Dreiländertagung*, 27. 61

Vallet, J., Panissod, F., Strecha, C., and Tracol, M. (2011). Photogrammetric performance of an ultra light weight swinglet UAV. In *UAV-g*. 21, 44

Vautherin, J., Rutishauser, S., Schneider-Zapp, K., Choi, H. F., Chovancova, V., Glass, A., and Strecha, C. (2016). Photogrammetric accuracy and modeling of rolling shutter cameras. *ISPRS Ann. Photogramm. Remote Sens. Spat. Inf. Sci*, 3 :139–146. 82, 83, 84, 99, XLVIII

Westoby, M., Brasington, J., Glasser, N., Hambrey, M., and Reynolds, J. (2012). 'structure-from-motion'photogrammetry : A low-cost, effective tool for geoscience applications. *Geomorphology*, 179 :300–314. 32

Widenhorn, R., Blouke, M. M., Weber, A., Rest, A., and Bodegom, E. (2002). Temperature dependence of dark current in a CCD. In *Sensors and Camera Systems for Scientific, Industrial, and Digital Photography Applications III*, volume 4669, pages 193–202. International Society for Optics and Photonics. 60

Wright, S. and Nocedal, J. (1999). Numerical optimization. *Springer Science*, 35(67-68) :7. 28, 49

Yastikli, N. and Jacobsen, K. (2005). Influence of system calibration on direct sensor orientation. *Photogrammetric Engineering & Remote Sensing*, 71(5) :629–633. 61

Zhang, C. et al. (2008). An UAV-based photogrammetric mapping system for road condition assessment. *Int. Arch. Photogramm. Remote Sens. Spatial Inf. Sci*, 37 :627–632. 24

Zhou, Y., Rupnik, E., Faure, P.-H., and Pierrot-Deseilligny, M. (2018). GNSS-assisted integrated sensor orientation with sensor pre-calibration for accurate corridor mapping. *Sensors*, 18(9) :2783. 26, 32, 33, 37, 62

Glossary

AP Application Program
BBA Bundle Block Adjustment
BDS BeiDou Navigation Satellite System
CCD Charge-Coupled Device
CMOS Complementary Metal-Oxide Semiconductor
CP Check Point
CUI Command-line User Interface
DEM Digital Elevation Model
DGAC Direction Générale de l'Aviation Civile
DiSO Direct Sensor Orientation
DOF Degree of Freedom
DSLR Digital Single-Lens Reflex
DSM Digital Surface Model
EO Exterior Orientation
GCP Ground Control Point
GLONASS Global Navigation Satellite System
GNSS Global Navigation Satellite System
GPS Global Positioning System
GSD Ground Sampling Distance
GUI Graphical User Interface
IMU Inertial Measurement Unit
INS Inertial Navigation System
InSO Indirect Sensor Orientation
IO Interior Orientation
IRNSS Indian Regional Navigation Satellite System
ISO Integrated Sensor Orientation
QZSS Quasi-Zenith Satellite System
RSM Root Mean Square
SIFT Scale invariant feature transform
STD Standard Deviation
UAV Unmanned Aerial vehicles

Table des figures

Liste des tableaux